Chapter 2
Advanced Mueller Ellipsometry Instrumentation and Data Analysis

Enric Garcia-Caurel, Razvigor Ossikovski , Martin Foldyna, Angelo Pierangelo, Bernard Drévillon and Antonello De Martino

Abstract The main object of this chapter is to give an overview the possibilities offered by instruments capable of measuring full Mueller matrices in the field of optical characterization. We have chosen to call these instruments Mueller ellipsometers in order to highlight their close relation with instruments traditionally used in ellipsometry. We want to make clear to the reader the place that Mueller ellipsometry takes with respect to standard ellipsometry by showing the similarities but also the differences among these techniques, both in instrumentation and data treatment. To do so the chapter starts by a review of the optical formalisms used in standard and Mueller ellipsometry respectively. In order to highlight the particularities and the advantages brought by Mueller ellipsometry, a special section is devoted to the algebraic properties of Mueller matrices and to the description of different ways to decompose them. Matrix decompositions are used to unveil the basic polarimetric properties of a the sample when a precise model is not available. Then follows a description of the most common optical configurations used to build standard ellipsometers. Special attention is paid to show what can and what cannot be measured with them. On the basis of this knowledge it is shown the interest of measuring whole

E. Garcia-Caurel (✉) · R. Ossikovski · M. Foldyna · A. Pierangelo · B. Drévillon · A. De Martino
LPICM, CNRS-Ecole Polytechnique,
Palaiseau, France
e-mail: enric.garcia-caurel@polytechnique.edu

R. Ossikovski
e-mail: razvigor.ossikovski@polytechnique.edu

M. Foldyna
e-mail: martin.foldyna@polytechnique.edu

A. Pierangelo
e-mail: angelo.pierangelo@polytechnique.edu

B. Drévillon
e-mail: bernard.drevillon@polytechnique.edu

A. De Martino
e-mail: antonello.demartino@polytechnique.edu

M. Losurdo and K. Hingerl (eds.), *Ellipsometry at the Nanoscale*,
DOI: 10.1007/978-3-642-33956-1_2,

Mueller matrices, in particular for samples characterized by complex anisotropy and/or depolarization. Among the numerous optical assemblies able to measure full Mueller matrices, most of them are laboratory prototypes, and only very few have been industrialized so far. Because an extensive and comparative review of all the Mueller ellipsometric instruments developed to date is clearly out of the scope of this chapter, we limit our description to four Mueller ellipsometers, two imaging and two spectroscopic systems that have been developed by us in the past years. The technical description of the Mueller ellipsometers is accompanied by some examples of applications which, without being exhaustive, are representative of the type of analyses performed in ellipsometry, and also illustrate the advantages that can be brought by modern Mueller ellipsometers to optical metrology, materials science and biomedicine.

2.1 Introduction

The use of polarized light to characterize the optical properties of materials, either in bulk or thin film format, is generally called Ellipsometry. The technique finds its roots in the pioneering work by Paul Drude in the nineteenth century when he used polarized light in a reflection configuration to study the optical properties and thickness of very thin metallic films. Since then, many methods have been successfully used to generate and analyze the polarization properties of light, and this technique has enjoyed a great success over the past decades. Hundreds of studies and industrial applications have emerged, which are either directly based on ellipsometry, or profit from its sensitivity.

Classical ellipsometric measurements require that the light beam remains completely polarized during the measurement process. Let us recall that a light beam is said to be fully polarized, when the relative phase between the different components of the electromagnetic field along two orthogonal directions remains constant. If for some reason, this relative phase varies (spatially, spectrally and/or temporally), the light will become partially polarized. If so, single ellipsometric measurements lose their physical meaning. To correctly measure and physically interpret the properties of partially polarized light, it is necessary to use the more general technique called Mueller Ellipsometry or Polarimetry. Mueller ellipsometry is thus needed for complete and accurate characterization of the anisotropic and/or depolarizing samples of interest in many instances, both in academic research and “real life” activities. We prefer the term “Mueller Ellipsometry” instead of “Polarimetry”, to emphasize the close relationship of this technique with standard ellipsometry. Several excellent monographs [1–3] have been published covering different aspects of both standard and Mueller ellipsometry, such as the theory of polarization, the optical response of solids, the instrumentation and innovative applications.

This chapter is aimed at accounting for the novel Muller ellipsometric data analysis, instrumentation, and their applications in the context of standard ellipsometry. Our purpose is not only to give a simple technical description of these aspects but also to show their interest for non-experienced and experienced users of standard

ellipsometry. The chapter is organized in different sections but it can be divided in three conceptual parts.

The first one starts by recalling the Jones and Stokes formalisms used in standard and Mueller ellipsometry respectively. Next we introduce the basic polarimetric effects such as dichroism, retardance, depolarization and polarizance. Those are the basic "building blocks" which allow to interpret the information brought by Mueller matrices in physical terms. Next we show different ways to decompose Mueller matrices into sums or products of simpler matrices which can be helpful to understand the physics and/or the structure of the samples. The next section consists of an overview of the basics of an ellipsometric measurement, and the usual process of treating ellipsometric data (inversion problem). This section emphasizes the features common to standard and Mueller ellipsometry.

The next section opens the second conceptual part of the chapter, devoted to instrumentation. The section gives an overview of the four most widely used types of ellipsometers. A special attention will be paid to show what can be measured with these ellipsometric configurations, or in other words, which elements of the Mueller matrix can be accessed. The purpose is to show the limitations of standard ellipsometers and the advantages brought by modern Mueller ellipsometers. In the next section we compare Generalized and Mueller ellipsometry, to show their equivalence for the study of complex but non-depolarizing samples, and the interest of measuring the full Mueller matrix when depolarization is present. The next section is devoted to various instrumentation issues of Mueller ellipsometers. We start recalling the basic theoretical background needed to design optimal polarimeters. Special emphasis is put on the concept of condition number, which has been used as a figure of merit to predict the optical performance of the designed instrument. Calibration is also an important issue because it strongly influences the quality of the measurements. We provide a concise description of a particularly useful, robust and versatile calibration procedure called "eigenvalue calibration method" (ECM). In the following section, we review different Mueller ellipsometers developed by the authors of the present chapter: (i) a spectroscopic system based on liquid crystal variable retarders working in the visible and near infrared, (ii) a broadband spectroscopic Mueller ellipsometer which has been adapted to work in the mid-infrared range, (iii) an imaging Mueller ellipsometer based on liquid crystal retarders to work with macroscopic samples with a characteristic size of few centimeters, (iv) an angle-resolved imaging Mueller ellipsometer coupled to a microscope in order to analyze tiny parts samples with a high degree of magnification.

The third part is devoted some examples of application of these Mueller ellipsometers. These applications, namely optical metrology and determination of dielectric functions of materials in broad spectral ranges, are representative of very common uses of Mueller ellipsometers. Optical metrology means the determination of physical dimensions such as thin film thicknesses, profile reconstruction of one-dimensional or two-dimensional diffraction gratings, or the overlay (misalignment) between stacked patterned structures. we show that even if we use only visible light we are able to push the accuracy of the optical metrology to the nanometer scale. Finally, we present some very recent and promising results of Mueller imaging for the detection and staging of

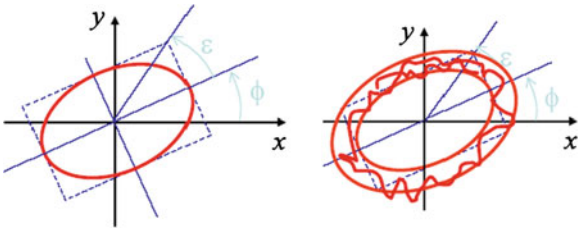

Fig. 2.1 Examples of electric field trajectories in the plane perpendicular to the propagation direction for fully polarized (*left*) or partially polarized (*right*) light waves

cancer both ex-vivo, and in vivo. In the conclusion, we try to summarize our vision of the status and the possibilities of Mueller ellipsometry, both from the instrumental point of view and for "real world" applications.

2.2 The Polarization of Light

In this section, we briefly review the most widely used theoretical descriptions of the light polarization properties, namely the Jones formalism for totally polarized light and the Stokes-Mueller formalism, which is the most general representation and can adequately account for any polarization states. The polarimetric properties of any sample are then defined from the changes this sample introduces in the polarization state of a probe light beam. In turn, these properties may be used for various purposes, from very well established applications (such as material and thin film characterizations) to more advanced ones, such as remote sensing and/or medical diagnosis.

As described in textbooks on electromagnetism [4], when a light ray propagates (through an isotropic or weakly birefringent medium) along the z direction, the electric field vector $\mathbf{E}$ is confined to vibrate in a x–y plane perpendicular to z, as illustrated in Fig. 2.1.

For totally polarized states, the electric field $\mathbf{E}$ describes an ellipse, characterized by its ellipticity ε and the azimuth of its major axis ϕ. The particular cases of linear and circular polarizations respectively correspond to $\varepsilon = 0$, and $\phi = 45°$. In contrast, partially polarized states correspond to more disordered motions of the electric field, which can be properly described only statistically, from cross-correlation functions, as discussed below.

2.2.1 The Jones Formalism

As mentioned above, the Jones formalism is well adapted to the description of totally polarized states. Any elliptical motion of $\mathbf{E}$ can be decomposed along the x and y axes,

with real amplitudes A_i and phases ϕ_i, $(i = x, y)$ which can be lumped into complex numbers E_i. Because in ellipsometry measurements are in general performed either in reflection or transmission configurations, it is common to choose as reference for the coordinates x and y, the directions parallel and perpendicular with respect to the plane of incidence, called p and s respectively. Then for transversal electromagnetic waves the Jones vector for the electric field is given by:

$$\begin{pmatrix} E_x \\ E_y \end{pmatrix} = \begin{pmatrix} E_p \\ E_s \end{pmatrix} = \begin{pmatrix} A_p e^{i\varphi_p} \\ A_s e^{i\varphi_s} \end{pmatrix} \tag{2.1}$$

Stated in the form (2.1), the Jones vector contains also an overall phase factor, which may be important in some cases, when the polarized beam under study interferes with another beam. However, as long as only single-beam ellipsometry is concerned, this overall phase can be removed, for example by setting $\phi_\mathrm{p} = 0$. In the absence of depolarization, the interaction with a sample transforms the Jones vector of the incident beam into another Jones vector, by a linear transformation:

$$\begin{pmatrix} E_p^{out} \\ E_s^{out} \end{pmatrix} = \begin{pmatrix} J_{pp} & J_{ps} \\ J_{sp} & J_{ss} \end{pmatrix} \begin{pmatrix} E_p^{in} \\ E_s^{in} \end{pmatrix} \tag{2.2}$$

where the J_{ij} are the elements of the Jones matrix. In a similar way as for Jones vectors, if one is interested only in the polarimetric properties of the sample and not its overall optical path (or phase shift) then one element can be taken as a real number (phase set arbitrarily to zero), and the Jones matrix depends on seven real parameters. This dependence can be further reduced to six if the overall amplitude transmission (or reflectivity) is also neglected. For plane and isotropic samples the Jones matrix in (2.2) takes on a special simple form: diagonal. It turns out that in practice the majority of substrates and thin films produced in research or industrial laboratories are isotropic, which makes the study by ellipsometry particularly simple.

$$\begin{pmatrix} E_x^{in} \\ E_y^{in} \end{pmatrix} = \begin{pmatrix} r_p & 0 \\ 0 & r_s \end{pmatrix} \begin{pmatrix} E_x^{in} \\ E_y^{in} \end{pmatrix} \tag{2.3}$$

Jones matrix elements can be interpreted in terms of the Fresnel reflection coefficients in polarization parallel, r_p, and perpendicular, r_s, to the plane of incidence. If the measurement is performed in transmission configuration, r_p and r_s must be substituted by the respective equivalent Fresnel transmission coefficients t_p and t_s (Fig. 2.2).

Ellipsometry measures the change on the polarization state of a beam after reflection or transmission by a sample. In the simplest case of isotropic samples, standard ellipsometry measures a couple of values Ψ and Δ called the ellipsometric angles. The angles Ψ and Δ are usually defined from the ratio ρ,

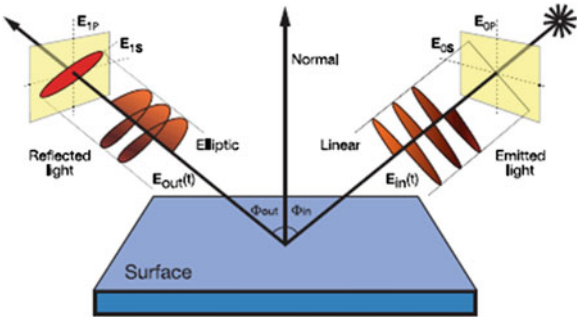

Fig. 2.2 Schematic view of a ellipsometric measurement in reflection configuration. The polarized beam is incident on the sample from the *right side*. After reflection the polarization state of the beam has changed and pursuits its propagation to the *left side*

$$\rho = \frac{r_p}{r_s} = \tan\Psi e^{i\Delta} \tag{2.4}$$

where

$$\tan\Psi = \frac{|\mathrm{r_p}|}{|\mathrm{r_s}|} \quad \text{and} \quad \Delta = \delta_\mathrm{p} - \delta_\mathrm{s} \tag{2.5}$$

Thus, $\tan\Psi$ is the amplitude ratio upon reflection, and Δ is the difference in phase shift. As it will be shown in a subsequent section of this chapter, Sect. 2.5.3, standard ellipsometers do not measure directly Ψ and Δ, but functions of them.

2.2.2 The Stokes-Mueller Formalism

2.2.2.1 General Polarization States: Coherence and Stokes Vectors

For partially depolarized states, the disordered motion of the electric field in the (x, y) plane schematically shown in Fig. 2.1, can be properly described only by its *statistical properties* instead of its instantaneous values. For this reason it is preferable to use field intensities instead of amplitudes. At first sight, one might think that a full probability distribution of the electric field **E** would be needed to fully characterize such states. In fact, as long as only intensity measurements can be performed with state-of-the art detectors at optical frequencies, all that is needed to predict the result of any classical measurement are the *second moments* (statistical averages of quadratic functions) of the electric field distributions. As a result, in the framework of linear optics, any possible polarization state of partially polarized field can be fully characterized by a four dimensional vector, called the field coherence vector **C**, defined for any set of a orthogonal axes (p, s). In the context of ellipsometry, the p and s axes are traditionally chosen to be oriented along the directions parallel and

perpendicular to the plane of incidence. Accordingly C can be written as:

$$\mathbf{C}^T = (C_1, C_2, C_3, C_4) = \left(\left\langle E_p E_p^* \right\rangle, \left\langle E_p E_s^* \right\rangle, \left\langle E_s E_p^* \right\rangle, \left\langle E_s E_s^* \right\rangle\right) \tag{2.6}$$

where the first and last components are real while the other two are complex conjugates of each other. However, in practice the most widely used vector to characterize arbitrary polarization states is the Stokes vector :

$$\mathbf{S} = \begin{pmatrix} I \\ Q \\ U \\ V \end{pmatrix} = \begin{pmatrix} I_p + I_s \\ I_p - I_s \\ I_{45^\circ} - I_{-45^\circ} \\ I_L - I_R \end{pmatrix} = \begin{pmatrix} \left\langle E_p E_p^* + E_s E_s^* \right\rangle \\ \left\langle E_p E_p^* - E_s E_s^* \right\rangle \\ \left\langle E_p E_s^* + E_s E_p^* \right\rangle \\ i\left\langle E_p E_s^* - E_s E_p^* \right\rangle \end{pmatrix} = \mathbf{AC} \quad \text{with}$$

$$\mathbf{A} = \begin{pmatrix} 1 & 0 & 0 & 1 \\ 1 & 0 & 0 & -1 \\ 0 & 1 & 1 & 0 \\ 0 & i & -i & 0 \end{pmatrix} \tag{2.7}$$

The popularity of the four dimensional real Stokes vector is certainly due to its immediate relationship with the directly measurable quantities $I_p, I_s, I_{+45}, I_{-45}$ i.e. the intensities which would be measured through ideal linear polarizers oriented along the p, s, $p + 45^\circ$ and $p{-}45^\circ$ in the plane perpendicular to the direction of propagation, while I_L and I_R would be the intensities transmitted by left and right circular polarizers [1]. Contrarily to the Stokes vectors, the Jones vector, which is defined in terms of electric field amplitudes, cannot be measured at optical frequencies.

In the most general case of partially polarized light the brackets at the right hand sides of (2.6) and (2.7) stand for all possible ways to take averages, e.g. spatially, spectrally or temporally, depending on the sample and measurement conditions. Thus, partially polarized states can be viewed as *incoherent superpositions of fully polarized states with different polarizations*, with simple addition of intensities and no interference effect. Conversely, for fully polarized states the field amplitudes are well defined and there is no need of averaging whatsoever. The corresponding brackets can thus be removed from (2.6) and (2.7).

Within the Stokes formalism, the *degree of polarization* ρ_S related to a given Stokes vector $\mathbf{S}$ is defined as:

$$\rho_S = \frac{\sqrt{Q^2 + U^2 + V^2}}{I} \tag{2.8}$$

This parameter varies between 0, for totally depolarized (fully disordered) states; and 1, for totally polarized states. This is an important difference between Jones and

Stokes vectors: *while Jones vectors may have any complex components, without any limitation whatsoever, this is no longer true for Stokes vectors*, for which ρ_s must be comprised between 0 and 1 to actually represent a physically realizable polarization state.

2.2.2.2 Interaction with a Sample: Mueller Matrices

Let us first consider the transformation of a fully polarized light by interaction with a non-depolarizing sample. From the transformation described within the Jones formalism by (2.2) we immediately obtain

$$(E_i E_j^*)^{out} = \sum_{k,l} J_{ik} J_{jl}^* \, (E_k E_l^*)^{in} \tag{2.9}$$

If we now consider the general case of a partially depolarized state interacting with a partially depolarizing sample, then both sides of (2.9) must be averaged. Now, in linear optics there is absolutely no reason to expect any statistical correlations between the fluctuations of the Jones matrix elements characterizing the sample and those of the incoming field amplitudes, as the light field cannot affect the sample properties in any way at the intensities typical of ellipsometric measurements. As a result, the quadratic functions of the Jones matrix and of the field amplitudes can be averaged separately,

$$\left\langle E_i E_j^* \right\rangle^{out} = \sum_{k,l} \left\langle J_{ik} J_{jl}^* \right\rangle \left\langle E_k E_l^* \right\rangle^{in} \quad \text{or} \quad \mathbf{C}^{out} = \mathbf{F}\, \mathbf{C}^{in} \tag{2.10}$$

where the matrix $\mathbf{F}$ is obtained by renumbering the couples of indices ik and jl in the same way as it was done for the coherence vector $\mathbf{C}$ in (2.6):

$$\mathbf{F} = \begin{bmatrix} \left\langle J_{pp} J_{pp}^* \right\rangle & \left\langle J_{pp} J_{ps}^* \right\rangle & \left\langle J_{ps} J_{pp}^* \right\rangle & \left\langle J_{ps} J_{ps}^* \right\rangle \\ \left\langle J_{pp} J_{sp}^* \right\rangle & \left\langle J_{pp} J_{ss}^* \right\rangle & \left\langle J_{ps} J_{sp}^* \right\rangle & \left\langle J_{ps} J_{ss}^* \right\rangle \\ \left\langle J_{sp} J_{pp}^* \right\rangle & \left\langle J_{sp} J_{ps}^* \right\rangle & \left\langle J_{ss} J_{pp}^* \right\rangle & \left\langle J_{ss} J_{ps}^* \right\rangle \\ \left\langle J_{sp} J_{sp}^* \right\rangle & \left\langle J_{sp} J_{ss}^* \right\rangle & \left\langle J_{ss} J_{sp}^* \right\rangle & \left\langle J_{ss} J_{ss}^* \right\rangle \end{bmatrix} = \left\langle \mathbf{J} \otimes \mathbf{J}^* \right\rangle \tag{2.11}$$

where $\otimes$ stands for a Kronecker product. While the coherence vector $\mathbf{C}$ is transformed by $\mathbf{F}$, upon interaction with a sample the Stokes vector is transformed by the well-known Mueller matrix $\mathbf{M}$ [5–7]:

$$\mathbf{S}^{out} = \begin{pmatrix} I \\ Q \\ U \\ V \end{pmatrix}^{out} = \mathbf{M}\mathbf{S}^{in} = \begin{pmatrix} M_{11} & M_{12} & M_{13} & M_{14} \\ M_{21} & M_{22} & M_{23} & M_{24} \\ M_{31} & M_{32} & M_{33} & M_{34} \\ M_{41} & M_{42} & M_{43} & M_{44} \end{pmatrix} \cdot \begin{pmatrix} I \\ Q \\ U \\ V \end{pmatrix}^{in} \tag{2.12}$$

By combining (2.7), (2.10) and (2.11) we immediately obtain

$$\mathbf{M} = \mathbf{A}\,\mathbf{F}\,\mathbf{A}^{-1} = \mathbf{A}\,\left\langle \mathbf{J} \otimes \mathbf{J}^{*} \right\rangle\,\mathbf{A}^{-1} \tag{2.13}$$

which can be written in an expanded notation for a general case as:

$$\mathbf{M} = \begin{pmatrix} \frac{1}{2}\left\langle |J_{pp}|^2 + |J_{ss}|^2 + |J_{sp}|^2 + |J_{ps}|^2 \right\rangle & \frac{1}{2}\left\langle |J_{pp}|^2 - |J_{ss}|^2 + |J_{sp}|^2 - |J_{ps}|^2 \right\rangle & \left\langle \mathrm{Re}\left(J_{ps}J_{pp}^{*} + J_{ss}J_{sp}^{*}\right)\right\rangle & -\left\langle \mathrm{Im}\left(J_{ps}J_{pp}^{*} + J_{ss}J_{sp}^{*}\right)\right\rangle \\ \frac{1}{2}\left\langle |J_{pp}|^2 - |J_{ss}|^2 - |J_{sp}|^2 + |J_{ps}|^2 \right\rangle & \frac{1}{2}\left\langle |J_{pp}|^2 + |J_{ss}|^2 - |J_{sp}|^2 - |J_{ps}|^2 \right\rangle & \left\langle \mathrm{Re}\left(J_{ps}J_{pp}^{*} - J_{ss}J_{sp}^{*}\right)\right\rangle & \left\langle \mathrm{Im}\left(-J_{ps}J_{pp}^{*} + J_{ss}J_{sp}^{*}\right)\right\rangle \\ \left\langle \mathrm{Re}\left(J_{sp}J_{pp}^{*} + J_{ss}J_{ps}^{*}\right)\right\rangle & \left\langle \mathrm{Re}\left(J_{sp}J_{pp}^{*} - J_{ss}J_{ps}^{*}\right)\right\rangle & \left\langle \mathrm{Re}\left(J_{ss}J_{pp}^{*} + J_{sp}J_{ps}^{*}\right)\right\rangle & \left\langle \mathrm{Im}\left(-J_{ss}J_{pp}^{*} + J_{sp}J_{ps}^{*}\right)\right\rangle \\ \left\langle \mathrm{Im}\left(J_{sp}J_{pp}^{*} + J_{ss}J_{ps}^{*}\right)\right\rangle & \left\langle \mathrm{Im}\left(J_{sp}J_{pp}^{*} - J_{ss}J_{ps}^{*}\right)\right\rangle & \left\langle \mathrm{Im}\left(J_{ss}J_{pp}^{*} + J_{sp}J_{ps}^{*}\right)\right\rangle & \left\langle \mathrm{Re}\left(J_{ss}J_{pp}^{*} - J_{sp}J_{ps}^{*}\right)\right\rangle \end{pmatrix} \tag{2.14}$$

Of course, in the absence of depolarization, i.e. when the Jones matrix is well defined, the brackets meaning averages can be removed in (2.14). Furthermore, if the Jones matrix is diagonal, as it is the case for standard ellipsometry, only the upper left and lower right 2×2 sub-matrices do not vanish, and the Mueller matrix can be recast in terms of the ellipsometric angles Ψ and Δ as:

$$\mathbf{M}(\tau, \Psi, \Delta) = \tau \begin{pmatrix} 1 & -\cos(2\Psi) & 0 & 0 \\ -\cos(2\Psi) & 1 & 0 & 0 \\ 0 & 0 & \sin(2\Psi)\cos\Delta & \sin(2\Psi)\sin\Delta \\ 0 & 0 & -\sin(2\Psi)\sin\Delta & \sin(2\Psi)\cos\Delta \end{pmatrix} \tag{2.15}$$

Due to the capability of the Stokes vectors to describe *any* polarization state, the Mueller matrix can fully describe the polarimetric properties of *any* sample, be it depolarizing or not. In other words, Mueller polarimetry is the only technique able to fully characterize the polarization responses of any sample, in any measurement conditions.

In contrast with the Jones matrix, the Mueller matrix does not carry any information about the overall optical phase shift introduced by the sample. So, depending on whether the overall transmission (or reflectivity) of the sample is of interest or not, the Mueller matrix may be considered in its original or in its *normalized* form: in the latter case, all its elements are divided by the upper left element M_{11} which is set equal 1.

2.2.2.3 Coherence Matrix: Physical Realizability and Depolarizing Character of Mueller Matrices

The coherence matrix, **N**, is an interesting object, obtained from a smart rearrangement of the matrix **F**. To obtain the coherence matrix it is necessary to redefine the

Jones matrix in a "vector" form $\mathbf{J}^V$ as:

$$\left[\mathbf{J}^V\right]^T = \left(J_1^V, J_2^V, J_3^V, J_4^V\right) = \left(J_{pp}, J_{ps}, J_{sp}, J_{ss}\right) \tag{2.16}$$

then the matrix $\mathbf{N}$ can be expressed in terms of matrix $\mathbf{F}$ as:

$$\begin{aligned}\mathbf{N} = \left\langle \left[\mathbf{J}^V\right] \otimes \left(\left[\mathbf{J}^V\right]^T\right)^* \right\rangle &= \begin{bmatrix} \left\langle J_{pp}J_{pp}^* \right\rangle & \left\langle J_{pp}J_{ps}^* \right\rangle & \left\langle J_{pp}J_{sp}^* \right\rangle & \left\langle J_{pp}J_{ss}^* \right\rangle \\ \left\langle J_{ps}J_{pp}^* \right\rangle & \left\langle J_{ps}J_{ps}^* \right\rangle & \left\langle J_{ps}J_{sp}^* \right\rangle & \left\langle J_{ps}J_{ss}^* \right\rangle \\ \left\langle J_{sp}J_{pp}^* \right\rangle & \left\langle J_{sp}J_{ps}^* \right\rangle & \left\langle J_{sp}J_{sp}^* \right\rangle & \left\langle J_{sp}J_{ss}^* \right\rangle \\ \left\langle J_{ss}J_{pp}^* \right\rangle & \left\langle J_{ss}J_{ps}^* \right\rangle & \left\langle J_{ss}J_{sp}^* \right\rangle & \left\langle J_{ss}J_{ss}^* \right\rangle \end{bmatrix} \\ &= \begin{bmatrix} F_{11} & F_{12} & F_{21} & F_{22} \\ F_{13} & F_{14} & F_{23} & F_{24} \\ F_{31} & F_{32} & F_{41} & F_{42} \\ F_{33} & F_{34} & F_{43} & F_{44} \end{bmatrix}\end{aligned} \tag{2.17}$$

where the superscripts, T and $*$ stand for transposed and complex conjugated. When applied successively, they are equivalent to the Hermitian conjugate. The relation between the $\mathbf{N}$ and $\mathbf{F}$ matrices allows to combine expressions (2.17), (2.11) and (2.14) to write $\mathbf{N}$ in terms of the elements of the Mueller matrix $\mathbf{M}$ as:

$$\mathbf{N} = \frac{1}{2}\begin{bmatrix} M_{11}+M_{22}+ & M_{13}+M_{23}+ & M_{31}+M_{32}- & M_{33}+M_{44}+ \\ M_{12}+M_{21} & i(M_{14}+M_{24}) & i(M_{41}+M_{42}) & i(M_{34}-M_{43}) \\ M_{13}+M_{23}- & M_{11}-M_{22}- & M_{33}-M_{44}- & M_{31}-M_{32}- \\ i(M_{14}+M_{24}) & M_{12}+M_{21} & i(M_{34}+M_{43}) & i(M_{41}-M_{42}) \\ M_{31}+M_{32}+ & M_{33}-M_{44}+ & M_{11}-M_{22}+ & M_{13}-M_{23}+i \\ i(M_{41}+M_{42}) & i(M_{34}+M_{43}) & M_{12}-M_{21} & (M_{14}-M_{24}) \\ M_{33}+M_{44}- & M_{31}-M_{32} & M_{13}-M_{23}- & M_{11}+M_{22}- \\ i(M_{34}-M_{43}) & +i(M_{41}-M_{42}) & i(M_{14}-M_{24}) & M_{12}-M_{21} \end{bmatrix} \tag{2.18}$$

An alternative definition of the matrix $\mathbf{N}$, giving the same result as (2.17), has been proposed by [8]. As it can be seen, the coherence matrix has the same elements as the matrix $\mathbf{F}$, hence it carries the same information. By construction, the matrix $\mathbf{N}$ is Hermitian, implying its eigenvalues are real. This algebraic property will be used to define some of the Mueller matrix decompositions detailed in a forthcoming section, Sect. 2.4. Moreover by construction it can be easily seen that the coherence matrix has the form of a variance-covariance matrix. In the following, in order to keep the same terminology as other authors, we will refer to matrix $\mathbf{N}$ as coherence matrix instead of variance-covariance matrix.

2.2.2.4 Physical Realizability of Mueller Matrices

We already pointed out in paragraph 2.2.2.1 that any two dimensional complex vector may represent the Jones vector of a physically realizable polarization state, while a four dimensional real vector is not necessarily an acceptable Stokes vector, as its degree of polarization ρ_s must be comprised between 0 and 1.

The situation is quite analogous for Jones and Mueller matrices. Any 2×2 complex matrix is a physically acceptable Jones matrix (provided we consider the polarization behavior of optical amplifiers, to include matrices with coefficients having moduli larger than 1), while *any* 4×4 *real matrix* $\mathbf{M}$ *is not necessarily a physically realizable Mueller matrix*. An obvious necessary condition is that any acceptable Stokes vector must be transformed by $\mathbf{M}$ into another acceptable Stokes vector, with ρ_s between 0 and 1. However, this condition is not sufficient.

The real criterion of physical realizability of $\mathbf{M}$ as a Mueller matrix is directly related to our previous definition of a Mueller matrix as a linear combination of the second moments of a probabilistic (and not deterministic) Jones matrix. A necessary and sufficient condition for the existence of such matrix, and thus of the acceptability of $\mathbf{M}$ as a Mueller matrix is that *the matrix* $\mathbf{N}$ *calculated from* $\mathbf{M}$ *by* (2.18) *is an acceptable coherence matrix, i.e. that this Hermitian matrix is definite positive* [9, 10] (all eigenvalues are non-negative, and at least one is strictly positive).

2.2.2.5 Depolarizing and Non-Depolarizing Mueller Matrices

From the above definitions, it should be quite clear now that a non-depolarizing sample is characterized by a well-defined (deterministic) Jones matrix. As a result, all the averaging introduced in Eqs. (2.10), (2.11), (2.14) and (2.17) can be safely eliminated. If so, Eq. (2.17) shows that $\mathbf{N}$ can be seen as a "projector" of the C^4 space onto the vector $\mathbf{J}^V$.

Actually, a necessary and sufficient condition for a Mueller matrix $\mathbf{M}$ *to be non-depolarizing and equivalent to a Jones matrix* $\mathbf{J}$ *is that its coherence matrix* $\mathbf{N}$ *has only one strictly positive eigenvalue The eigenvector associated with this eigenvalue is the vector* $\mathbf{J}^V$ *related to* $\mathbf{J}$ *by* $\mathbf{J}^V$ (2.16).

As discussed later in Sect. 2.3.3 devoted to pure depolarizers, there are many ways to quantify the depolarizing character of a given sample, after more or less complex treatments of the Mueller matrix M. However, a very simple quantifier, the quadratic depolarization index P_q proposed by Gil [11] deserves a special mention here due to its ease of implementation:

$$P_q = \sqrt{\frac{\sum_{ij} M_{ij}^2 - M_{11}^2}{3M_{11}^2}} = \sqrt{\frac{trace(\mathbf{M}^T\mathbf{M}) - M_{11}^2}{3M_{11}^2}} \tag{2.19}$$

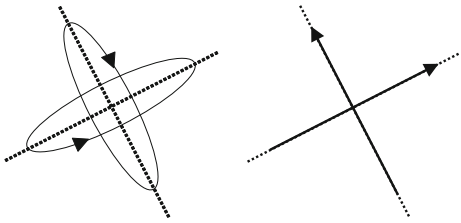

Fig. 2.3 *Left* a pair of elliptically polarized orthogonal states. *Right* a pair of linearly polarized orthogonal states

where the superscript T stands for the transpose operation and, *trace*, indicates the algebraic trace operator. The quadratic depolarization index P_q varies from 0, for a perfect depolarizer (only M_{11} is nonzero) to 1, for non-depolarizing matrices.

2.3 The Essential Polarimetric Properties of Any Sample

Generally speaking, the polarimetric response of a given sample describes how the incident light polarization is changed due to the interaction with the sample. In spite of its apparent complexity, this response can be rationalized in terms of three fundamental properties, namely the sample diattenuation, retardation, and depolarization. In many cases of practical interest, among which the usual ellipsometric characterization of isotropic materials or thin films, all these properties can be unambiguously defined from the measured data. The fundamental polarimetric properties used as "building blocks" to characterize more complex systems are given by pure diattenuators, pure retarders and depolarizers.

To understand these properties it is useful to use the concept of pairs of fully polarized orthogonal eigenstates, represented in Fig. 2.3. Each eigenstate is characterized by its length and ellipticity. An ellipticity equal to zero corresponds to linearly polarized light, an ellipticity equal to ± 1 corresponds to circularly polarized light, while other values of ellipticity correspond to elliptically polarized light. The sign of the ellipticity states the difference between clockwise or counterclockwise rotation. For the vast majority of usual polarization optical components, such as retardation plates or polarizers, these eigenstates are actually linearly polarized, (also shown in Fig. 2.3).

Linear diattenuators, which can be seen as partial linear polarizers, transmit (or reflect) each of their eigenstates without altering their ellipticity nor azimuth, but may change their intensities. Simple linear retarders, which can be assimilated to wave plates, transmit their eigenstates without changing their respective ellipticity, azimuth and intensity but modify their relative phases (or optical paths). These effects are schematically represented in Fig. 2.4.

In contrast with diattenuators and retarders, ideal depolarizers do not leave any polarization state invariant, excepted the totally depolarized one. Actually these components reduce the light degree of polarization ρ_s defined in (2.8). In particular, these

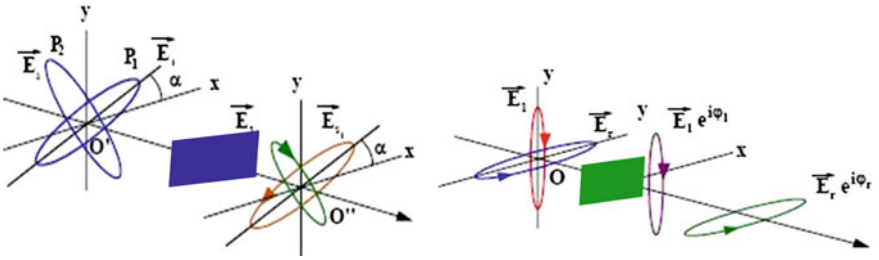

Fig. 2.4 Illustration of the transformation of polarization eigenstates by simple diattenuators (*left*) or simple retarders (*right*)

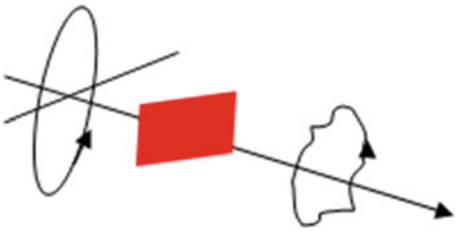

Fig. 2.5 Analogous to Fig. 2.4, for a typical depolarizer

components transform totally polarized states into partially polarized ones, as illustrated in Fig. 2.5.

As mentioned above, partially polarized states can be physically interpreted as incoherent superpositions of totally polarized states with different polarizations. As a result, a depolarizer can be described as an optical system with different non-depolarizing responses which add up incoherently. In practice, this occurs for samples featuring spatial, spectral or temporal inhomogeneities resulting in different output polarization states leading to intensity signals which are integrated by the detector. If retarders and diattenuators sharing the same eigenvectors are present in a sample or in a given medium, their combined effect on the final state of a polarized beam does not depend on the order on which each one appears; in other words, their polarization effects are commutative. The same is not true for a depolarizer. When combined with retardance and diattenuation, the position where depolarization takes place in the sample matters, and determines the final polarization state of the beam.

In the following we provide a description of each one of the elementary polarimetric properties together with a representation of the corresponding Mueller matrices. More details can be found in [12]. The matrix representation is the basis of a powerful method of interpretation of polarimetric measurements. The method consists on decomposing the measured Mueller matrix into basic polarimetric effects, and it will be detailed in a forthcoming section, Sect. 2.4.

2.3.1 Diattenuation and Linear Diattenuators (Polarizers)

Diattenuation, the polarimetric property of the diattenuators, is defined in practice by a scalar, called D, characterizing the maximum variation of transmitted (or reflected) light intensity with as a function of the incident polarization state. Diattenuation is defined as follows

$$D = \frac{I_{\max} - I_{\min}}{I_{\max} + I_{\min}} \tag{2.20}$$

where I_{max} and I_{min} correspond to the intensities of the two transmitted (or reflected) eigenstates. This definition recalls the definition of the ellipsometric angle Ψ. Indeed $\tan^2\Psi$ can be written as I_{max}/I_{min}. The square is justified because D is defined for intensities and Ψ for amplitudes of the electromagnetic field. From this relation it is easy to derive:

$$D = \frac{1 - \tan^2 \Psi}{1 + \tan^2 \Psi} = \cos 2\Psi. \tag{2.21}$$

For ideal linear polarizers, I_{min} is close to 0, (in practice the ratio $I_{\min}/I_{\max}$ is typically of the order of 10^{-3} to 10^{-6} $I_{\max}$), thus D is almost 1 and Ψ almost 0° or 90°. The notion of diattenuation can be further extended to a vector, which gives information about the orientation if diattenuator eigenstates. More specifically, if the vector diattenuation is defined as:

$$\mathbf{D} = D \begin{pmatrix} d_1 \\ d_2 \\ d_3 \end{pmatrix} = \begin{pmatrix} D_{horizontal} \\ D_{45^\circ} \\ D_{circular} \end{pmatrix} \tag{2.22}$$

with $d_1^2 + d_2^2 + d_3^2 = 1$, then the polarization eigenstates Stokes vectors $\mathbf{S}_{\min}$, $\mathbf{S}_{\max}$ are given by

$$\mathbf{S}_{\max}^T = (1, d_1, d_2, d_3,), \quad \mathbf{S}_{\min}^T = (1, -d_1, -d_2, -d_3,) \tag{2.23}$$

The three components of the diattenuation vector $\mathbf{D}$ define respectively the horizontal, the 45°, and the circular diattenuation. The vector diattenuation of any sample is a very simple function of the first row of the sample Mueller matrix:

$$\mathbf{D} = \frac{1}{M_{11}} \begin{pmatrix} M_{12} \\ M_{13} \\ M_{14} \end{pmatrix} \tag{2.24}$$

The Mueller matrix of a pure diattenuator can be expressed in terms of the scalar and the vector diattenuation as follows:

$$\mathbf{M} = \tau \begin{pmatrix} 1 & \mathbf{D}^T \\ \mathbf{D} & (\mathbf{m}_d) \end{pmatrix}; \quad \text{where} \quad \mathbf{m}_d = \sqrt{1 - D^2}\mathbf{I}_3 + \left(1 - \sqrt{1 - D^2}\right)\mathbf{D}\,\mathbf{D}^T \quad (2.25)$$

This Mueller matrix has been written in a contracted form. The elements of the first row and column are represented by the diattenuation vector. $\mathbf{m_d}$ is a 3×3 symmetric sub-matrix which is function of the identity (3×3) matrix, $\boldsymbol{I}_3$, the vector and the scalar diattenuation. Finally, τ represents the overall transmission or reflectivity or the sample when the incident light is totally depolarized.

For the practically very interesting case of linear diattenuators (e.g. whose eigenstates are linearly polarized) the Mueller matrix $\mathbf{M}_\mathrm{D}$ reads:

$$\mathbf{P} = \frac{\tau_P}{2} \begin{pmatrix} 1 & \cos(2\theta)\cos 2\Psi & \sin(2\theta)\cos 2\Psi & 0 \\ \cos(2\theta)\cos 2\Psi & \cos^2(2\theta) + \sin^2(2\theta)\sin 2\Psi & \cos(2\theta)\sin(2\theta)(1 - \sin 2\Psi) & 0 \\ \sin(2\theta)\cos 2\Psi & \cos(2\theta)\sin(2\theta)(1 - \sin 2\Psi) & \sin^2(2\theta) + \cos^2(2\theta)\sin 2\Psi & 0 \\ 0 & 0 & 0 & \sin 2\Psi \end{pmatrix} \quad (2.26)$$

where θ is the azimuth of the high transmission polarization direction with respect to the x axis and Ψ is the ellipsometric angle. The diattenuator vector takes the particularly simple form

$$\mathbf{D} = \cos 2\Psi \begin{pmatrix} \cos 2\theta \\ \sin 2\theta \\ 0 \end{pmatrix} \quad (2.27)$$

2.3.2 Retardance and Linear Retarders

The time delay generated between two eigenstates after propagation through a pure retarder is represented by the scalar retardance, R. In a frequency representation of the electromagnetic fields, the time delay is represented by the phase difference between the two eigenstates. Similarly to the diattenuation, it is possible to define a vector retardance, $\mathbf{R}$, as

$$\mathbf{R} = R \begin{pmatrix} r_1 \\ r_2 \\ r_3 \end{pmatrix} = \begin{pmatrix} R_H \\ R_{45^\circ} \\ R_C \end{pmatrix} \quad (2.28)$$

with $r_1^2 + r_2^2 + r_3^2 = 1$. Again, the Stokes vectors of the fast and slow eigenstates $\mathbf{S}_\mathrm{f}$, $\mathbf{S}_\mathrm{s}$ are given respectively by

$$\mathbf{S}_f^T = (1, r_1, r_2, r_3,), \quad \mathbf{S}_s^T = (1, -r_1, -r_2, -r_3,) \quad (2.29)$$

A pure retarder can be described geometrically as rotation in the space of Stokes vectors. Mathematically the Mueller matrix $\mathbf{M}_\mathrm{R}$ of the retarder can be written in compact notation as:

$$\mathbf{M}_R = \begin{pmatrix} 1 & \mathbf{0}^T \\ \mathbf{0} & \mathbf{m_R} \end{pmatrix}, \quad \text{and} \quad (\mathbf{m_R})_{ij} = \delta_{ij}\cos(R) + r_i r_j\,(1-\cos R)\sum_{k=1}^{3}\varepsilon_{ijk} r_k \sin R \tag{2.30}$$

where the 3×3 sub-matrix, $\mathbf{m_R}$, is orthogonal and has a unit determinant, $\det(\mathbf{m_R}) = +1$. $\mathbf{0}$ represents the null vector. δ_{ij} is the Kronecker symbol, and $\varepsilon_{\mathrm{ijk}}$ is the Levi-Civita permutation sign. Scalar and vector retardances can be easily determined from the measured Mueller matrices as follows:

$$R = \cos^{-1}\left(\frac{trace\,(M_R)}{2} - 1\right) \tag{2.31}$$

$$r_i = \frac{1}{2\sin R}\sum_{j,k=1}^{3}\varepsilon_{ijk}(\mathbf{m_R})_{jk} \tag{2.32}$$

Again, the case of linear retarders is of particular interest. For such a component, with its fast axis oriented at an azimuth, θ, with respect to the x axis and a scalar retardation Δ, the Mueller matrix reads :

$$\mathbf{M}_R(\theta,\Delta) = \tau_R \begin{pmatrix} 1 & 0 & 0 & 0 \\ 0 & \cos^2(2\theta)+\sin^2(2\theta)\cos(\Delta) & \cos(2\theta)\sin(2\theta)\,(1-\cos(\Delta)) & -\sin(2\theta)\sin(\Delta) \\ 0 & \cos(2\theta)\sin(2\theta)\,(1-\cos(\Delta)) & \sin^2(2\theta)+\cos^2(2\theta)\cos(\Delta) & \cos(2\theta)\sin(\Delta) \\ 0 & \sin(2\theta)\sin(\Delta) & -\cos(2\theta)\sin(\Delta) & \cos(\Delta) \end{pmatrix} \tag{2.33}$$

It is straightforward to check that the scalar retardation R given by (2.31) is nothing else but the ellipsometric angle Δ, and the retardance vector is

$$\mathbf{R} = \Delta \begin{pmatrix} \cos 2\theta \\ \sin 2\theta \\ 0 \end{pmatrix} \tag{2.34}$$

2.3.3 Depolarization and Pure Depolarizers

The Mueller matrix of a general depolarizer, $\mathbf{M}_\boldsymbol{\delta}$, is given in compact notation by:

$$\mathbf{M}_\delta = \begin{pmatrix} 1 & \mathbf{0}^T \\ \mathbf{0} & \mathbf{m}_\delta \end{pmatrix} \tag{2.35}$$

where $\mathbf{m_\delta}$ is a 3×3 real symmetric matrix. Thus this matrix can be reduced to a diagonal form in a suitable orthonormal basis formed by three (3-dimensional) eigenvectors $\mathbf{v}_\mathrm{i}$. As a result, in a basis formed by the four Stokes vectors

$$\mathbf{S}_0^T = (1, 0, 0, 0,), \quad \text{and} \quad \mathbf{S}_i^T = \left(1, \mathbf{v}_i^T\right), (1 \leq i \leq 3) \tag{2.36}$$

the Mueller matrix M_δ of the depolarizer becomes diagonal

$$\mathbf{M}_\delta = \begin{pmatrix} 1 & 0 & 0 & 0 \\ 0 & a & 0 & 0 \\ 0 & 0 & b & 0 \\ 0 & 0 & 0 & c \end{pmatrix} \tag{2.37}$$

where the eigenvalues a, b, c of $\mathbf{m}_\delta$ are real numbers comprised between -1 and 1. The Eq. (2.37) above shows that for the three Stokes vectors $\mathbf{S}_\mathrm{i}$ defined in (2.36) the degree of polarization is reduced by a factor equal to the corresponding eigenvalue a, b or c, while the totally depolarized state remains unchanged. In other words, a general depolarizer features only one eigenpolarization, corresponding ot a totally depolarized state.

Due to the symmetry of $\mathbf{m}_\delta$, the Mueller matrices of pure depolarizers defined in (2.35), clearly depend on six parameters, i.e. the independent components of $\mathbf{m}_\delta$. Another possible choice, which may be more physically relevant, are the three eigenvalues a, b, and c, and the three Euler angles defining the directions of the normalized vectors $\mathbf{v}_\mathrm{i}$ in the three dimensional space of the (Q, U, V) coordinates of Stokes vectors.

Due to this dependence on six parameters, in the most general case, depolarizers are more mathematically complex than retarders or diattenuators, which involve only three parameters each. Fortunately, in many situations of physical interest the symmetry properties of the sample greatly reduce the number of independent parameters. For example, when observed in forward or backward scattering geometries a suspension of spherical (or statistically isotropic) scatterers behaves as a pure depolarizer with different depolarization powers for linearly and circularly polarized incident states. Moreover, for the particular case of a suspension of spheres, the depolarization power for linear states is independent of the orientation of the incident polarization. Mathematically, these intuitive properties can be reformulated as

$$a = b \neq c \quad \text{and} \quad v_1^T = (\cos\alpha, \sin\alpha, 0), \quad v_2^T = (-\sin\alpha, \cos\alpha, 0), \quad v_3^T = (0, 0, 1) \tag{2.38}$$

where α can be chosen arbitrarily.

However, as depolarizers are studied not only for their own sake but also to characterize the depolarizing properties of more general Mueller matrices by mathematical treatments presented in the next section, it is desirable to define a single numeri-

cal function defining the "overall" depolarizing power of a depolarizer, and which would vary from 0 to 1, these extreme values being reached for nondepolarizing matrices and for total depolarizers respectively. A first example of such function is the quadratic depolarization index P_q defined in Eq. (2.19) for a general Mueller matrix, and obviously applies also to pure depolarizers. Another possible definition has been given specifically for depolarizers by Lu and Chipman [12].

$$\delta = 1 - \frac{1}{3}\left(|a| + |b| + |c|\right) \tag{2.39}$$

Finally, we point out that the best definition of an "overall" depolarizing power depends on the system under consideration. This is an open field, with many new definitions being proposed [13, 14].

2.3.4 Polarizance: Homogeneous and Inhomogeneous Systems

The concept of polarizance is linked to the ability of a sample to increase the degree of polarization of an initially non-polarized beam. This increase can be done either by a selective reorientation or by a selective elimination of certain vibration directions of the electric field. Mathematically this concept is expressed as follows:

$$\mathbf{S}_{out} = \begin{pmatrix} M_{11} \\ M_{21} \\ M_{31} \\ M_{41} \end{pmatrix} = \begin{pmatrix} M_{11} & M_{12} & M_{13} & M_{14} \\ M_{21} & M_{22} & M_{23} & M_{24} \\ M_{31} & M_{32} & M_{33} & M_{34} \\ M_{41} & M_{42} & M_{43} & M_{44} \end{pmatrix} \cdot \begin{pmatrix} 1 \\ 0 \\ 0 \\ 0 \end{pmatrix} \tag{2.40}$$

The degree of polarization of the Stokes vector representing the final state of the beam is called scalar polarizance P. Moreover, in analogy with the vector diattenuation and the vector retardance the vector polarizance $\mathbf{P}$ can be defined from the Mueller matrix elements of the polarizing element as:

$$P = \frac{\sqrt{M_{21}^2 + M_{31}^2 + M_{41}^2}}{M_{11}^2} \quad \text{and} \quad \mathbf{P} = \frac{1}{M_{11}} \begin{pmatrix} M_{21} \\ M_{31} \\ M_{41} \end{pmatrix} \tag{2.41}$$

For many systems, the diattenuation and polarizance vectors are equal: $\mathbf{P} = \mathbf{D}$. Such systems are said to be *homogeneous*. The diattenuators and the retarders respectively defined in Sects. 2.3.1 and 2.3.2 are indeed homogeneous.

At first glance a diattenuating system may seem necessary to partially polarize an initially unpolarized beam. The emerging polarization being directly determined by the diattenuation vector $\mathbf{D}$, one might expect that in all cases $\mathbf{P} = \mathbf{D}$, and thus the notion of polarizance would eventually be pointless. This is not true, as we now show with very simple examples of inhomogeneous systems.

- Let us first consider a setup consisting of a *polarizer followed by a perfect depolarizer*. Such a system clearly exhibits diattenuation, as the intensity transmitted by the polarizer depends on the incoming polarization. However, the beam emerging from the depolarizer is, by definition, totally depolarized, implying that an initially depolarized beam would remain totally depolarized. As a result, such a system exhibits a strong diattenuation but no polarizance.
- Let us now consider the same elementary components, but *in reverse order* (depolarizer first, polarizer afterwards). In this case, any incoming polarized beam is transformed by the depolarizer into a totally depolarized beam whose intensity does not depend on the incoming polarization. Then, the polarizer transforms this beam into a polarized one, with always the same polarization. In contrast with the previous case, now the system exhibits zero diattenuation but a strong polarizance ($P = 1$ for a perfect polarizer).

2.3.5 Summary

In this part, we have introduced the "elementary" polarimetric properties, namely diattenuation, retardance, depolarization and polarizance. As diattenuation, retardance and polarizance are defined by 3D non-normalized vectors, each of them depends on three independent parameters. On the other hand, we have seen that depolarization depends on another six parameters. So, all these polarimetric properties imply 15 independent parameters, as expected for normalized Mueller matrices (M_{11}, which is an overall transmission factor, is irrelevant for polarimetry).

However, the elementary polarimetric properties of a given Mueller matrix cannot be defined unambiguously. As shown in the next section, several decomposition procedures may be used to retrieve these properties, the final results depending on the chosen decomposition. For a correct interpretation of the data, it is therefore essential to choose properly the decomposition best adapted to the system under study, if available in the "toolbox".

2.4 Mueller Matrix Algebra: Decomposition of Mueller Matrices

Ideally, any polarimetric measurement should be interpreted by fitting to the measured Mueller matrices numerical simulations based on a relevant model, as it is very commonly done with standard ellipsometry studies of samples like stacks of isotropic thin films on plane substrates. Unfortunately this is far from being always possible with the "complex" and/or "disordered" samples such as biological tissues, which exhibit depolarization and justify the use of Mueller polarimetry. For such samples accurate models of their polarimetric responses are very difficult to elaborate.

In the absence of adequate physical models, experimental Mueller matrices can still be phenomenologically interpreted by decomposing them into simpler components with well-defined polarimetric properties. Basically, Mueller matrix decompositions can be classified into two groups:

- *sum decompositions*: Sum decompositions treat a depolarizing Mueller matrix as an incoherent addition of non-depolarizing matrices. Sum decompositions are primarily used to assess the physical realizability of the measured Mueller matrix, a condition which is not necessarily satisfied due to experimental errors, and to "filter" out the contribution these errors if needed. In other cases sum decompositions allow to isolate the individual non-depolarizing Mueller matrices which contribute to a measured depolarizing matrix.
- *product decompositions*, which describe the sample as a stack of elementary samples traversed sequentially by the light beam. These decompositions are mostly used to evaluate the diattenuation, retardation, depolarization and polarizance of the input Muller matrix, and, in some cases, to locate the various elementary polarization properties inside the sample.

2.4.1 Sum Decompositions

Sum decompositions treat the depolarizing Mueller matrix as an incoherent addition of non-depolarizing matrices. The physical image behind these decompositions is that of a beam which does not shine a single sample, but on N different ones at the same time. Consequently each sample transmits of reflects, simultaneously and independently of the other samples, a portion of the beam. To complete the image we consider that a unique detector integrates incoherently (without interferences) and simultaneously the light coming from all the N samples. An electrical analogue would be a circuit comprising N resistances connected in parallel. A current flow, arriving to the circuit, splits, and a portion of the total intensity current goes through each resistance. Once the individual current flows have gone through the resistances, they sum up again at the output of the circuit.

Sum decompositions are very useful because they may represent physical situations frequently encountered in ellipsometric measurements. Incoherent superpositions of differently polarized contributions may be caused by the sample or by the measurement system itself. Typical examples of such situations are

(a) *multiple reflections* by the double face of substrates thicker than the light coherence length, typically of the order of 0.2 mm for most spectroscopic ellipsometers.
(b) *Spatially inhomogenous samples*. Many examples can be found in this category which have in common the fact that the probe beam is much larger than the characteristic size of homogeneous zones. Thus the beam illuminates a region of the sample with different optical responses. Once all of these responses arrive at the detector they add-up incoherently and generate depolarization.

(c) *Tightly focused beams*. The reduction of beam spot sizes sometimes involves the creation of highly divergent (convergent) beams incident on the sample. A highly divergent or convergent can be understood as a bundle of well collimated beams with a specific angle of incidence each. As a result, the reflected beam is also divergent and contains a "bundle" of optical responses, which add-up incoherently when they are detected.

Many other examples can still be found which shows the interest for a decomposition which simplifies the analysis of data.

2.4.1.1 Cloude Decomposition

The most popular sum decomposition is known as the Cloude decomposition [15, 16]. Accordingly, any depolarizing matrix $\mathbf{M}$ can be represented as a weighted sum of up to four non-depolarizing Mueller matrices $\mathbf{M_i}$ in the following way:

$$\mathbf{M} = \lambda_1\mathbf{M}_1 + \lambda_2\mathbf{M}_2 + \lambda_3\mathbf{M}_3 + \lambda_4\mathbf{M}_4, \tag{2.42}$$

with the weight factors λ_i being positive. To form the decomposition, it is necessary to evaluate the coherence matrix $\mathbf{N}$ from the original Mueller matrix $\mathbf{M}$ via the $\mathbf{F}$ matrix by Eqs. (2.11) and (2.17). Then, let the eigenvalues and the normalized eigenvectors of $\mathbf{N}$ be λ_i and $\mathbf{e}_i$, respectively. The coherence matrices $\mathbf{N}_i$ of the *non-depolarizing* components $\mathbf{M}_i$ are given by

$$\mathbf{N_i} = \mathbf{e}_i\mathbf{e}_i^{\dagger} \tag{2.43}$$

where the symbol † stands for Hermitian conjugate Comparison of (2.43) and (2.18) immediately shows that $\mathbf{e}_i$ is nothing else but the vector form $\mathbf{J}_i^V$ defined in (2.16) of the Jones matrix $\mathbf{J}_i$ associated with the nondepolarizing matrix $\mathbf{M}_i$. Finally, the matrices $\mathbf{M}_i$ can be derived from J_i by using (2.14).

As shown previously, for a physically realizable Mueller matrix, the corresponding coherence matrix $\mathbf{N}$ is positive semi-definite and therefore, has non-negative eigenvalues λ_i that are usually sorted according to $\lambda_1 \geq \lambda_2 \geq \lambda_3 \geq \lambda_4$. Conversely, if $\lambda_4 < 0$ for instance, the matrix $\mathbf{M}$ is unphysical, i.e. $\mathbf{M}$ may transform a valid input Stokes vector into an invalid output one. When the Mueller matrix to be measured is non- or very weakly depolarizing, measurement errors may easily make it nonphysical. In such cases, Cloude decomposition provides a convenient tool to "filter out" the effect of such errors and make the measured matrix physical: to this end, once the eigenvalues λ_i and non-depolarizing matrices $\mathbf{M}_i$ are obtained, the (presumably small) negative eigenvalues are set equal to zero, and the relationship (2.42) is used one more to reconstruct a physically acceptable matrix close to the initially measured one.

In general *for a spatially inhomogeneous system the non-depolarizing components* $\mathbf{M}_i$ *do not correspond to actual physical Mueller matrices corresponding to different parts of the system* ! A simple reason for that is that the eigenvectors $\mathbf{e}_i$, of $\mathbf{N}$ form

an orthonormal basis. Then the matrices $\mathbf{M}_i = \mathbf{e}_i\mathbf{e}_i^\dagger$ have special properties which are not necessarily verified by the actual physical Mueller matrices of different parts of the system. To retrieve such matrices, and thus fully characterize such systems in spite of their inhomogeneity, more information than the simple knowledge of $\mathbf{M}$ is needed. An example of such characterization is described in Sect. 2.7.2.

2.4.1.2 Le Roy-Bréhonnet Decomposition

A special case of Cloude decomposition is that proposed by Le Roy-Bréhonnet et al. [17] representing $\mathbf{M}$ as the sum of a non-depolarizing Mueller matrix $\mathbf{M}_{nd}$ and an ideal diagonal depolarizer $\mathbf{M}_{id}$ (i.e., the kind of depolarizer introduced in the preceding section with null diagonal elements $a = b = c = 0$):

$$\mathbf{M} = \mathbf{M}_{nd} + \mathbf{M}_{id} \tag{2.44}$$

Unlike Cloude decomposition which is valid for an arbitrary depolarizing Mueller matrix, Le Roy-Bréhonnet expression is valid only if the condition $\lambda_2 = \lambda_3 = \lambda_4$ ($\neq \lambda_1$) is fulfilled. Le Roy-Bréhonnet decomposition offers another way to filter noisy experimental Mueller matrices of non-depolarizing samples. The procedure attributes to $\mathbf{M}_{nd}$ the whished matrix and to $\mathbf{M}_{id}$ the noise.

2.4.2 Product Decompositions

Product decompositions represent an arbitrary Mueller matrix as a product of elementary Mueller matrices—diattenuators, retarders and depolarizers. These decompositions are characterized by the number of elementary components and their respective positions in the multiplication. The order of the components is important since depolarizer matrices do not commute with diattenuator nor with retarder matrices. In principle, product decompositions are adequate to describe physical situations in which the beam interacts sequentially with different parts of the sample, each of which being characterized by a well-defined fundamental polarization property.

An *ad-hoc* example of such situation is the propagation of a beam through a wedge made of an anisotropic material with a rough output face. We assume that the input face is tilted with respect to the propagation direction, whereas the rough surface is perpendicular to the output beam. Then the tilted plane surface introduces diattenuation due the difference in transmission coefficients for *s* and *p* polarizations, the propagation though the bulk crystal introduces retardation, and the scattering on the rough output surface may depolarize. Accordingly, the Mueller matrix $\mathbf{M}$ of the wedge can be represented by a matrix multiplication of the form $\mathbf{M} = \mathbf{M}_{\delta P}\mathbf{M}_R\mathbf{M}_D$ with elementary Mueller matrices in this order. $\mathbf{M}_{\delta P}$, $\mathbf{M}_R$, $\mathbf{M}_D$ are the Mueller matrices of the depolarizer, the retarder and the diattenuator respectively.

Of course, situations in which one knows very well a priori the right order of the elementary components are very rare in "real life" applications. Thus various product decompositions have been (and are still being) developed to better cope with complex situations.

2.4.2.1 Forward and Reverse Decompositions into Three Factors

All these decompositions describe the input matrix $\mathbf{M}$ as a product of a diattenuator, a retarder, and a depolarizer. Actually with three elementary component types, there are six different possible orders. Among these, the most widely used choice is that chosen by Lu and Chipman [12], namely:

$$\mathbf{M} = \mathbf{M}_{\delta\mathbf{P}}\, \mathbf{M}_{\mathrm{R}}\, \mathbf{M}_{\mathrm{D}} \tag{2.45}$$

where the "special" symbol $\mathbf{M}_{\delta\,\mathbf{P}}$ had been used for the depolarizer. Actually, for this decomposition to be quite general, if the diattenuator and the retarder are of the forms defined in Sects. 2.3.1 and 2.3.2, then the depolarizer cannot be a "pure" depolarizer of the form defined in Sect. 2.3.3, as the product matrix $\mathbf{M}$ would exhibit no polarizance (three parameters are missing). As a result, the "depolarizer" has nonzero polarizance and its matrix is of the form:

$$\mathbf{M}_{\delta\mathbf{P}} = \begin{pmatrix} 1 & \mathbf{0}^T \\ \mathbf{P} & \mathbf{m}_\delta \end{pmatrix} \tag{2.46}$$

With these assumptions the procedure is numerically stable and always provides physically realizable elementary matrices $\mathbf{M}_{\delta\,\mathbf{P}}$, $\mathbf{M}_{\mathrm{R}}$ and $\mathbf{M}_{\mathrm{D}}$. This procedure is thus very convenient and is widely used for the phenomenological interpretation of experimental (or even simulated) Mueller matrices.

What happens if the order of the elementary components is changed? A very simple calculation shows that the above results are easily generalized to the other two cases in which the diattenuator precedes the depolarizer, namely

$$\mathbf{M} = \mathbf{M}'_{\mathrm{R}}\, \mathbf{M}'_{\delta\mathbf{P}}\, \mathbf{M}'_{\mathrm{D}} \quad \text{or} \quad \mathbf{M} = \mathbf{M}''_{\delta\mathbf{P}}\, \mathbf{M}''_{\mathrm{D}}\, \mathbf{M}''_{\mathrm{R}} \tag{2.47}$$

More precisely, the depolarizer matrices keep the form defined in (2.46) and the $\mathbf{M}'$ and $\mathbf{M}''$ matrices are deduced from those provided by the standard decomposition (2.45) by unitary transformations.

This kind of simple generalization is no longer valid for the three cases in which the depolarizer precedes the diattenuator. Morio and Goudail [18] introduced a "reverse" decomposition procedure for these three cases with the same definition of the depolarizer, but this procedure could lead to unstable or even unphysical results in case of very strong depolarizations. This issue has been solved by Ossikovski et al. [19] assuming that when the depolarizer precedes the diattenuator, the former features zero polarizance. The "standard" reverse decomposition takes then the form:

$$\mathbf{M} = \mathbf{M}_{\mathrm{D}}\, \mathbf{M}_{\mathrm{R}}\, \mathbf{M}_{\mathrm{D}'\delta} \tag{2.48}$$

with a depolarizer matrix of the form:

$$\mathbf{M}_{\mathrm{D}'\delta} = \begin{pmatrix} 1 & \mathbf{D}'^{T} \\ \mathbf{0} & \mathbf{m}_{\delta} \end{pmatrix} \tag{2.49}$$

As in the case of "direct" decompositions, the matrices of the three possible "reverse" cases (i.e. when the depolarizer precedes the diattenuator) are deduced from one another by simple orthogonal transformations. This procedure too is stable and always provides physically realizable Mueller matrices for the elementary components.

2.4.2.2 Symmetric Decompositions

The symmetric decomposition was first introduced for non-depolarizing Mueller matrices [20] in the following form:

$$\mathbf{M} = \mathbf{M}_{\mathrm{LR2}}\, \mathbf{M}_{\Psi\Delta}\, \mathbf{M}_{\mathrm{LR1}} \tag{2.50}$$

where $\mathbf{M}_{\mathrm{LR1}}$ and $\mathbf{M}_{\mathrm{LR2}}$ represent *linear* retarders, and $\mathbf{M}_{\Psi\Delta}$ is a *linear* retarding diattenuator with known orientation of its common diattenuation and retardation axes (like in standard ellipsometry, where these axes are along *s* and *p* directions). The procedure allowing to retrieve the three matrices $\mathbf{M}_{\mathrm{LR1}}$, $\mathbf{M}_{\Psi\Delta}$ and $\mathbf{M}_{\mathrm{LR2}}$ from $\mathbf{M}$ has been experimentally validated by measuring the Mueller spectra of a standard ellipsometric sample (10 nm of SiO2 on a c-Si substrate) with and without inserting retardation plates in the input and output beams [21]. A possible application of this procedure could be the elimination of the effect of birefringence of strained windows for in situ ellipsometric measurements.

This procedure was subsequently generalized to depolarizing Mueller matrices, which could be decomposed according to [22]

$$\mathbf{M} = \mathbf{M}_{\mathrm{D2}}\, \mathbf{M}_{\mathrm{R2}} \mathbf{M}_{\mathrm{d}\,\delta}\, \mathbf{M}_{\mathrm{R1}}\, \mathbf{M}_{\mathrm{D1}} \tag{2.51}$$

where $\mathbf{M}_{\mathrm{D1}}$ and $\mathbf{M}_{\mathrm{D2}}$ represent generic diattenuators of the form defined in Sect. 2.2.1, $\mathbf{M}_{\mathrm{R1}}$ and $\mathbf{M}_{\mathrm{R2}}$ generic retarders, and $\mathbf{M}_{\mathrm{d}\,\delta}$ a diagonal depolarizer. The central position of the depolarizer in the symmetric decomposition can be very useful for samples which can be viewed as purely depolarizing media limited by tilted input and output interfaces: in this case the diattenuation and retardation effects are likely to occur at the output interfaces and the depolarization in between. Moreover, in many cases of practical interest the Mueller matrix of the depolarizer is indeed diagonal.

However, this decomposition has two essential limits:

- $\mathbf{M}_{\mathrm{d}\,\delta}$ an take a diagonal form if, and only if, the eigenvector related to the largest eigenvalue of the matrix product $\mathbf{M}' = \mathbf{G}\,\mathbf{M}^T\,\mathbf{G}\,\mathbf{M}$ is *not* fully polarized, which is quite generally, but not always the case. If so, $\mathbf{M}$ can be termed "*Stokes diagonalizable*" and the procedure may be used
- Assuming $\mathbf{M}$ Stokes diagonalizable the depolarizer should be *nondegenerate*, i.e. its three diagonal elements a, b, c (other than M_{11}, set equal to 1) must be different from each other. Otherwise, $\mathbf{M}_{\mathrm{d}\,\delta}$ may commute with $\mathbf{M}_{\mathrm{R}1}$ and $\mathbf{M}_{\mathrm{R}2}$, and if so only the product $\mathbf{M}_{\mathrm{R}1}\mathbf{M}_{\mathrm{R}2}$ can be determined unambiguously.

This decomposition has been thoroughly studied experimentally. First, its validity has been demonstrated on an *ad hoc* system including nondegenerate and degenerate depolarizers set between retarders and diattenuators [23]. In both cases, the achieved accuracy was better than that of forward or reverse decompositions. Then a system with a non-Stokes diagonalizable Mueller matrix was implemented and studied [24], and finally it was shown that such matrices may occur in natural photonic systems, such as the cuticles of beetles [25].

2.4.2.3 Logarithmic Decomposition

The logarithmic decomposition was proposed recently as a complementary alternative to the standard product decompositions. This decomposition is a natural generalization [26] of the classic differential matrix formalism [27] to the depolarizing case. The approach, based on the physical picture of a continuously distributed depolarization, parallels and complements the product decomposition approach whereby depolarization is modeled as a spatially localized "lump" phenomenon. In particular, the differential matrix methodology appears as particularly well adapted to the phenomenological description of the continuous scattering in turbid media. According to this decomposition, the space derivative along the propagation direction z of a Mueller matrix $\mathbf{M}$ can be expressed as:

$$\frac{d\mathbf{M}}{dz} = \mathbf{m}\mathbf{M} \tag{2.52}$$

For a non-depolarizing medium, the (4×4) differential matrix $\mathbf{m}$ contains all the seven elementary properties of the medium and is given by:

$$\mathbf{m} = \begin{pmatrix} \alpha & \beta & \gamma & \delta \\ \beta & \alpha & \mu & \nu \\ \gamma & -\mu & \alpha & \eta \\ \delta & -\nu & -\eta & \alpha \end{pmatrix} \tag{2.53}$$

in which α is the isotropic absorption, β is the linear dichroism along the x–y laboratory axes, γ is the linear dichroism along the $\pm 45°$ axes, δ is the circular dichroism,

η is the linear birefringence along the x–y axes, ν is the linear birefringence along the $\pm 45°$ axes and μ is the circular birefringence [27]. Note that $\mathbf{m}$ is z (z the direction of light propagation) dependent in the general case of longitudinally inhomogeneous medium. If the medium can be considered homogeneous in the z direction over a distance, d, expression (2.52) can be easily integrated giving:

$$\mathbf{M} = \exp(\mathbf{m}d) = \exp(\mathbf{L}) \tag{2.54}$$

which can be also written as:

$$\ln(\mathbf{M}) = \mathbf{m}d = \mathbf{L} \tag{2.55}$$

This expression indicates that the fundamental properties of the medium in consideration can be easily deduced from the simple logarithm of the related Mueller matrix if the total thickness d is known.

When the medium shows depolarization, the matrix $\mathbf{m}$ must be substituted by matrix $\mathbf{m}'$:

$$\mathbf{m}' = \begin{pmatrix} \alpha & \beta'' & \gamma'' & \delta'' \\ \beta' & \alpha_1 & \mu'' & \nu'' \\ \gamma' & -\mu' & \alpha_2 & \eta'' \\ \delta' & -\nu' & -\eta' & \alpha_3 \end{pmatrix} \tag{2.56}$$

According to this representation, the primed and the double primed betas, β' and β'', are still related to the linear dichroism in the x–y laboratory axis. Similarly, γ' and γ'' are related to the linear dichroism along the $\pm 45°$ axes, δ' and δ'' are related to the circular dichroism, η' and η'' are related to the linear birefringence along the x–y axes, ν' and ν'' are related to the linear birefringence along the $\pm 45°$ axes and μ' and μ'' are related to the circular birefringence.

As discussed in Sect. 2.2.2.2, a depolarizing Mueller matrix can be seen as a statistical superposition of non-depolarizing Mueller matrices. As a result, the matrix $\mathbf{m}'$ can also be interpreted as a statistical superposition of matrices of the form given by (2.53), which are the only differential ones for which diattenuation and birefringence may be unambiguously defined. Then, for $\mathbf{m}'$ all we can define are estimates of the polarimetric fundamental parameters, together with the uncertainties affecting these estimates.

Following the idea behind the Le Roy-Bréhonnet decomposition, it is possible to decompose a matrix $\mathbf{m}'$ into the sum of two components, a non-depolarizing component and a purely depolarizing one, represented by the matrices $\mathbf{m_m}$ and $\mathbf{m_u}$ respectively. The first matrix, $\mathbf{m_m}$, has the same shape and symmetry properties as $\mathbf{m}$ in (2.53), therefore it represents a non-depolarizing component. Accordingly, $\mathbf{m_u}$ represents the depolarizing component. Matrices $\mathbf{m_m}$ and $\mathbf{m_u}$ can be easily deduced from:

$$\text{If } \mathbf{m}' = \mathbf{m_m} + \mathbf{m_u} \quad \text{then,} \quad \mathbf{m_m} = \frac{1}{2}\left(\mathbf{m}' - \mathbf{G}\mathbf{m}'^{T}\mathbf{G}\right), \quad \text{and} \quad \mathbf{m}_u = \frac{1}{2}\left(\mathbf{m}' + \mathbf{G}\mathbf{m}'^{T}\mathbf{G}\right) \tag{2.57}$$

in which $\mathbf{G}$ is a diagonal matrix, $\mathbf{G} = \mathrm{diag}(1, -1, -1, -1)$ and the superscript T stands for the transpose. The latter expression written in an extended notation leads to:

$$\mathbf{m_m} = \frac{1}{2}\begin{pmatrix} 2\alpha & \beta'+\beta'' & \gamma'+\gamma'' & \delta'+\delta'' \\ \beta'+\beta'' & 2\alpha_1 & \mu'+\mu'' & \nu'+\nu'' \\ \gamma'+\gamma'' & \mu'+\mu'' & 2\alpha_2 & \eta'+\eta'' \\ \delta'+\delta'' & \nu'+\nu'' & \eta'+\eta'' & 2\alpha_3 \end{pmatrix} \quad \text{and}$$
$$\mathbf{m}_u = \frac{1}{2}\begin{pmatrix} 0 & \beta'-\beta'' & \gamma'-\gamma'' & \delta'-\delta'' \\ \beta'-\beta' & 0 & \mu'+\mu'' & \nu'-\nu'' \\ \gamma''-\gamma' & \mu''-\mu' & 0 & \eta'-\eta'' \\ \delta''-\delta' & \nu''-\nu' & \eta''-\eta' & 0 \end{pmatrix} \tag{2.58}$$

What is the physical meaning of the elements of the matrices $\mathbf{m_m}$ and $\mathbf{m_u}$? The random character of depolarization leads to a statistical interpretation of these two matrices. According to (2.17) all the off-diagonal terms of $\mathbf{m_m}$ represent the average of the prime and double prime estimations of each one of the fundamental properties. Therefore, the off-diagonal terms of $\mathbf{m_m}$ are interpreted to be the most probable statistical estimates of each fundamental property. The main diagonal of $\mathbf{m_m}$ has four entries, the isotropic absorption α, and the anisotropic absorptions α_1, α_2 and α_3 along the x–y, the $\pm 45°$ and the circular axes respectively, which characterize the type of depolarization affecting the sample. The off-diagonal elements of the matrix $\mathbf{m_u}$ are the semi-differences between the prime and the double prime estimates of each one of the fundamental properties. These elements are interpreted as the statistical uncertainties associated by the degree of randomness on each fundamental property because of depolarization.

In summary, the logarithmic decomposition provides an easy way to determine the fundamental polarization properties characterizing a medium, considered as homogenous along the direction of propagation of light over a distance d. If the medium is depolarizing, then the decomposition provides a matrix $\mathbf{m}'$ whose elements are related to the fundamental properties. A simple sum decomposition of matrix $\mathbf{m}'$ allows to obtain an estimation of the most probable values of the fundamental properties together with their related uncertainty created by the depolarization. Moreover, the matrix $\mathbf{m}'$ provide three values allowing to characterize the depolarization affecting the sample unambiguously.

2.4.2.4 Experimental Validation of the Reverse Decomposition

The reverse decomposition procedure has been validated [28] by an *ad hoc* setup schematized in Fig. 2.6, used in conjunction with an imaging Mueller polarimeter described in more detail later. This setup comprised three samples: a depolarizer, a diattenuator and a retarder, traversed by the light beam in this order, and realized as follows:

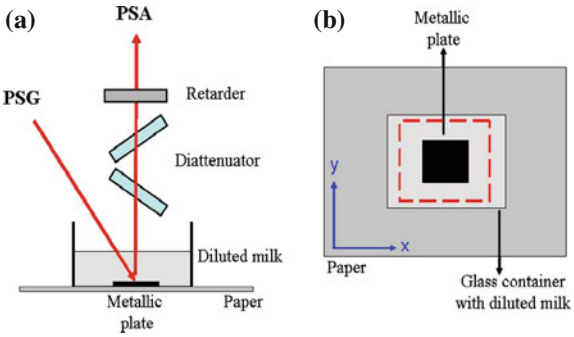

Fig. 2.6 Experimental set-up used in conjunction with an imaging Mueller polarimeter for the experimental validation of the "reverse" decomposition. **a** Side view of the whole setup. **b** View of the depolarizer as seen by the imager, from the *top*. The *red dotted line* on panel **b** defines the field imaged on the CCD

- *The depolarizer*. As a controllable depolarizer we used a transparent glass container, resting on a white piece of paper, with a small square metallic plate at the center of the field of view. This container was filled with milk diluted in water at variable concentrations. The paper always appeared as highly depolarizing due to its bulk scattering properties while the depolarization power of the plate could be varied from 0 to 1 by increasing the milk concentration.
- *The diattenuator*. This element consisted of two high index (n = 1.8) glass plates, tilted as shown on the figure at about 45°, providing a uniform diattenuation D close to 0.3 all over the field of view. This diattenuation was kept constant throughout this investigation. Moreover, both glass plates were tilted around the y axis of the image, implying that in the Mueller matrix of the diattenuator alone the only non vanishing elements were M_{11}, $M_{12} = \mathrm{M}_{21} < \mathrm{M}_{11}$ and $M_{22} = \mathrm{M}_{11}$, as it can be easily checked from (2.26) with $\theta = 0$.
- *The retarder*. The retarder was a commercially available 50 mm clear aperture mica quarter wave-plate (Melles Griot 02WRM009). This element also can be inserted and removed without any displacement of the image of the depolarizer. The orientation of the plate was also kept constant but arbitrary, so that the lower right 3×3 sub-matrix in (2.33) was "full".

Both the diattenuator and the retarder could be inserted or removed from the beam path without any displacement or deformation of the image of the depolarizer. The measurements were performed as follows: the container was filled with 30 ml of water first, and milk concentration was gradually increased, from 0 to 5 %. For each concentration, three Mueller images were taken, the first one with the depolarizer alone, the second one with the depolarizer followed by the diattenuator and the third one with the retarder added to the other two components. Figure 2.7 shows typical experimental Mueller images, taken at 0.6 % milk concentration. Moreover:

- The image taken with the depolarizer alone exhibits the expected shape for a suspension of spherical scatterers, i.e. a diagonal matrix with $\mathrm{M}_{22} = \mathrm{M}_{33}$. As

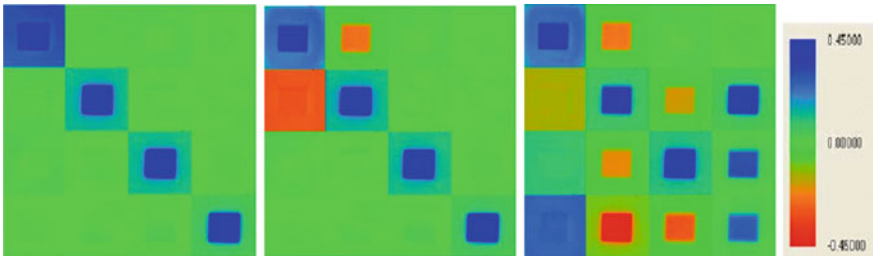

Fig. 2.7 Mueller matrix images taken with 0.6 % of milk concentration on water. *Left* depolarizer alone. *Middle left* depolarizer followed by the diattenuator. *Middle right* depolarizer, diattenuator and retarder. All elements are normalized by $M_{11,}$ the only one shown without normalization and displayed according to the color scale shown at *right* of the figure. Images taken from Ref. [28] with authorization of the publisher

expected, the central part of the image, corresponding to the metal plate, features higher values of the diagonal terms than the more depolarizing surrounding part, corresponding to the paper.

- The second image was taken with the diattenuator after the depolarizer. Again, the measured Mueller images exhibit the expected trends: with respect to the previous image, only the M_{12} and M_{21} are affected. Moreover, the observed diattenuation (M_{12}) is significant only on the metal plate, and practically vanishes in the peripheral part due the strong depolarization characteristic of the paper. In contrast, the polarizance (M_{21}) is uniform, as expected for a diattenuator set after the depolarizer and covering the whole field of view. This result clearly shows how depolarization breaks the expected symmetries for a non-depolarizing Mueller matrix of a diattenuator.
- In the third image, taken with all three elements in place, we see a "mixing" of lower three lines due to the shape of the retarder Mueller matrix M_R given by (2.30). All three the components of the polarizance vector are nonzero, but of course they remain spatially uniform as expected for a polarizance is introduced by the spatially uniform diattenuator.

To assess the performance of the appropriate decomposition (in the present case the "reverse" one) we applied the procedure to various images obtained with the diattenuator and/or the retarder after the depolarizer. The Fig. 2.8 shows the image of the depolarizer extracted by applying both the forward and reverse decompositions to the image acquired with all elements present (right panel of Fig. 2.7). Simple visual inspection of Fig. 2.8 clearly shows the relevance of the reverse decomposition in our case, as this decomposition retrieves a diagonal image quite similar to that taken with the depolarizer alone (left panel of Fig. 2.7). In contrast, the forward decomposition introduces an artificial polarizance, together with significant errors in the diagonal terms (M_{44} appears larger than M_{33} and M_{22}, while the opposite is true, as correctly found by the reverse decomposition).

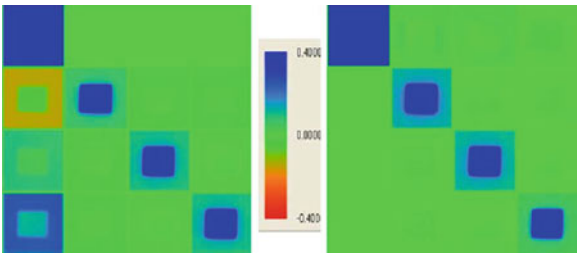

Fig. 2.8 Mueller images of the depolarizer obtained by the forward (*left*) and the reverse (*right*) decomposition of the image taken with all three elements present. Images taken from Ref. [28] with authorization of the publisher

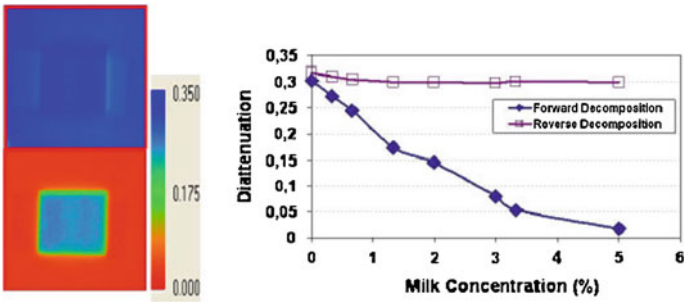

Fig. 2.9 Data relevant to the diattenuator retrieved from images taken with all components present by both forward and reverse decompositions. *Left* scalar diattenuation images provided by the reverse (*top*) and the forward (*bottom*) decompositions at 0.6 % milk concentration. *Right* evolution of the scalar diattenuation retrieved by both decompositions in the central region (where the plate is located) as a function of milk concentration. Images taken from Ref. [28] with authorization of the publisher

Another test was performed on the images of the diattenuator provided by both procedures. The results are summarized in Fig. 2.9. The left panel shows the diattenuation images provided by both procedures from measurements with all elements present. The image at the top, provided by the reverse decomposition, shows an almost spatially uniform diattenuation, as expected. In contrast, the reverse decomposition displays widely different values in the regions with the plate and the paper, with a very large error for the latter, due to its strong depolarization power. The right panel of Fig. 2.9 shows the evolution of the diattenuation retrieved in the region of the plate as a function of milk concentration, or, equivalently, of the depolarizing power δ in this region. When δ is low both decompositions provide a value close to the expected value, 0.3. Then, when δ increases, the value given by the forward decomposition decreases very significantly, while that given by the reverse decomposition remains stable.

2.4.3 Summary

In summary, in this section a number of possible ways to decompose Mueller matrices have been presented. A decomposition is always possible on a given matrix, however each decomposition has its own domain of validity and it will produce correct and results when applied to the cases for which it is adapted. Otherwise it may produce non-sense results. When it comes to decomposing Mueller matrix it is thus advisable to have a good knowledge about the physical nature of the system to evaluate the relevance of the various decompositions. It is also advisable to apply different decompositions to the same Mueller matrix and select the 'correct one' (or, rather, the 'best one') after a critical comparison of all the results. In spite of these *caveats*, Mueller matrix decompositions may prove extremely useful, as we will show for several experimental examples in, Sect. 2.7, the last section of this chapter.

2.5 Standard and Generalized Ellipsometry

Ellipsometry is a well-established and powerful optical tool for the characterization of optical substrates, thin films and multilayer samples. This technique is based on the measurement of the sample Jones matrix, followed by numerical treatments involving direct data inversion in "simple" cases, or, more frequently, data fitting by simulations with a suitable multi-parameter model.

Depending on whether the sample Mueller matrix is diagonal or not, the technique is called Standard or Generalized Ellipsometry. Non-diagonal Jones matrices are generated because the sample has the ability to transform p polarized light into s polarized light and vice-versa, which is called cross-polarization. Standard ellipsometry is, by far, the most widely used and is perfectly well suited to optically isotropic samples. On the other hand, generalized ellipsometry is needed for thorough characterization of samples such as: magnetized materials with their associated magnetization directed out of the plane of incidence, anisotropic crystals, diffraction gratings in conical configuration or roughened surfaces.

In the rest of this section, we will essentially consider standard ellipsometry, including the basic principles of operation of the most widespread ellipsometers. However, we will show that these instruments, though explicitly designed for standard ellipsometry, can also be used for generalized ellipsometry provided the sample Jones matrix obeys some specific symmetry properties. We postpone to Sect. 2.6 the presentation of Mueller ellipsometers, which are specifically designed to provide the whole set of 16 coefficients (or 15 if the matrix is measured in its normalized form).

2.5.1 Standard Ellipsometry

Standard ellipsometric measurements are commonly performed in external configuration, which means that a light beam propagating in air (or vacuum) is reflected by or transmitted through, a sample, and then it propagates again in air (or vacuum) before arriving at the detector. The interest of ellipsometry is that it can measure simultaneously the moduli and the phases of the polarization components of the light.

The sensitivity of phase measurements, exploited to determine thin film thickness, has its roots in an interferometric effect. The light reflected by the first interface of a layer present in the sample, interferes with the light reflected by the second face of the layer. The same principle remains valid when a stack of multi-layers are present. Therefore, the maximum film thickness that can be measured with ellipsometry has to be less than the coherence length of the light source (otherwise, true depolarization occurs and must be properly taken into account). Accordingly, ellipsometry is capable of characterizing transparent or low absorbing thin films with thicknesses ranging from less than a nanometer to several micrometers.

The information provided by ellipsometry is very rich for layer stack description. It enables accurate measurements of surface roughness and interfaces, while the determination of complex refractive index gives access to fundamental physical parameters which are related to a variety of sample properties including: morphology, crystallinity, chemical composition and electrical conductivity, etc.

The informations extracted from ellipsometric measurements are greatly enhanced by using wide spectral ranges, from vacuum ultraviolet to mid-infrared. The vacuum-ultraviolet, (wavelengths between 130 and 400 nm) is the most sensitive to small changes such as ultra-thin layers or interfaces, films with low index contrast, gradient and anisotropy. Ultraviolet is also highly sensitive to the roughness of sample surface. The near-infrared (NIR), (wavelengths between 0.8 and 3 μm), and mid-infrared (MIR) (wavelengths between 2 and 14–50 μm), are necessary to determine the thickness of materials which are strongly absorbing in the visible spectrum. NIR and MIR are also used to determine the optical conductivity (typically metals and doped oxides) because in this spectral region the optical response of samples is dominated by free charge carriers.

In addition to high sensitivity, ellipsometry has the advantages of being non-destructive and contactless. A spectroscopic ellipsometer is relatively easy to use and requires no sample preparation. Standard ellipsometers can be built with light-weight optomechanical components and they are relatively compact. They can be mounted as stand-alone instruments or coupled to other systems such as vacuum chambers, chemical reactors or bio-reactors, etc. In the former case, measurements are said to be ex-situ and in the latter they are called in-situ. In-situ measurements are interesting because they allow for the characterization of a sample in “real-time” and at the same conditions (no alterations by the atmosphere) as it is prepared, deposited or treated (Fig. 2.10).

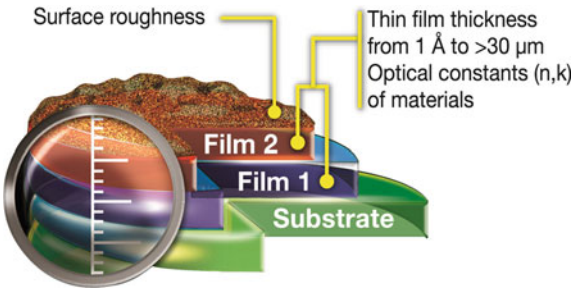

Fig. 2.10 Schematic representation summarizing the different parameters related to the sample that can be deduced using ellipsometry. These parameters include: thin film thickness, refractive index, roughness, porosity, composition and uniformity, etc.

The variety of samples that can be studied with ellipsometry opens a wide range of possibilities for this technique. A recent survey [29] of the most relevant databases of scientific publications concluded that ellipsometry has been successfully applied in many studies concerning material science (semiconductors and photovoltaics), biology (biofilms, and biosensors) and pharmacy.

2.5.2 Analysis of Ellipsometric Data

Conventional techniques used for thin film characterization (e.g., ellipsometry and reflectometry) rely on the fact that the complex reflectivity of an unknown optical interface depends on both its intrinsic characteristics (material properties and thickness of individual layers) and on three properties of the light beam that is used for the measurements: wavelength, angle of incidence, and polarization state. In practice, characterization instruments record reflectivity spectra resulting from the combined influence of these parameters. The extraction of the information concerning the physical parameters of the sample from the recorded spectra is an indirect process, in other words, from a given ensemble of experimental data, we need to build a theoretical model of the sample allowing to reproduce as closely as possible the measured data.

In general, theoretical models depend on a series of parameters characteristic of the sample, which must be adjusted to make the theoretical data "fit" the measurements. A common model for a stack of layers includes the thicknesses and the refractive indices of the layers. In many cases, the refractive index of the substrate must be considered as well [30, 31]. The quality of the fit is usually evaluated with a figure of merit and it is used during the fit process to guide the numerical algorithm which searches for the best-fitted values of the model parameters. According to [30] it is necessary to define an unbiased figure of merit in order to judge for the goodness of fit. There exist different expressions for the figure of merit, but the most popular is the one based on the mean square deviation between simulated and measured data.

$$\chi^2 = \frac{1}{N-M-1}\sum \frac{\left(\Psi^{Th}-\Psi^{Exp}\right)^2}{\sigma_\Psi^2} + \frac{\left(\Delta^{Th}-\Delta^{Exp}\right)^2}{\sigma_\Delta^2} + \frac{\left(R^{Th}-R^{Exp}\right)^2}{\sigma_{R'}^2} \tag{2.59}$$

N refers to the total number of data points and M is the total number of fitted parameters. The superscripts *Th*, and, *Exp*, refer the theoretical and experimental data respectively. The summation is done over all the spectral data points. The sigmas in the denominators correspond to the estimated uncertainties of the corresponding experimental values. Typical values for sigmas of our experimental setups are around 0.5 or 0.1 % depending on the setup. The advantage of the formulation given by (2.59) is that it allows to include non-ellipsometric data, such as total reflectivity R, in the fitting process. Combination of ellipsometric data with information coming from other sources can be interesting and enhances the accuracy in the determination of fitted parameters. According to [30] the figure of merit behaves like a multivariate mathematical function which depends on a given number of fitting parameters.

Once the figure of merit has been defined, it is possible to take advantage of modern computers to automatize the process of parameter fitting, which is based on the search of the minimum value of the figure of merit. The automatic process of minimization of a multivariate function is far from being obvious. The principal difficulty that arises almost systematically, is the fact that the figure of merit may have either multiple minima with the same value, or multiple partial minima with different values. In order to minimize the impact of this drawback in the final results, it is possible to use smart or advanced minimization strategies which are based either on systematic multiple guesses for the initial parameters, or genetic algorithms or even on simulated annealing algorithms. In spite of the advantages of those minimization strategies, it is important to keep in mind that at the end of a minimization process, a supervision of the results is necessary to check their pertinence and efficiency.

A second factor that can complicate data fitting, which is inherent to the fact that ellipsometry data analysis is an indirect process, is the correlation between fitted parameters. We use the term parameter correlation when in a fit process it is possible to find multiple sets of parameters that produce the same value of the figure of merit. Correlation is said to be linear when the couples of correlated parameters follow a linear relation. Correlation between fitting parameters happens because experimental data are not sensitive to individual parameters but to combinations of them. Correlation between two parameters may also occur if one of the two parameters has much more impact on the data, the optical response, than the other. A statistical treatment of optical and simulated data based on the variance-covariance matrix formalism [30] can quantify parameter correlations which are specific to the sample and the model. It is therefore difficult to establish general rules to treat the problem. A procedure based on common sense consists, whenever correlation appears, to keep one of the parameters fixed at a 'reasonable' value, determined a priori or from a complementary technique (microscopy, XPS…), and to fit the other parameters. Modern commercial ellipsometers come with data modelling software packages specially designed to help the user, professionals or beginners, to overcome the most usually encountered difficulties in data analysis. They provide various data fitting procedures

based on multi-start or multi-guess strategies to avoid problems related to multiple relative minima and parameter correlation. In many cases, they also provide graphical user friendly interfaces which are of great help to build models of complex structures.

In spite of the great advantages of ellipsometry, this technique is limited to the analysis of samples which do not depolarize light. As stated previously, depolarization results from incoherent superposition of light beams with different polarization states. In practice, depolarization is commonly encountered when measuring inhomogeneous samples (either in composition of thickness) or very rough surfaces. Depolarization can be caused by the measurement device itself as in the case of monochromators with poor spectral resolution or instruments with high angular acceptance [3]. When depolarization is present it may introduce significant errors into the results provided by ellipsometry and the usual optical models. In such cases it is safer to make measurements with a Mueller polarimeter and use advanced optical models to take into account the sources of incoherent mixing of light which cause depolarization.

2.5.3 Instrumental Implementations of Standard Ellipsometers

Very many designs have been successfully implemented for standard ellipsometers. As an exhaustive review of all these designs is clearly beyond the scope of this chapter, in this subsection we will restrict ourselves to the configurations schematized in Fig. 2.11.

Overall, the instrument is made of two optical arms and a sample-holder in between. The first arm, the entry, is coupled to a source of light, and includes a linear polarizer set at an azimuth P with respect to the p direction in the plane perpendicular to the input beam. The second arm, or exit arm, is used to determine the polarization of the outcoming beam. It comprises a Polarization State Analyser, or PSA, and a detector which may be a single channel device (photodiode, photomultiplier. . .) or a multichannel one (typically a CCD coupled with a spectrometer, or, less frequently, with an imaging system). The PSA typically includes a polarizer and possibly other components. The PSA design actually defines the various types of instruments outlined in this part.

Of course, in all cases the polarization components can be inverted: all the PSAs described in the following can be placed in the input

If the instrument is designed as shown in Fig. 2.11, with only a linear polarizer (set at azimuth P) between the source and the sample, then the incident polarization is linear, with a normalized Stokes vector of the form:

$$\mathbf{S}_{inc}^{T} = \left(1, I_p - I_s, I_{45} - I_{-45}, 0\right) = (1, \cos(2P), \sin(2P), 0) \tag{2.60}$$

As a result, the output Stokes vector $\mathbf{S}_{\text{out}}$ does not depend on the last column of the sample Mueller matrix $\mathbf{M}$: *only the first three columns of* $\mathbf{M}$ *can be determined by such an instrument*. Similarly, if the design is reversed and the *output arm includes*

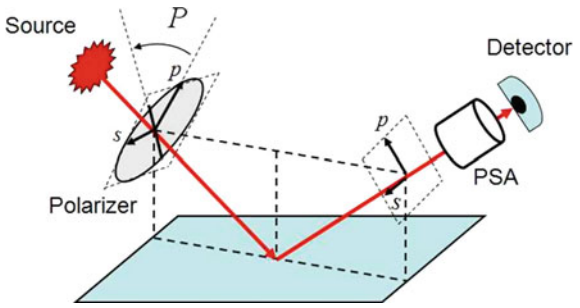

Fig. 2.11 General scheme of a standard ellipsometer. The PSA is the Polarization State Analyzer, which distinguishes the various setups outlined in this subsection

only a linear polarizer before the detector, then only the first three lines of **M** *will be accessible*, as this type of analysis does not provide any information about the circular component V of the Stokes vector $\mathbf{S}_{\text{out}}$ of the emerging beam.

Basically, standard ellipsometers can be classified into two general families, null-ellipsometers and non-null ellipsometers. In null ellipsometers, the optical components of the system must be rotated until the detected intensity vanishes, then the ellipsometric values are deduced from the orientations of the optical elements needed to achieve the null intensity. Conversely, in non-null ellipsometers the light intensity is modulated temporally by the action of at least one of the optical components integrating the ellipsometer, then after an harmonic analysis of the signal, the ellipsometric values are deduced. The non-null ellipsometers can be classified into three groups: rotating polarizers or analyzers, rotating compensators and phase-modulated. In the following we overview some characteristics of the different types of ellipsometers. Our interest is to show which functions of the ellipsometric angles Ψ and Δ can be measured with each type of instrument, and also, how those measurements are related to the Mueller matrix elements. A deeper and more exhaustive analysis of different ellipsometric configurations can be found elsewhere [1, 3, 32].

2.5.3.1 Null Ellipsometers

Null ellipsometers were the first type of instruments developed in late nineteenth century because of their instrumental simplicity and ease of use. As outlined before, the operation of this kind of ellipsometers consists of rotating the optical elements in order to cancel the transmitted intensity. The operation is so simple that in the former systems, rotation was done manually and the null intensity was evaluated with the naked eye. During the twentieth century, thanks to the generalization of electronics, automatic rotation by motors and photodiodes substituted the human hand and eye respectively, making the measurement task much more comfortable. Two possible PSA designs for null ellipsometers are shown in Fig. 2.12.

In the first design (left panel of the figure) a variable retarder (VR) is included just after the sample with its axes parallel to the s and p directions, followed by a linear analyzer. (The VR represented as a Babinet Soleil Bravais compensator, but of course any other equivalent device, such as a nematic liquid crystal cell, may also

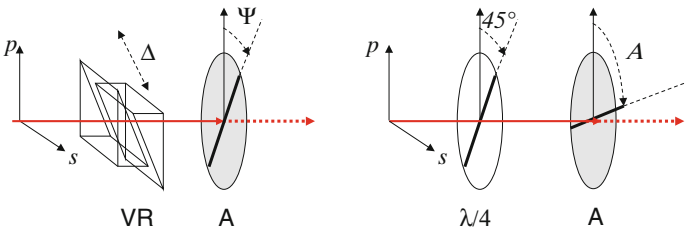

Fig. 2.12 Two possible designs of PSAs for null-ellipsometers. *Left* variable retarder (VR) with its axes aligned along the s and p directions, followed by a linear analyzer (A). *Right* the variable retarder is replaced by a quarter wave plate (λ/4). In both cases, the high transmission axis of the polarizer is shown as a black bar

be used). This PSA requires to set the polarizer in the input arm at $P = 45°$. Then, for the incoming beam $E_p = E_s$, while after the sample one has

$$E_p = E_s \tan \Psi \quad \exp \quad [i\Delta] \tag{2.61}$$

Now, if (and only if) the VR is set at a retardation $-\Delta$, the elliptical polarization described by (2.61) is transformed into a linear one, oriented at an angle Ψ from the s direction. Then extinction is merely obtained by setting the analyzer A at an azimuth Ψ from the p direction. The ellipsometric angles Δ and Ψ are thus nothing else but the retardation introduced by the VR and the azimuth of the analyzer that extinguish the output beam. Once the VR has been properly calibrated, such a setup can be used at various wavelengths.

In the second setup (right panel of Fig. 2.12) the VR is replaced by a quarter wave plate (QWP), which is cheaper and may also be more accurate due to its wider angular and spectral acceptances angle (at least for zero or low order plates), but will operate at a single wavelength. The fast axis of the QWP is oriented 45° with respect to respect to p direction the plane of incidence. The intensity measured by the detector is then:

$$I = \sin(2A)\sin(2\Psi)\left[\sin(2P)\cos(\Delta) - \cos(2P)\sin(\Delta)\right] - \cos(2A)\cos(2\Psi) + 1 \tag{2.62}$$

and vanishes if and only if

$$A = \Psi \quad \text{and} \quad 2P + 90° = \Delta \tag{2.63}$$

meaning that now the ellipsometric angles Ψ and Δ are retrieved from the orientations of the input polarizer P and the output analyzer A.

Null ellipsometers based on QWPs have been shown to be very accurate, and comparable to good modern instruments, but a single wavelength. As mentioned above, to circumvent this limitation VR can be used (in both the configurations shown in Fig. 2.12) to make the instrument spectroscopic, but the overall accuracy may be limited by that of the VR calibration.

2.5.3.2 Rotating Analyzer Ellipsometers

In this case, the PSA consists only of a single linear analyzer, rotating at constant angular speed ω. This configuration is often referred to as "PSRA" for "Polarizer-Sample Rotating Analyzer". The mechanical rotation of the analyzer is used to harmonically modulate the intensity of the light beam, for subsequent synchronous detection. The detected signal by a PSRA ellipsometer can be written as follows:

$$S(t) = S_0 \left[1 + \alpha \cos(2\omega t) + \beta \sin(2\omega t)\right] \tag{2.64}$$

where ω is the angular rotation speed of the analyzer. The Fourier coefficients of the modulated signal can be written as functions of the ellipsometric angles Ψ, Δ and the orientation of the polarizer with respect to the plane of incidence, P:

$$\alpha = \frac{\tan^2\Psi - \tan^2 P}{\tan^2\Psi + \tan^2 P}, \quad \beta = \frac{2\tan\Psi\cos\Delta\ \tan P}{\tan^2\Psi + \tan^2 P} \tag{2.65}$$

from which one easily gets

$$\tan\Psi = \sqrt{\frac{1+\alpha}{1-\alpha}}\,|\tan P| \quad \cos\Delta = \frac{\beta}{\sqrt{1-\alpha^2}} \times \frac{\tan P}{|\tan P|} \tag{2.66}$$

As a result $\tan\Psi$, and thus Ψ itself, is determined unambiguously. In contrast, *as only* $\cos\Delta$ *is actually retrieved*, for this type of instrument:

- Only the absolute value of Δ is measured,
- This value becomes inaccurate when Δ is close to 0 or 180°, where the cosine function reaches its extrema. This situation typically occurs for thick transparent or highly absorbing samples.

However, this shortcoming may be obviated by inserting an additional known retarder, with its axes aligned with the s and p directions, to "shift" the retardation to be measured away from 0° or 180°. Another possible issue to be solved are the systematic errors which may be introduced by any residual polarization of the source and/or of the detector. On the other hand, as the technique uses only polarizers, it is possible to operate it over wide spectral ranges (from 200 nm to 30 μm), and the rotation speed may be chosen according to other requirements, such as a possible acquisition by a linear CCD after a spectrometer, which can be very convenient in many cases.

About Muller matrix elements, as stated above the fourth column cannot be measured with a linear polarization incident on the sample. Moreover, when the Polarization State Analyzer at the output consists also in a simple (rotating) linear analyzer, the fourth row is also inaccessible. Only the upper left 3×3 sub-matrix of the sample Mueller matrix can be determined, provided the measurements and data analysis outlined above are repeated with at least four different azimuths P of the input polarizer.

Alternatively, both the analyzer and the polarizer can be rotated simultaneously, at different angular frequencies, in a "RPSRA" configuration. For example, if these frequencies are set equal to 3ω for the analyzer and ω for the polarizer, then the intensity measured by a detector can be written as follows:

$$4\frac{I}{I_0} = \alpha_0 + \sum_{j=1}^{4} \left(\alpha_{2j} \cos\left(2j\omega t\right) + \beta_{2j} \sin\left(2j\omega t\right)\right) \tag{2.67}$$

where I_0 represents the light source intensity. The 3×3 upper left sub-matrix of the sample can be expressed in terms of the Fourier coefficients appearing in (2.67) as

$$\mathbf{M} = \begin{pmatrix} \alpha_0 & \alpha_2 & \beta_2 & \bullet \\ \alpha_6 & (\alpha_4 + \alpha_8) & (\beta_8 - \beta_4) & \bullet \\ \beta_6 & (\beta_8 + \beta_4) & (\alpha_4 - \alpha_8) & \bullet \\ \bullet & \bullet & \bullet & \bullet \end{pmatrix} \tag{2.68}$$

2.5.3.3 Rotating Compensator Ellipsometers

Rotating compensator ellipsometers include at least one linear retarder, usually called (somewhat improperly) compensator. The linear polarizers at the entry and exit arms are kept still and, as the name indicates, the retarder is continuously rotated in order to temporally modulate the detected signal.

Depending on whether the rotating compensator is placed at the entry or at the exit arm there are two possible configurations known as PRCSA or PSRCA where the meaning of P, S and A is the same as previously RC stands for Rotating Compensator. In the following we will consider the PSRCA configuration, which corresponds to the general scheme of Fig. 2.11, with a Polarization State Analyzer designed as shown in Fig. 2.13.

A major difference between this type of PSA and the previous one, based on a rotating analyzer, is that with a rotating compensator and a fixed linear analyzer it is

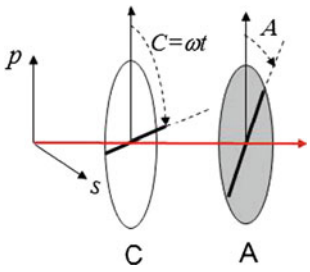

Fig. 2.13 Scheme of the Polarization State Analyzer of a rotating compensator ellipsometer in the PSRCA configuration. The linear analyzer (A) is fixed while the compensator (C) is rotated continuously, with its azimuth $C = \omega t$

possible to retrieve all four components of the Stokes vector $\mathbf{S}_{\text{out}}$, implying that more quantities are measurable, both in standard ellipsometry and for Mueller matrices.

If the compensator is a quarter wave plate (retardation equal to 90°), the intensity recorded by the detector is:

$$\frac{I}{I_0} = 2 - \cos 2\Psi + 2\sin 2\Psi \sin\Delta \sin 2C - \cos 2\Psi \cos 4C + 2\sin 2\Psi \cos\Delta \sin 4C \tag{2.69}$$

where I_0 is again the non-modulated (DC) intensity if the light source, and the trigonometric functions of $C = \omega t$, the compensator orientation. As a result, the three different Fourier harmonics of the modulated signal directly provide the three quantities $\cos 2\Psi$, $\sin 2\Psi \sin\Delta$ and $\sin 2\Psi \cos\Delta$. In other words, rotating compensator ellipsometers provide accurate measurements of the ellipsometric Ψ and Δ angles over the complete measurement range ($\Psi = 0 - 90°$; $\Delta = 0 - 360°$). Similar results can be obtained for PRCSA ellipsometers.

However, the construction of a rotating compensator ellipsometer, with a compensator which behaves ideally providing an achromatic retardance of 90° over a wide spectral range, is a difficult optomechanical challenge, and it requires more complicated calibration and data reduction procedures than rotating polarizer or analyzer ellipsometers. Any deviation of the optical response of the compensator from the ideal behavior must be carefully calibrated, otherwise it will be the source of important systematic errors.

Rotating compensator ellipsometers can be implemented in more general configurations, among which:

(a) *The RP/RCFA configuration*, which consists of a rotating polarizer at the entry arm and a rotating compensator followed by a fixed analyzer at the exit arm.
(b) *The FPRC/RA configuration*, which consists of a fixed polarizer and rotating compensator at the entry arm and at rotating analyzer at the exit arm.

In the best operation mode of the RP/RCFA configuration, the compensator and the polarizer are rotated synchronously at different frequencies. In an optimal operation configuration the rotation frequency of the polarizer is 3 times that of the compensator. Then the detected signal can be decomposed in a Fourier series:

$$4\frac{I}{I_0} = \alpha_0 + \sum_{j=1}^{7} \left(\alpha_{2j}\cos(2jP) + \beta_{2j}\sin(2jP)\right) \tag{2.70}$$

where I_0 is again the light source intensity. The Fourier analysis of the modulated signal provides 15 coefficients which allow to determine the elements of the first three columns of the Mueller matrix as follows:

$$\mathbf{M} = \begin{pmatrix} (\alpha_0 - \alpha_6) & (\alpha_1 - \alpha_5 - \alpha_7) & (\beta_1 - \beta_5 + \beta_7) & \bullet \\ 2\alpha_6 & 2(\alpha_5 + \alpha_7) & 2(\beta_7 - \beta_5) & \bullet \\ 2\beta_6 & 2(\beta_7 + \beta_5) & 2(\alpha_5 - \alpha_7) & \bullet \\ -2\beta_3 & -2\beta_2 & -2\alpha_2 & \bullet \end{pmatrix} \tag{2.71}$$

The Fourier components are functions of the compensator properties, in particular retardation, which can be wavelength dependent. The calibration of such as system is extremely complex, especially when the ellipsometer is spectroscopic [33]. Conversely, the advantage of such as system is that a single measurement scheme allows to obtain 12 out of 16 Mueller matrix elements. If a simplified operation mode is used, in which only the compensator is rotated continuously, the 12 elements of the Mueller cannot be obtained after a single measurement. The polarizer must be placed at different azimuths, and for each position, a new measurement must be made. Once the process is finished, the combination of the Fourier coefficients extracted from all the measurements allows to obtain the first three columns of the Mueller matrix. Similar arguments can be given to illustrate the operation of the FPRC/RA configuration which then provide the first three *rows* of the Mueller matrix.

2.5.3.4 Phase-Modulation Ellipsometers

Finally we describe the phase-modulation ellipsometers, which include a photoelastic modulator, This component can be placed between the linear polarizer and the sample, either at the entry or exit optical arm, in PMSA or the PSMA configurations respectively. Here P, M S and A stand for fixed polarizer, modulator, sample, and fixed analyzer respectively.

A photoelastic modulator consists of a bar of optically isotropic material, which is made birefringent by means of an applied mechanical stress. To enhance this naturally weak effect, the applied stress is periodic and at a proper frequency to generate a stationary sound wave in the bar. The needed time dependent mechanical stress is usually applied using piezoelectric transducers attached to the end of the bar. As acoustic losses in the bar are very weak, very sharp resonances occur for ultrasonic waves, resulting in a dramatic increase of the induced birefringence with respect to a static stress. As a result, the device behaves as a retarder with a time dependent retardation $\delta(t)$, which varies sinusoidally at frequencies of several tens of kHz.

We now consider the PSMA configuration in which at the entry arm the polarizer is fixed and set at an azimuth P with respect to the plane of incidence, while in the exit arm, as represented in Fig. 2.14, the photoelastic modulator is set to an azimuth M and the linear analyzer is set at an azimuth angle A with respect to the plane of incidence. The detected signal then takes the form:

$$S(t) = S_0[1 + I_s \sin(\delta(t)) + I_c \cos(\delta(t))], \tag{2.72}$$

with:

$$I_c = \sin[2(A-M)]\ [\sin 2\mathrm{M}(\cos 2\Psi - \cos 2P) + \sin 2P \cos 2M \sin 2\Psi \cos \Delta] \tag{2.73}$$

$$I_\mathrm{s} = \sin[2(A - M)] \sin 2P \sin 2\Psi \sin \Delta \tag{2.74}$$

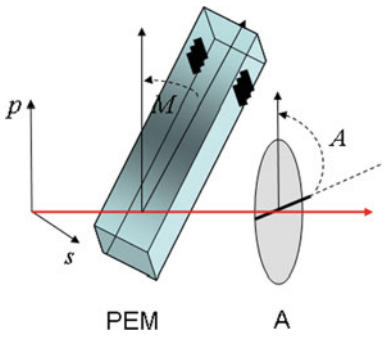

Fig. 2.14 Scheme of a PSA comprising a photoelastic modulator (PEM) and a linear analyzer (A), set respectively at azimuths M and A. The black "patches" in the higher part of the component are piezoelectric transducers

In practice, as $\delta(t) = \sin(\omega t)$, the Eq. (2.72) must be developed in Fourier series (with the well-known Bessel functions as coefficients) to express I_s and I_c as functions of the directly measured quantities, actually the amplitudes of the $\sin(\omega t)$ and $\sin(2\omega t)$ components of the signal.

The expressions (2.73) and (2.74) show that the signal S (I_s, I_c) are maximized when A-M = 45°. Moreover it is also clear that it is not possible to unambiguously determine Ψ and Δ from a single measurement configuration. In practice, two configurations are typically used

- $M = 0°$, $A = 45°$, $P = 45°$, known as configuration II, for which we get $I_s = \sin 2\Psi \sin \Delta$, $I_c = \sin 2\Psi \cos \Delta$
- $M = 45°$, $A = 90°$, $P = 45°$, known as configuration III, for which we get $I_s = \sin 2\Psi \sin \Delta$, $I_c = \cos 2\Psi$

As a result, in configuration II, one measures Δ accurately over the full range (0–360°) but Ψ is ambiguously defined, as only $\sin 2\Psi$ is retrieved. Conversely, in configuration III one fully determines 2Ψ, but only $\cos \Delta$ is obtained. However, all that is needed to shift from one configuration to the other is to rotate the whole PSA, which can be done automatically without major difficulties, and then combine the results of the two measurements for a complete, unambiguous determination of both Ψ and Δ.

For Mueller matrix measurements, the three quantities which can be directly retrieved from the time evolution of the signal can be recast in terms of the matrix elements M_{ij} and the azimuths P, A and M as [34]

$$\begin{aligned} I_\alpha &= S_0 = M_{11} + M_{12}\cos(2A) + M_{13}\sin(2A) \\ I_\beta &= S_0 I_S = (M_{31} + M_{32}\cos(2A) + M_{33}\sin(2A))\cos(2M) \\ &\quad - (M_{21} + M_{22}\cos(2A) + M_{23}\sin(2A))\sin(2M) \\ I_\gamma &= S_0 I_C = M_{41} + M_{42}\cos(2A) + M_{43}\sin(2A) \end{aligned} \tag{2.75}$$

from which it is clear that the nine elements M_{1i}, M_{2i} and M_{4i} can be retrieved with three measurements carried out with $M = 45°$ and $A = 0°$, 60° and 120° for example. Then the last four element M_{3i} can be obtained by another three measurements,

with the same A values as before but $M = 0°$. Moreover, this new set of measurements over-determines the values of M_{1i} and M_{4i}. As a result, six measurements are necessary to retrieve the full set of 12 elements of the first three columns of the Mueller matrix, with partial redundancy. In order to "spread" this redundancy over the whole set of elements, eight measurements can be realized, as described in [34]. Of course, the need to realize so many measurements to obtain the first three columns of the sample Mueller matrix makes phase modulation ellipsometers less practical than those based on rotating compensators, which provide the same set of data with a single measurement.

However, if combined with a suitable synchronous detection (which may be performed digitally) the high modulation frequency (50 kHz) specific of photoelastic phase modulation allows very efficient noise rejection and provides wide dynamic ranges. This technique is thus particularly well suited for very demanding measurements, such as the characterization of extremely thin films of example.

As it can be seen, the elements of the fourth column of the Mueller matrix cannot be addressed. To determine the elements of the sample Mueller matrix, eight measurements are necessary, corresponding to appropriate and alternative settings of the azimuths of the modulator and the analyzer. If the modulator were placed at the exit arm, the 12 elements of the matrix that would be addressed would correspond to the first three rows of the Mueller matrix. The situation is comparable to the rotating compensator ellipsometer previously described. The difference is that with the rotating compensator ellipsometer, the 12 elements can be measured in a single measuring run, whereas 8 runs are needed with an ellipsometer with only one photoelastic modulator.

2.5.3.5 Summary

In this subsection we have presented the most commonly used experimental configurations for standard ellipsometry, with particular emphasis of the quantities that actually can, or cannot, be measured by each of them. In Table 2.1, we summarize the main characteristics of these configurations, including their strengths and weaknesses.

We want to make two points absolutely clear:

- We did not try to review the many refinements are more complex systems which have been tested and developed, possibly up to commercialization. A full book would be needed for this to be done seriously.
- By listing the main advantages and weaknesses of each technique we absolutely do not mean that commercially available systems using this technique necessarily presents these strengths and weaknesses. While some basic limitations, such as those concerning the measurable Mueller matrix elements, cannot be solved in a given configuration, many other practically essential issues, among which those related to the measurements accuracy, the speed, the signal to noise ratio and the

Table 2.1 Summary of essential characteristics, advantages and weaknesses of the main ellipsometric techniques

Technology	Modulation (Hz)	Measured parameters	Strengths	Weakness
Null	0	Ψ and Δ	• Simple optical assemblies	• Spectroscopic extension difficult
		9 Mueller matrix elements	• High accuracy and precision relatively easy to achieve	• Sensitive to residual polarization from source or detector
Rotating polarizer analyser	Several to hundreds	$\tan(\Psi)$ and $\cos(\Delta)$	• Simple optical assemblies	• Inaccurate measurements for Δ approaching 0° or 180°
		9 Mueller matrix elements	• Quasi-achromatic instruments	• Does not measure the V component of the Stokes vector
			• Wide spectral range of operation	• Sensitive to residual polarization from source or detector
			• Easy CCD detection	
Rotating compensator	Several to hundreds	$S_2 = -\cos(2\Psi)$	• Complete measurement of the Stokes vector from a single detection configuration	• Complicated optical assemblies
		$S_3 = \sin(2\Psi)\cos(\Delta)$		
		$S_4 = \sin(2\Psi)\sin(\Delta)$		
		12 Muller matrix elements	• Easy CCD detection	• Rotating may introduces inaccuracies because of beam wandering due to compensator imperfections

(continued)

Table 2.1 (continued)

Technology	Modulation (Hz)	Measured parameters	Strengths	Weakness
			• Generalized ellipsometry possible depolarization + 12 elements of the Mueller matrix	• Complex calibration procedures
Phase-modulation	50×10^3 to 100×10^3	$S_2 = \sin(2\Psi)\cos(\Delta)$; conf. (II)	• No rotating elements and Fast measurements	• Temperature sensitive photoelastic modulator
		$S_3 = \sin(2\Psi)\sin(\Delta)$; confs (II) and (III)	• Excellent signal-to-noise ratio from VUV to NIR	• No "CCD" detection
		$S_4 = \cos(2\Psi)$; conf. (III)	• Accurate measurement of (Ψ, Δ) with two detection configurations (II) and (III)	• Chromatic dependence of the photoelastic-modulator
		12 Mueller matrix elements	• Generalized ellipsometry possible Depolarization + 12 elements of the Mueller matrix	• Measurements of the 12 Mueller matrix elements require multiple (6–8) runs

like greatly depends on engineering developments which are clearly beyond the scope of this contribution

We thus stress that the information presented in Table 2.1 is by no means a "buyer's guide": it might be useful only to ask the manufacturers some reasonably relevant questions !

2.5.4 Generalized Ellipsometry

In practice, when it comes to measure non-diagonal matrices characterizing non-depolarizing cross-polarizing samples, the ease of use, and the adequacy of the instrument to retrieve all the necessary information from the sample is of prime importance for the researcher. Even though none of the previously shown standard ellipsometers (rotating analyzer-polarizer, rotating compensator with a single compensator and phase-modulation with a single modulator) is able to perform a complete measurement of the 16 elements of a Mueller matrix, this does not mean that they cannot be used to perform generalized ellipsometry.

In many cases of practical interest it can be shown [31] that for non-depolarizing systems the form of their associated Jones-Mueller matrix (2.14) is sufficiently redundant that either the corresponding Jones matrix can be inferred from a partially measured Mueller matrix, or the non-measured Mueller-Jones matrices can be inferred from the measured ones. Inference procedure is valid under some hypothesis, for instance, the fact that the off-diagonal element of the Jones matrix J_{sp} is equal to the conjugate of J_{ps}.

At this point it important to point-out that the information carried by a Jones matrix and the related Jones-Mueller matrix is strictly the same, and it can be retrieved independently of the formalism, either Jones or Stokes, used to represent the data and the physical problem to which they are related.

However, it is important to recall that the accuracy of the non-measured matrix elements depends on the systematic errors of the measured matrix elements and also, on the degree of applicability of the conditions under which the non-measured elements have been inferred.

2.6 Mueller Ellipsometry: Instrumental Issues

When the redundancies of the Mueller matrix are not sufficient to reconstruct the full matrix from partial measurements, or when depolarization modifies the structure of the matrix respect to the non-depolarizing case, it is mandatory to measure the 16 elements of the Mueller matrix (15 if it is normalized). In this section we address some essential issues specific of the instruments capable of achieve such measurements.

Fig. 2.15 Schematic representation of the optical setup of a general Mueller ellipsometer. The Stokes formalisms has been used to represent the polarization properties of light. In the framework of Stokes formalism the optical properties of the PSG, sample and PSA can be represented by matrices

2.6.1 General Considerations on Mueller Ellipsometers

Throughout this section, Mueller ellipsometers will be described within the framework of the Stokes-Mueller formalism, which unifies the presentation of both techniques, and simplifies the algebra with respect to original descriptions of generalized ellipsometry based on Jones matrices.

In the following, to avoid too lengthy developments, we will limit our presentation to *sequential* ellipsometers, i.e. systems in which the polarization states are generated in the entry arm and analysed in the exit arm sequentially. The ideas and techniques presented in this section is also valid, with minor adaptations, for instruments performing sinusoidal modulation of the input and/or output polarizations with subsequent Fourier analysis of the signals (Fig. 2.15).

Within this formalism, the operation of any ellipsometric or polarimetric system can be schematized as follows:

The PSG produces a set of input Stokes vectors $\mathbf{S}_i$, which are transformed by the sample into $\mathbf{M}\,\mathbf{S}_i$ ($\mathbf{M}$ being the Mueller matrix of the sample). These output Stokes vectors are then analysed by the PSA, which delivers the raw signals B_{ij} by projecting each vector $\mathbf{M}\,\mathbf{S}_i$ onto its basis states. This scheme can be summarized by the simple matrix equation.

$$\mathbf{B} = \mathbf{A}\,\mathbf{M}\,\mathbf{W} \tag{2.76}$$

where the modulation matrix $\mathbf{W}$, which characterizes the PSG, is formed by the $\mathbf{S}_i$ vectors in columns, while the $\mathbf{S'}_j$ are the line vectors of the analysis matrix $\mathbf{A}$ characterizing the PSA. In the most general case, $\mathbf{B}$ is rectangular, with m lines and n columns, where m and n respectively represent the numbers of states generated by the PSG and analyzed by the PSA.

To get the full Mueller matrix $\mathbf{M}$, both the PSG and the PSA must be "complete", with at least 4 basis states. Then expression (2.76) is sufficient to extract $\mathbf{M}$ from $\mathbf{B}$ by merely inverting the (in principle well known !) matrices $\mathbf{A}$ and $\mathbf{W}$, if both m and n are equal to 4, or by pseudo-inverting these matrices if the system is overdetermined. In the following for simplicity reasons, we will consider only the case of "minimal" Mueller ellipsometers, for which $m = n = 4$, but we emphasize that all the ideas exposed in the following about instrument optimization and calibration can be easily transposed to overdetermined configurations.

While their principle of operation may seem straightforward, Mueller ellipsometers are not so widespread (only two have been very recently made commercially available), because of the added technical complexity due to the simultaneous presence of *complete* PSG *and* PSA. Two issues are of paramount importance (as for any other instruments, but they are particularly critical here)

- The ***optimization of the instrument design***, to get the optimal performance if all components were ideal (perfectly well described by the model). The general criterion for this optimization, namely the minimization of the condition numbers of matrices **A** and **W** is now widely accepted.
- The instrument ***calibration***, in other words the determination of the actual **A** and **W**matrices, which are necessarily affected by the many imperfections of the optical components, positioning systems and the like. *This is a crucial issue*, especially for the complex setups which may be necessary to follow the optimization criterion defined above. Actually, for such complex systems, the usual approach based on a detailed modeling of the whole instrument and its non-idealities may be totally inapplicable. Conversely, the Eigenvalue Calibration Method developed and experimentally validated by Compain [35] circumvents this problem by determining both **A** and **W** matrices from a set of measurements on reference sample directly, by algebraic methods, *without any modeling of the instrument*. Moreover, the *only requirement on reference samples is that they are linear dichroic retarders*; not too close to half-wave plates, as the ECM allows to determine their precise characteristics during the calibration procedure itself. As a result, no very specific samples, such as retardation plates with accurate retardation values, are needed.

Due to its flexibility and robustness, the ECM has been a cornerstone of all the instrumental developments in Mueller ellipsometry at LPICM (and a few other laboratories as well). Its usefulness could hardly be overestimated for the development of innovative Mueller ellipsometers.

2.6.2 Design Optimization of the Polarization State Generators and Analyzers

Item 1 is probably the easiest to address. If we rewrite expression (2.76) as

$$\mathbf{M} = \mathbf{A}^{-1}\mathbf{B}\,\mathbf{W}^{-1} \tag{2.77}$$

we see that the optimization of the instrument design is equivalent to a minimization of the errors in **M** for a given value of the measurement errors in the raw matrix **B**. Due to the algebraic properties of matrices, the error propagation from **B** to **M** will be minimized if the *condition numbers* of **A** and **W** are minimized [36–39]. Without trying to be too rigorous, we now illustrate the rationale behind this criterion by considering the noise propagation from raw intensities to final results in the case of a PSA.

Let us recall that the condition number $c(\mathbf{X})$ any square matrix $\mathbf{X}$ is defined as

$$c(\mathbf{X}) = \|\mathbf{X}\| \; \|\mathbf{X}^{-1}\| \tag{2.78}$$

where the norm of the matrices (and vectors) can be defined in several ways. In our case, the most relevant choice is the Euclidean norm for the vectors while for matrices we define

$$\|\mathbf{X}\| = \sup\left[s_i(\mathbf{X})\right] \tag{2.79}$$

where s_i are the singular values of $\mathbf{X}$. With such definitions, for any vectors $\mathbf{T}$ and $\mathbf{Z}$,

$$\mathbf{Z} = \mathbf{TX} \quad \Rightarrow \quad \|\mathbf{Z}\| \leq \|\mathbf{T}\| \; \|\mathbf{X}\| \tag{2.80}$$

If now we consider the operation of a PSA with an analysis matrix $\mathbf{A}$, the Stokes vector $\mathbf{S}$ of the light impinging on the PSA and the four dimensional vector $\mathbf{I}$ whose components are the four intensities measured at the output of the PSA are related by

$$\mathbf{I} = \mathbf{A}\,\mathbf{S} \quad \Leftrightarrow \quad \mathbf{S} = \mathbf{A}^{-1}\mathbf{I} \tag{2.81}$$

Now when the configuration of the PSA is varied, for example by changing the relative orientations of its optical components, the matrix $\mathbf{A}$ varies too. However, for typical PSA as those described below, the four line vectors of $\mathbf{A}$ are always the transposes of totally polarized Stokes vectors, and it is easy to see that in these conditions that $\|\mathbf{A}\|$ hardly changes. Conversely, $\left\|\mathbf{A}^{-1}\right\|$ may become arbitrarily large when $\mathbf{A}$ becomes close to a singular matrix, for example when two line vectors become almost equal, meaning that the same polarization state is being measured twice while for another polarization state, say $\mathbf{S}_{\min}$ the measured intensity vector $\mathbf{I}_{\min}$ is very small. If so, as the norm of $\mathbf{S}_{\min}$ is always between 1 and 2, $\left\|\mathbf{A}^{-1}\right\|$ has to be large for (2.80) to be verified.

Then, if we make the realistic assumption that any intensity measurement vector $\mathbf{I}$ is affected by an additive noise $\delta\,\mathbf{I}$, then the resulting error $\delta\,\mathbf{S}$ in the extracted $\mathbf{S}$ is simply

$$\delta\mathbf{S} = \mathbf{A}^{-1}\delta\mathbf{I} \tag{2.82}$$

but, in contrast with the signal, *the amplitude* $\|\delta\mathbf{I}\|$ *of the additive noise is assumed to remain constant when the* PSA *configuration is changed. As a result, the maximum error* $\|\delta\mathbf{S}\|$ *on the extracted Stokes vector* $\mathbf{S}$ *is proportional to* $\left\|\mathbf{A}^{-1}\right\|$, *which must then be mimimized. Due to the typically very small variation of* $\|\mathbf{A}\|$, *this criterion is basically equivalent to the minimization of the condition number* $c(\mathbf{A})$, which has the advantage to be dimensionless.

Moreover the condition number $c(\mathbf{X})$ is a widely used criterion to see "how well" a given square matrix $\mathbf{X}$ can be numerically inverted, between the two extremes of unitary ($c = 1$) and singular ($c = 0$). *Actually this parameter describe "how well the polarization space is sampled" by the* PSA. At this point, the generalization to complete Mueller polarimeters is intuitively straightforward: in these instruments,

both the PSG *and the* PSA *must realize an optimal sampling of their respective polarization spaces*.

Mathematically, the argumentation presented above can be easily generalized by recasting the matrices **B** and **M** defined in (2.76) as 16 dimensional vectors $\mathbf{B}^{(16)}$ and $\mathbf{M}^{(16)}$, which transforms (2.76) into [40]

$$\mathbf{B}^{(16)} = \left[\mathbf{W}^T \otimes \mathbf{A}\right] \mathbf{M}^{(16)} \tag{2.83}$$

and using the relationship

$$c\left[\mathbf{W}^T \otimes \mathbf{A}\right] = c(\mathbf{W})c(\mathbf{A}) \tag{2.84}$$

For sequential PSAs the line vectors are actually physically realizable Stokes vectors, which thus exhibit a degree of polarization between 0 and 1. Any set of such 4 vectors can never be orthogonal to each other, which prevents the matrix **A** to be unitary and imposes

$$c(\mathbf{A}) \geq \sqrt{3} \tag{2.85}$$

(a similar limitation actually occurs also for modulation-based ellipsometers, even though the basis states forming the **A** and **W** matrices are not necessarily physically realizable Stokes vectors).

Finally, we point out that the minimization of the condition numbers $c(\mathbf{A})$ and $c(\mathbf{W})$ optimizes the propagation of *additive noise*. In principle, other indicators may be found to minimize the effect of other types of noise, such as the multiplicative noise due to speckle effects in imaging with spatially coherent light.

However, in practice, this criterion provides very efficient guidelines to optimize the design of complete Mueller ellipsometer, as it has been experimentally demonstrated among others, on a double rotating compensator setup operated in discrete rotation steps [41]. In addition to the "Standard" double rotating compensator operated with continuous rotations [42], many optimized designs of complete PSA and PSG have been published in the past decade, based on photoelastic modulator in double pass [43], achromatic division of amplitude prism [44], Pockels cells [45, 46] nematic or ferroelectric. The last two types of PSGs and PSAs will be described in more detail below.

Last but not least, we conclude this subsection with the two following remarks

- Minimizing the conditions numbers of **A** and **W** not only minimizes the noise on the extracted Mueller matrix **M**, but it also "equalizes" the noise among its various components [38], and is thus recommended only for the complete Mueller ellipsometers described in this section. For more specialized instruments, or when particular attention is paid to some particular elements of **M**, other criteria may be much more adapted.

- In principle, the minimization of $c(\mathbf{A})$ and $c(\mathbf{W})$ is intended to minimize the effects of statistical noise on **B**, but in practice it turns out to be also a good criterion to minimize *systematic errors* even though such errors cannot be treated by a general theory comparable to those available for statistical noises.

2.6.3 Actual Implementations of Polarization State Generators and Analyzers

In this subsection we briefly outline various widely used configurations for PSGs and PSAs, without trying to be exhaustive. We first consider those based on what we call "traditional" approaches, which make use of the elements previously described for standard ellipsometers, with, however, suitable modifications to provide full Mueller matrix measurements.

We then focus on the original systems developed at LPICM, and based on

- rotatable Fresnel rhombs for broadband spectroscopic operation in the infrared,
- nematic and ferroelectric liquid crystals. These devices are actually extremely easy to use, and typically feature wide angular and spatial acceptances, which make them particularly well suited for *imaging* applications, in the visible and near infrared range. Spectroscopic Mueller ellipsometers based on these devices have also been successfully developed and commercialized.

For all the optimized PSGs described in the following, the corresponding PSAs are nothing else but the mirror images of the PSGs.

2.6.3.1 Traditional Approaches

Two of the standard ellipsometric configurations, the rotating compensator and the photoelastic modulator have been generalized, at the expense of extensive instrumental and calibration complication, in order to access the full Mueller matrix.

Concerning the rotating analyzer configuration, the generalization consists of using at least two rotating compensators, both with an ideal retardance of 90° and rotating synchronously with different angular speeds [3, 34, 41, 42]. One compensator is placed at the entry arm between the polarizer and the sample, whereas the second compensator is placed at the exit arm between the sample and the analyzer. Following the nomenclature previously described, this configuration can be addressed as PRCSRCA, or in a shortened version just as PCSCA. The advantage of this configuration is that it allows to access the full Mueller matrix in a single measurement run. This approach has been used to develop the commercially available spectroscopic Mueller ellipsometer RC2 by Woollam [47].

The second type of generalized ellipsometer, based on photoelastic modulators, can be found in two variants. The first one, similar to the rotating compensator consists of a system with two modulators. One modulator is placed at the entry arm,

between the polarizer and the sample. The second modulator occupies a symmetric position respect to the first. It is placed at the exit arm between the sample and the analyzer. This configuration can be called, PMSMA. The two modulators can be operated synchronous or asynchronously, but they must be resonant at different frequencies. The drawback of this configuration is that in order to access the whole Mueller matrix, the modulators must be placed at different orientations, and that a complete measurement must be carried out for each orientation [48]. The second variant, consist of a system with four photoelastic modulators. According to the description given in [3, 49], two modulators are placed at the entry arm between the sample and the polarizer, and two modulators are placed at the exit arm between the sample and the analyzer. Again the modulators must vibrate at different frequencies in order to get maximum sensitivity and to avoid possible ambiguities. The advantage is that the four-modulator configuration is exempt of mechanical movements and therefore it can measure the full Mueller matrix in a single run.

2.6.3.2 Rotatable Fresnel Rhombs for Broadband Spectroscopic Operation

As it is well known [4] a prism working in total internal reflection behaves as a retardation plate, with, however, a high degree of achromaticity, as the retardation depends only on the material optical index and the angle of incidence on the face working in internal reflection, without the $1/\lambda$ factor typical of retarders cut in birefringent materials. As a result, if used in conjunction with suitable linear polarizers, this type of component is very appealing to develop broadband PSGs, PSAs, and complete Mueller ellipsometers.

Because of the bulky shape of the prisms, care must be taken to select an appropriate geometry that does not deviate the beam the element is rotated. Among the possible prism geometries [50], we selected the V-shaped retarder shown in Fig. 2.16 as it is the easiest to manufacture. This component consists of two identical Fresnel rhombs disposed symmetrically and joined by optical contact.

The PSG of the Mueller ellipsometer consists then of a linear polarizer, which is kept fixed, followed by an achromatic retarder that can rotate about the light propagation axis. The PSA is identical to the PSG, but with its optical elements in reverse order. During current operation of the Mueller ellipsometer, the PSG generates at least four polarization states corresponding to four different azimuths of the retarder and, similarly, the PSA is operated with at least four analysis configurations.

The optical configuration of the broadband Mueller ellipsometer is very similar to that of a PCSCA generalized ellipsometer, with two fixed polarizers and two mobile retarders, which explains why the broadband Mueller ellipsometer is able to measure a full Mueller matrix in a single run. However, the operation mode and the retardance created by the retarders is quite different. To work in optimal conditions, the retardance of the compensators of a PCSCA generalized ellipsometer must be 90°, 270° or a multiple of them, whereas in the broadband system, it is not the case as it will be shown later. The operation is very different too. The compensators in

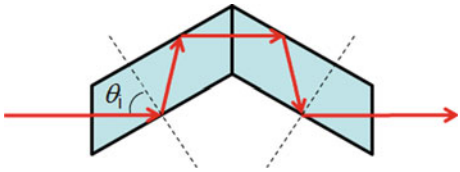

Fig. 2.16 V-shaped achromatic retarder made of two assembled Fresnel rhombs operating with four total internal reflections at incidence θ_i

the PCSCA system are continuously rotated and a double Fourier analysis, either continuous or discrete, of the time-modulated detected signal must be performed. In contrast, our broadband Mueller ellipsometer, is operated sequentially setting each retarder at four predetermined orientations and the signal is measured between two sequential rotations. During an acquisition, the retarders do not move. Simple linear algebraic operations, (two matrix multiplications), are needed to obtain the Mueller matrix from the measured intensities **B**. Finally, the system is calibrated by the ECM method described below.

As described above, the four polarization states generated in the PSG and analyzed by the PSA, have been selected in order to minimize the condition numbers $c(\mathbf{W})$ and $c(\mathbf{A})$. To this end, we simulated the optical behavior of PSG assuming the polarizer and the retarder were ideal. The Mueller matrices of a linear polarizer, **P**, and an ideal retarder, **C**, oriented respectively at azimuths 0 and θ, are:

$$\mathbf{P} = \tau_P \begin{pmatrix} 1 & 1 & 0 & 0 \\ 1 & 1 & 0 & 0 \\ 0 & 0 & 0 & 0 \\ 0 & 0 & 0 & 0 \end{pmatrix};$$

$$\mathbf{C}(\theta, \delta) = \tau_R \begin{pmatrix} 1 & 0 & 0 & 0 \\ 0 & \cos^2(2\theta) + \cos(\delta)\sin^2(2\theta) & \sin^2(\frac{\delta}{2})\sin(4\theta) & -\sin(\delta)\sin(2\theta) \\ 0 & \sin^2(\frac{\delta}{2})\sin(4\theta) & \cos^2(2\theta) + \cos(\delta)\sin^2(2\theta) & \sin(\delta)\cos(2\theta) \\ 0 & \sin(\delta)\sin(2\theta) & -\sin(\delta)\cos(2\theta) & \cos(\delta) \end{pmatrix} \tag{2.86}$$

where τ_P is the polarizer transmission, while τ_R and δ represent the transmission and the retardance of the retarder respectively. Assuming that the light entering the PSG is completely depolarized, the Stokes vector generated by the PSG is given by the expression:

$$\mathbf{S_{out}}(\theta, \delta) = \mathbf{C}(\theta, \delta) \cdot \mathbf{P} \cdot \begin{pmatrix} 1 \\ 0 \\ 0 \\ 0 \end{pmatrix} \tag{2.87}$$

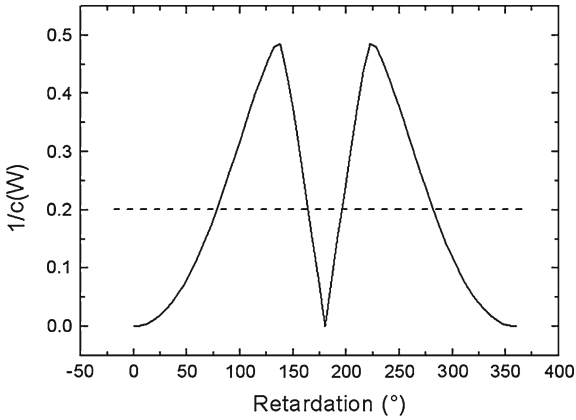

Fig. 2.17 Reciprocal condition number as function of the value of the retardance of the V-shaped prism. The two maxima correspond to the selected retardances

Hence, the matrix **W** and its condition number c(**W**) can be understood as functions of five parameters. Finding the values of the parameters that minimize the condition number is a numerical problem that can be solved by means of a standard numerical optimization routines. As a result, two optimal values for the retardation and two sets of optimal azimuth angles can be found. $\delta_1 = 132° + n360°$ and $\delta_2 = 227° + n360°$, with "n" being any integer. Figure 2.17 shows the values of the condition number calculated as function of the Fresnel rhomb pair retardation for one set of optimal values of the azimuths (In this figures and all the following analogous ones, we plot the reciprocal $1/c$ of the condition number, which may vary from 0 to 0.577 and is thus easier to plot than c.)

The two maxima and correspond respectively to the optimal values for the retardation. The two sets of azimuths are:

- $\{\theta_1, \theta_2, \theta_3, \theta_4\} = \{38° + n360°, 74° + n360°, 106° + n360°, 142° + n360°\}$
- $\{\theta_1, \theta_2, \theta_3, \theta_4\} = \{218° + n360°, 254° + n360°, 286° + n360°, 322° + n360°\}$

with "n" being any integer.

2.6.3.3 Nematic Liquid Crystals

These devices behave as electrically controllable variable retarders, analogous to Babinet Soleil Bravais compensators, with fixed orientation of their slow and fast axes and retardations which may be adjusted from $1 \sim 2$ times 360° to almost 0° by applying a.c. driving voltages, typically in square wave form, with rms values from 0 to about 15 V. We used NLC variable retarders from Meadowlark; detailed information about these devices is available on their site [51]. One limitation of NLCs is their slow switching times, of the order of tens of milliseconds.

The whole PSG is composed of a linear polarizer followed by two NLCs with their fast axes set at the (fixed) azimuths θ_1 and θ_2 with respect to the polarization defined by the polarizer. Calling respectively δ_1 and δ_1 the retardations of the NLCs, a straightforward calculation provides the output Stokes vector

$$\mathbf{S}_{PSG} = \mathbf{M}_R(\theta_2, \delta_2)\mathbf{M}_R(\theta_1, \delta_1) \begin{bmatrix} 1 \\ 1 \\ 0 \\ 0 \end{bmatrix} \tag{2.88}$$

where the matrices $\mathbf{M}_\mathrm{R}(\theta_\mathrm{i}, \delta_\mathrm{i})$ are those defined in (2.33) for linear retarders. Finally we get the explicitly

$$\mathbf{S}_{PSG} = \begin{pmatrix} 1 \\ \left(\mathrm{c}_1^2 + \mathrm{s}_1^2 \cos\delta_1\right)\left(\mathrm{c}_2^2 + \mathrm{s}_2^2 \cos\delta_2\right) + c_1c_2s_1s_2\,(1-\cos\delta_1)\,(1-\cos\delta_2) - s_1s_2 \sin\delta_1 \sin\delta_2 \\ c_2s_2\,(1-\cos\delta_2)\left(\mathrm{c}_1^2 + \mathrm{s}_1^2 \cos\delta_1\right) + c_1s_1\,(1-\cos\delta_1)\left(\mathrm{c}_2^2 + \mathrm{s}_2^2 \cos\delta_2\right) + s_1c_2 \sin\delta_1 \sin\delta_2 \\ s_2 \sin\delta_2\left(\mathrm{c}_1^2 + \mathrm{s}_1^2 \cos\delta_1\right) - c_1s_1c_2 \sin\delta_2\left(\mathrm{c}_1^2 + \mathrm{s}_1^2 \cos\delta_1\right)(1-\cos\delta_1) + s_1 \sin\delta_1 \cos\delta_2 \end{pmatrix} \tag{2.89}$$

where $c_i = \cos 2\,\theta_i$, $s_i = \sin 2\,\theta_i$. Now to generate the needed four Stokes vectors to be complete, we can play with 10 parameters (the fixed azimuths and the four pairs of retardations); which are far too many! Actually, among the many possibilities, the theoretical minimum of $c(\mathbf{W})$ is reached for azimuth values given by

$$\theta_1 = \varepsilon 27.4^\circ + q90^\circ \quad \text{and} \quad \theta_2 = \varepsilon 72.4^\circ + r90^\circ \tag{2.90}$$

where $\varepsilon = \pm 1$ has the same value in both equations, while q and r, are any integer numbers (not necessary equal), and retardation sequences the form

$$(\delta_1, \delta_2) = (\Delta_1, \Delta_1), (\Delta_2, \Delta_1), (\Delta_1, \Delta_2), \quad \text{and} \quad (\Delta_2, \Delta_2), \tag{2.91}$$

with

$$\Delta_1 = 315^\circ + p90^\circ \quad \text{and} \quad \Delta_2 = 135^\circ + p90^\circ \tag{2.92}$$

where, again, p is an arbitrary integer.

As retardations can be adjusted on demand, PSGs based on nematic liquid crystals can in priniciple reach the theoretical minimum of $c(\mathbf{W})$ for any wavelength within their spectral range. This possibility of complete optimization make them very well suited for Mueller ellipsometric measurements discrete wavelengths, provided total acquisition times of the order of 1 s for the whole set of 16 images is acceptable.

2.6.3.4 Ferroelectric Liquid Crystals

With respect to nematics, ferroelectric liquid crystals (FLCs) feature the following quite different, and complementary, characteristics

- They are also linear retarders, but with constant retardation. What is driven electrically is the orientation of their fast axis. This *orientation is actually bistable*, with two possible azimuths 45° apart from each other. The polarity of the DC driving voltage actuelly defines which of these two azimuths is actually reached.
- These devices may switch from one state to other *extremely fast*, typically in less than 100 μs.

The commutation speed of these components allow fast Mueller ellipsometry, either in spectroscopic or in imaging modes. However, due to the fixed values of retardations, PSG is built with these components will not allow a fine minimization of the condition number like that possible with nematics. This minimization can be performed only as a compromise over all the spectral range of interest. On the other hand, if acceptable values are obtained throughout this range, with c values typically less than 4 or so, then the data can be taken simultaneously over this range, allowing fast spectral ellipsometry and/or "color" Mueller imaging.

We first consider a configuration similar to that described above for nematic LCs (Fig. 2.18). A linear polarizer is followed by two FLCs, which are switched alternatively to actually generate the four needed polarization states. If we now call θ_1 and θ_2 two possible azimuths of the FLCs, when the driving voltages are switched, the resulting pairs of azimuth are

$$\{(\theta_1, \theta_2), (\theta_1 + 45°, \theta_2), (\theta_1, \theta_2 + 45°), (\theta_1 + 45, \theta_2 + 45°)\} \tag{2.93}$$

Again, the four generated Stokes vectors can be calculated by putting these azimuths, and the constant retardations δ_1 and δ_2 into (2.89). With this configuration, the best result was obtained with

$$\delta_1 = 90° \quad \text{and} \quad \delta_2 = 180° (\text{at } 510\,\text{nm}), \quad \text{and} \quad \theta_1 = 70°, \theta_2 = 165.5° \tag{2.94}$$

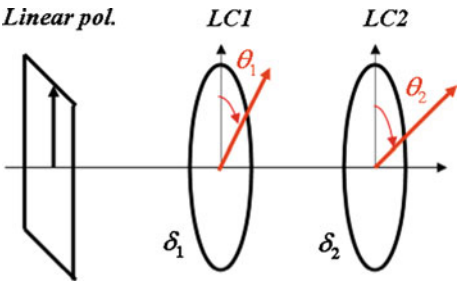

Fig. 2.18 Configuration of a PSG based on two nematic liquid crystals. The *red arrows* indicate the directions of the fast axes

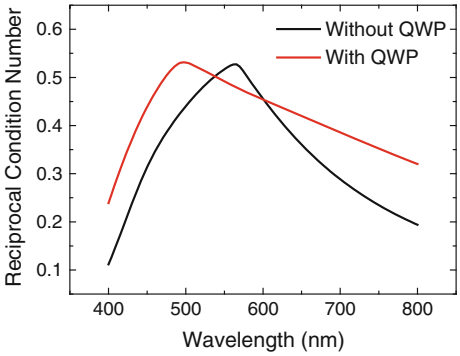

Fig. 2.19 Spectral dependence of the reciprocal condition number $1/c(\mathbf{W})$ of the matrix $\mathbf{W}$ associated to the FLC based PSG. The effect of the insertion of a quartz wave-plate between the FLCs can be clearly seen. *Red line* with the wave-plate and *Black line* without it

The spectral dependence of the reciprocal condition number $1/c(\mathrm{W})$ obtained with these parameters is shown as the black line on Fig. 2.19. The qualitative criterion defined above, namely $1/c \geq 0.25$ is obeyed in a relatively narrow range, between 450 and 700 nm.

This useful spectral range can be significantly extended by adding a true zero order quarter wave plate for 633 nm. With the same values of δ_1 δ_2 (quarter_ and half-wave at 510 nm) the red curve is obtained for

$$\theta_1 = -10^\circ \quad \text{and} \quad \theta_2 = 165.5^\circ \tag{2.95}$$

meaning that the PSG can be used with the same noise propagation as before between 420 nm (limited by the transmission of the FLCs) and 1000 nm.

This configuration has been generalized to extend the spectral range towards the near infrared (NIR). Ladstein and co-workers [52] used the same configuration described above but with FLCs specially adapted to work in the NIR. The working principle of this system was based in a simple scale law. They used two FLCs providing a retardance which was roughly the double of the retardance provided by the ellipsometer working in the visible range, and as a result, they obtained a system which worked well in the range from 700 to 1900 nm. However, the high retardance provided by the NIR FLCs prevented the system to work in the visible range. A second attempt made in parallel by the group of Letnes [53] in Norway and us in France [54] showed that the addition of a third FLC to the PSG (and to the PSA as well) allowed to work in an extended range from 450 nm in the visible to 1800 nm in the NIR. There are two possible modes of operation of the 3FLC system:

(a) In a first mode, the orientations of the three FLCs in the PSG have to be commuted to generate a sequence of 8 polarization states. The same sequence must to be done for the PSA for acquiring a sequence of 64 measurements at each wavelength to extract the Mueller matrix of the sample. This mode is referred as "complete mode".
(b) In a second mode, the orientations of the three FLCs in the PSG have to be commuted to generate a reduced sequence of only 6 polarization states. The

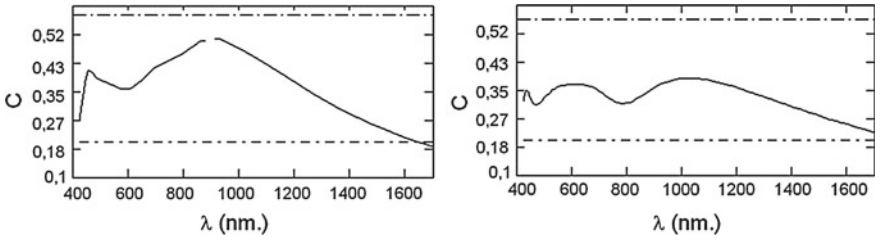

Fig. 2.20 Spectral values of (1/*c*) associated to the 3 FLCs PSG operated in the complete (*left*) mode and the reduced (*right*) mode respectively. λ represents the wavelength in nanometers

same sequence must to be done for the PSA for acquiring a sequence of N = 36 measurements at each wavelength to extract the Mueller matrix. This mode is referred to below in the present document as "reduced mode".

Figure 2.20 shows the spectral value of the reciprocal condition number for the complete and the reduced modes of operation respectively. As it can be seen in both cases, the condition number remains acceptable. The reduced mode, despite of displaying a condition number that is slightly lower than the complete mode, allows to perform a complete Mueller matrix measurement, twice faster than the complete mode because it needs half of polarization station states. The choice between operation modes depends on the particular experimental conditions. Complete mode will always produce less noisy results than the reduced mode, therefore it is recommended to use it when measuring samples with low reflectivity.

2.6.4 The Eigenvalue Calibration Method (ECM)

We now focus on item 2, i.e. the crucial issue of instrument ***calibration***. Obviously, the more complex the instrument, the more difficult the detailed modeling of all its imperfections. This modeling, however, is needed to calibrate the instrument by the usual procedure: the presumably relevant parameters are included in the model describing non-idealities, and then their values are determined by fitting the measured deviations from expected values on well-known samples (in many cases, vacuum or NIST samples made of crystalline silicon covered with various thicknesses of SiO_2) [33, 48]. While this classical procedure may be of great value as it provides in-depth knowledge of the instrument, it can be extremely time-consuming and may not be applicable to otherwise interesting optical assemblies, due to their complexity. In this respect, the optimization of **A** and **W** condition numbers, if it may enhance the instrument performance, may also render its calibration by traditional methods more difficult.

As it was outlined at the beginning of Sect. 2.6, the purpose of ECM method is to accurately determine the **W** and **A** matrices without any modeling of the instrument

nor any specific calibration samples. Provided these samples are linear dichroic retarders, their characteristics (transmission, diattenuation, retardation) are retrieved by the procedure itself, as shown in this subsection. Of course, in the following we expose the ideas presented in the original article by Compain et al. [35] but the practical implementation, and in particular the choice of the reference samples, is somewhat different.

We first address the case of a Mueller ellipsometer operated in transmission, before generalizing the method to the case of measurements in reflection.

2.6.4.1 Calibration of Mueller Ellipsometers in Transmission

The general principle. Let us first assume we have a set of reference samples, characterized by perfectly well known Mueller matrices $\mathbf{M}_i$. As the instrument is operated in transmission, it is possible to make a first measurement on vacuum, to obtain

$$\mathbf{B}_0 = \mathbf{A}\,\mathbf{W}. \tag{2.96}$$

Then, putting the sample i in the beam we measure the corresponding raw matrix

$$\mathbf{B_i} = \mathbf{A}\,\mathbf{M_i}\,\mathbf{W} \tag{2.97}$$

Now, with the experimentally available matrices $\mathbf{B}_0$ and $\mathbf{B}_i$ we calculate the matrices $\mathbf{C}_i$ as

$$\mathbf{C_i} = (\mathbf{B}_0)^{-1}\,\mathbf{B_i} = \mathbf{W}^{-1}\,\mathbf{M_i}\,\mathbf{W}. \tag{2.98}$$

Then, by multiplying both sides of the above equation by $\mathbf{W}^{-1}$ we finally get

$$\mathbf{M_i}\,\mathbf{W} - \mathbf{W}\,\mathbf{C_i} = \mathbf{0}. \tag{2.99}$$

For all values of I (i.e. for all samples). As $\mathbf{M}_i$ is assumed to be known and $\mathbf{C}_i$ has been obtained experimentally, (2.99) is actually a linear system of equations whose unknowns are the elements of $\mathbf{M}$. The question is therefore: how can we solve this system most efficiently? To define the best procedure, we must keep in mind two essential points

- The system may be undetermined, well determined or overdetermined, depending on how many samples have been measured, and "how different" these samples were. Thus the solving procedure must be suitable for all cases.
- Even if the $\mathbf{M}_i$ matrices are perfectly well known, the matrices $\mathbf{C}_i$ are certainly affected by experimental errors, and thus the system may very well have no *exact* solution. All we can try to do is to determine the best possible approximation of the ideal solution which would have required "perfect" measurements for $\mathbf{C}_i$.

The best way to cope with these two issues is to solve (2.99) in the "least-squares" sense, by determining the $\mathbf{X}$ matrix (or matrices, if the system is undetermined) which minimizes the sum of the squares of the $16\,N$ elements of the N 4×4 matrices appearing in (2.99). Of course, is the system turns out to be undetermined, then more samples have to be included. On the other hand, inclusion of new measurements is straightforward.

To practically realize this rms minimization, we define for each measurement the linear operator $\mathbf{T_i}$ which associates to any matrix $\mathbf{X}$ the matrix

$$\mathbf{T_i}\ (\mathbf{X}) = \mathbf{M_i}\ \mathbf{X} - \mathbf{X}\ \mathbf{C_i} \tag{2.100}$$

Provided its elements are properly renumbered any 4×4 real matrix $\mathbf{X}$ can be considered as a vector $\mathbf{X}_k^{(16)}$ with 16 components. Equation (2.100) can then be rewritten in the form

$$(\mathbf{T}_i(\mathbf{X}))_k^{(16)} = \mathbf{Y}_{i,k}^{(16)} = \sum_m \mathbf{H}_{i,km}^{(16,16)} \mathbf{X}_m^{(16)} \tag{2.101}$$

where the $\mathbf{H}^{(16,16)}$ matrix is obtained by a little bit lengthy but straightforward calculation by expliciting the renumbering of the elements of $\mathbf{X}$ and $\mathbf{T}_\mathrm{i}(\mathbf{X})$. Then the sum of the squares of the 16 matrix elements appearing in (2.100) for the sample i can be rewritten as

$$\left|\mathbf{Y}_i^{(16)}\right|^2 = \left[\mathbf{X}_i^{(16)}\right]^T \left[\mathbf{H}_i^{(16,16)}\right]^T \mathbf{H}_i^{(16,16)}\ \mathbf{X}_i^{(16)} = \left[\mathbf{X}^{(16)}\right]^T \mathbf{K}_i\ \mathbf{X}^{(16)} \tag{2.102}$$

where the 16×16 matrix $\mathbf{K_i} = \mathbf{H_i^T}\ \mathbf{H_i}$ is symmetrical and semi-definite positive, i.e. its eigenvalues are all positive or zero. Clearly, if Eq. (2.100) were "exact" (i.e. the matrices $\mathbf{C}_\mathrm{i}$ had no errors) *the* $\ll$ *vector* $\gg$ $\mathbf{W}^{(16)}$ *must be an eigenvector associated with a zero eigenvalue of the* $\mathbf{K}$ *matrix associated with this sample*. If we now define a matrix $\mathbf{K}_{tot}$ as

$$\mathbf{K}_{tot} = \sum_i \mathbf{K}_i \tag{2.103}$$

again $\mathbf{W}^{(16)}$ will be an eigenvector associated with a zero eigenvalue. In fact, the quantity ${}^t\mathbf{X}^{(16)}\mathbf{K}_{tot}\mathbf{X}^{(16)}$ is nothing else but the sum of the squares of the $16\,N$ matrix elements of the $\mathbf{T_i}(\mathbf{X})$ appearing in (2.100) for all samples.

As all the eigenvalues of the $\mathbf{K_i}$ matrices are positive or zero, when the number of samples included in the procedure (and so the number of $\mathbf{K_i}$ matrices in the sum (2.103)) is sufficient, then $\mathbf{K}_{tot}$ will have *only one* eigenvector $\mathbf{W}^{(16)}$ associated with a zero eigenvalue, which then determines the $\mathbf{W}$ matrix unambiguously.

Again, we point out once more than due to the experimental errors affecting the matrices $\mathbf{C}_\mathrm{i}$, none of the eigenvalues of the actual $\mathbf{K}$ matrix is exactly zero. However, if the intensity measurements are reasonably accurate (and if the samples are sufficient

to (over)determine the system) *then one eigenvalue of* **K** *will be found to be much smaller than the 15 others*. In the following, we assume that the eigenvalues of **K** are sorted in decreasing order, from the largest (λ_1) to the smallest (and theoretically vanishing) λ_{16}.

The choice of sets of optimal reference samples. In addition to constitute a very efficient tool to find **W** (if the Mi are known), the above formalism also provides a simple criterion to optimize the choice of the reference samples. Our goal is to determine as precisely as possible the eigenvector of **K** associated with the smallest eigenvalue (λ_{16}). It is reasonable to assume that, the larger the other eigenvalues, the more the eigenvector $\mathbf{W}^{(16)}$ will be "isolated" from the others and thus well determined (or, if the take the argument in the other way around, if λ_{15} is very small, then the two smallest eigenvalues are almost degenerate and $\mathbf{W}^{(16)}$ will be difficult to distinguish from the eigenvector associated to λ_{15}).

In summary, *the best sets of calibration samples are those for which* λ_{15} *is largest, or, equivalently, those for which the ratio* $R = \frac{\lambda_{15}}{\lambda_1}$ *is largest*. As we will see in the following, to be characterized during the calibration procedure, these samples must also linear dichroic retarders set at various azimuths, with Mueller matrices of the form:

$$\mathbf{M}(\tau, \Psi, \Delta, \phi) = \tau \mathbf{R}(-\phi) \begin{pmatrix} 1 & -\cos 2\Psi & 0 & 0 \\ -\cos 2\Psi & 1 & 0 & 0 \\ 0 & 0 & \sin 2\Psi \cos\Delta & \sin 2\Psi \sin\Delta \\ 0 & 0 & -\sin 2\Psi \sin\Delta & \sin 2\Psi \cos\Delta \end{pmatrix} \mathbf{R}(\phi) \tag{2.104}$$

where we recognize a matrix of the form defined in (2.15), while $\mathbf{R}(\phi)$ is matrix describing a rotation by an angle ϕ around the light propagation direction within the Stokes Mueller formalism

$$\mathbf{R}(\phi) = \begin{pmatrix} 1 & 0 & 0 & 0 \\ 0 & \cos(2\phi) & -\sin(2\phi) & 0 \\ 0 & \sin(2\phi) & \cos(2\phi) & 0 \\ 0 & 0 & 0 & 1 \end{pmatrix} \tag{2.105}$$

It turns out that the first condition (only one vanishing eigenvalue) is met with the following set of three measurements (in addition to the measurement of $\mathbf{B}_0$, without any sample):

- *Polarizer set at two different azimuths* ϕ_{P1} and ϕ_{P2}. Actually, ϕ_{P1} *can be set equal to zero throughout*, without any loss of generality,
- *Retarder* with retardation angle Δ, set at an azimuth ϕ_D.

The ratio $R = \frac{\lambda_{15}}{\lambda_1}$ is then optimized by a (little bit lengthy) trial-and-error procedure. A maximum $R_{max} = 0.1015$, which seems to be a *global* maximum, is reached for:

ϕ_{P1}	ϕ_{P2}	Δ	ϕ_D
0°	90°	109°	30.5°

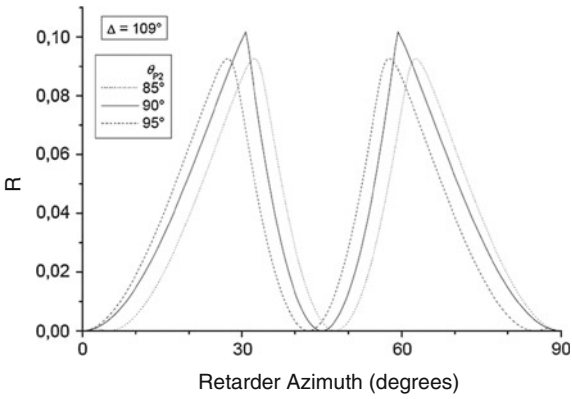

Fig. 2.21 Variation of the ratio R with the retarder azimuth, for three azimuths of the 2nd polarizer

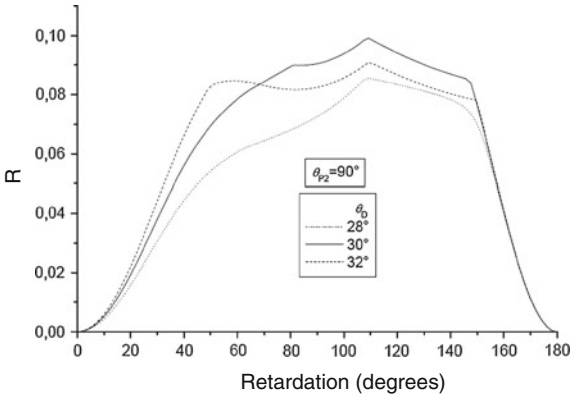

Fig. 2.22 Variation of the ratio R with the retardation Δ of the retarder, for three values of its azimuth

As for the choice of PSG and PSA configuration, this optimization must be completed by an evaluation of the ≪sharpness≫ of this maximum: a calibration procedure characterized by a local maximum $R_{\text{loc}} < R_{\text{max}}$ may be more convenient than that corresponding to R_{max}, if the local maximum is much broader, as the values of the parameters are less critical.

In the three following figures, the ratio, R is plotted against ϕ_{D}, Δ, and ϕ_{P2} respectively for values close to the optimum.

The curves reproduced in Figs. 2.21, 2.22 and 2.23 clearly show that the value of the retardation is by no means critical: this retarder must not be close to a half-wave plate, but basically any value of Δ between 30° and 150° is fine. Conversely, the angular positioning of the polarizer is more critical.

Of course, many other sets of calibration samples can be used, including at least a polarizer and a retarder. For the latter, the acceptable retardation interval is very broad, as seen above.

Characterization of reference samples. The basic idea is to use the very special form of the $\mathbf{M}(\tau_{\text{i}}, \Psi_{\text{i}}, \Delta\text{I}, \phi_{\text{i}})$ matrices of the calibration samples to determine

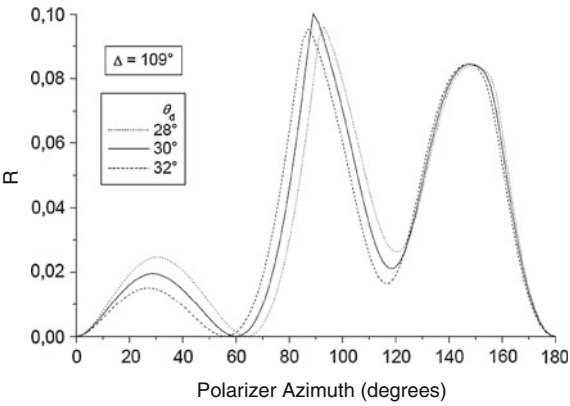

Fig. 2.23 Variation of R with the 2nd polarizer azimuth, for three orientations of the retarder

these matrices during the calibration procedure itself. A key in this respect is that the eigenvalues of these matrices are independent of ϕ. Two of them are real and the other two are complex conjugates:

$$\lambda_{R1} = 2\tau \cos^2 \Psi, \quad \lambda_{R2} = 2\tau \sin^2 \Psi, \quad \lambda_{C\pm -} = \tau \sin(2\Psi)\exp[\pm i\Delta] \tag{2.106}$$

Now, (2.98) shows that the experimentally available matrix $\mathbf{C}_i$ and $\mathbf{M}_i$ have the same eigenvalues, from which we can determine all the parameters of $\mathbf{M}_i$, except the azimuth, by inverting (2.106)

$$\tau = \frac{1}{2}\left(\lambda_{R1} + \lambda_{R2}\right), \quad \cos(2\Psi) = \frac{\lambda_{R1} - \lambda_{R2}}{\lambda_{R1} + \lambda_{R2}} \tag{2.107}$$

$$\sin(2\Psi)\cos\Delta = \frac{\lambda_{C+} + \lambda_{C-}}{\lambda_{R1} + \lambda_{R2}}, \quad \sin(2\Psi)\sin\Delta = -i\frac{\lambda_{C+} + \lambda_{C-}}{\lambda_{R1} + \lambda_{R2}} \tag{2.108}$$

Moreover, these eigenvalues must obey the simple criterion:

$$\frac{\lambda_{R1}\lambda_{R2}}{\lambda_{C+}\lambda_{C-}} = 1 \tag{2.109}$$

which provides a simple test of the quality of the measurements involved in the determination of $\mathbf{C}_i$.

At this point, the azimuths ϕ_i can be determined from the spectrum of the matrix $\mathbf{K}$. If we use a polarizer set at two different azimuths (one of which is zero by definition, and the other, ϕ_{P2}, is close to 90°) and a retarder set at $\phi_D \sim 30°$ the matrix K can be calculated with ϕ_{P2} and ϕ_D "injected" into the $\mathbf{M}_i$ as variable parameters. Then, the system (2.99) has a solution, and l_{16} will tend to zero if, and only if, these parameters take the values corresponding to the actual azimuths of the elements during the measurements. Thus, these azimuths can be determined by minimizing the ratio $\lambda_{16}/\lambda_{15}$. A typical example of such a search is shown in Fig. 2.24. The

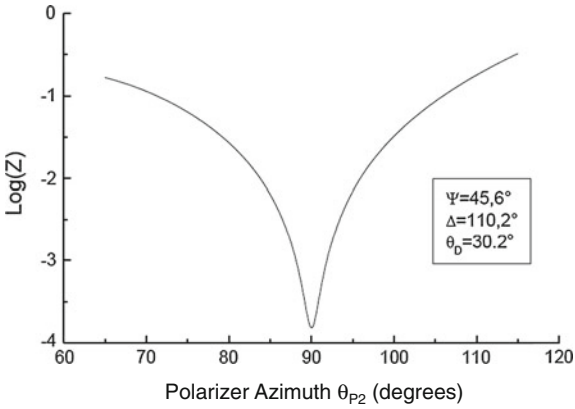

Fig. 2.24 Typical result of the determination of the azimuths of the calibration samples by minimizing $Z = \lambda_{16}/\lambda_{15}$

minimum is quite sharp, allowing a determination of the angles ϕ_{P2} and ϕ_D with accuracies of the order of $0.1°$.

Once **W** has been determined, the matrix A is readily obtained by inverting (2.96):

$$\mathbf{A} = \mathbf{B}_0 \mathbf{W}^{-1} \tag{2.110}$$

2.6.4.2 Calibration of Mueller Ellipsometers in Reflection

We consider now cases where the vacuum cannot be measured, but an object (say a sample holder) with a matrix $\mathbf{M}_0$ (a priori unknown) is necessarily placed between the PSG and the PSA. Then the PSG and the PSA have to be calibrated separately. In a first (common) step, the holder is measured alone, yielding

$$\mathbf{B}_0 = \mathbf{A}\,\mathbf{M_0}\mathbf{W} \tag{2.111}$$

Then the calibration samples are inserted in the input arm, between the PSG and the sample holder. The corresponding raw data matrices now write

$$\mathbf{B}_i = \mathbf{A}\,\mathbf{M_0}\,\mathbf{M_i}\,\mathbf{W} \tag{2.112}$$

From which we calculate the products

$$\mathbf{C}_i = \mathbf{B_0}^{-1}\mathbf{B_i} = \mathbf{W}^{-1}\mathbf{M_i}\mathbf{W} \tag{2.113}$$

And the matrix **W** is then determined in the same way as described previously. Then the calibration elements are inserted in the output arm, between the holder and the PSA, to measure

$$\mathbf{B}'_{\mathbf{i}} = \mathbf{A}\ \mathbf{M_i}\ \mathbf{M_0}\ \mathbf{W} \tag{2.114}$$

And then calculate

$$\mathbf{C}'_{\mathbf{i}} = \mathbf{B}'_{\mathbf{i}}\ \mathbf{B}_{\mathbf{0}}^{-1} = \mathbf{A}^{-1}\ \mathbf{M_i}\ \mathbf{A} \tag{2.115}$$

And the same procedure now provides **A**. There is no need to know $\mathbf{M}_0$ this matrix can even be measured once both **A** and **W**, are calibrated, the only requirement about this matrix is that it should be reasonably well conditioned to allow a safe inversion of $\mathbf{B}_0$.

2.6.4.3 Summary: Practical Implementation

We now summarize how the method is used in practice. The essential steps appear in a different order with respect to the previous (hopefully pedagogical !) presentation:

1. **Choice of the set of calibration samples**. Of course this choice is made once and for all, and may be dictated not only by the criteria shown above, but also by practical considerations about the availability of the components, and the space they need to be inserted. As we already mentioned, there are many possibilities with combinations of polarizers and retarders, the latter being really uncritical. The main issue to keep in mind is that these components should be "ideal" in the sense that they should not depolarize, for example. As a result, these components must feature wide enough spectral, angular or spatial acceptances, depending on the type of instrument.
2. **Measurement of $\mathbf{B}_0$**. This is the first step of the procedure, but if the instrument is operated in transmission (or equivalently, in reflection under normal or quasi-normal incidence) this measurement may also be used for another purpose, namely the minimization of the condition numbers of **A** and **W**, if needed, for example by optimizing the driving voltages of NLCs (this step too is made once and for all for a given configuration): as $\mathbf{B}_0 = \mathbf{AW}$, the lower the condition numbers of **A** and **W**, the lower that of $\mathbf{B}_0$. As a simple measurement of $\mathbf{B}_0$ is much faster than a complete calibration, the multi-parameter optimization using this criterion is also much more efficient, even though at the end a full calibration is needed to evaluate separately $c(\mathbf{A})$ and $c(\mathbf{W})$!
3. **Measurement of the $\mathbf{B_i}$, calculation of the, $\mathbf{C_i}$, matrices and of their eigenvalues**. This step offers very interesting possibilities to check that the system is working properly. Actually, the eigenvalues of the matrices $\mathbf{C_i}$ should be of the form

    a. $(\tau, 0, 0, 0)$ for polarizers,
    b. $(\lambda_{R1}, \lambda_{R2}, \lambda_C, \lambda_C^*)$ for the retarders, and these eigenvalues should verify (2.107)
    c. For any given component, the eigenvalues of its **C** matrix should be invariant when the component is rotated (even though the **B** matrix changes wildly !)

Let us emphasize that these criteria are pretty robust, as they do not involve in any way the (still unknown **A** and **W** matrices) but are based on two conditions which are mandatory for a good operation of the instrument:

- the intensity measurements are linear.
- the components, in their current use, can be considered as "good" linear dichroic retarders.

It is a very strong point of the method to offer the possibility to check these issues in a very robust way.

4. **The K matrix is evaluated** as a function of the unknown azimuths of $(n - 1)$ calibration samples (in the example showed above, these parameters were θ_{P2} and θ_D) and the ratio $Z = \lambda_{16}/\lambda_{15}$ must be minimized to determine the actual values of these parameters,
5. **W is determined** as the eigenvector associated to λ_{16}.
6. **A is determined** either from W and B0 (in transmission) or by repeating the procedure with the calibration samples in the exit arm.

Though this procedure may seem quite complex, once it is implemented it is very easy to use and provides accurate results even for systems which would be impossible to model correctly such as the ellipsometer based on FLCs described in Sect. 2.6.3.2. As a matter of fact, by using this calibration method, *full Mueller ellipsometry becomes easier to implement than more limited techniques with traditional calibration procedures* !

2.6.5 Examples of Complete Mueller Ellipsometers Developed at LPICM

2.6.5.1 Broad Band Spectroscopic Mueller Ellipsometer with Fresnel Rhombs

The motivation to develop a broadband Mueller ellipsometer was to perform complete Mueller matrix measurements in a wide spectral range. Two examples of interesting wide spectral ranges are the vacuum-ultraviolet (130 nm) to the mid infrared (7000 nm), or the visible to mid-long infrared (500–18000 nm). Vacuum-ultraviolet and infrared ranges have particular advantages. Infrared, features enhanced sensitivity to the sample chemical compositions due to molecular vibrations and phonon absorptions. Moreover, free carrier absorption in the infrared can be useful to study the dopant concentrations or electrical mobilities. On the other hand, the shortness of the vacuum-ultraviolet wavelengths make this range ideal to measure the thickness of very thin films (down to a few nm). In addition, the enhanced sensitivity of vacuum-ultraviolet to small defects and structures in the surface of samples is used for optical metrology and surface state quality control.

To date, several systems have been shown which are able to work in the vacuum ultraviolet [55–57], the infrared [33, 58–63], or even the terahertz [64–66] spectral

ranges. However, almost none of them can perform complete Mueller matrix measurements in a wide spectral range because they are either standard (incomplete) ellipsometers, or they are designed to work in a relative narrow spectral range. We developed a broadband Mueller ellipsometer to fill this lack of full polarimetric solutions.

Two main parameters actually determine the performances of a broadband system, namely the transparency and the dispersion properties of the optical components used to build it. Polarizers, based either on prisms or grids, can be used over broad spectral range, with quasi-achromatic properties. For instance, magnesium fluoride (MgF_2) used in prism polarizers is transparent from 0.12 to 7 μm and ZnSe, used for grid polarizers, transmits from 0.6 to 21 μm.

In contrast, issues appear with retarder. Liquid crystals are limited to a relative narrow spectral band covering the visible and the near infrared. These materials strongly absorb in the mid-infrared and may be irreversibly damaged by ultraviolet light. Moreover, liquid crystals show a strong dispersion of retardance at short wavelengths. Similar issues related with either absorption or dispersion appear when other optical components such Kerr optical rotators, photoelastic modulators, or wave-plate compensators are considered. We decided to use retardation induced by total internal reflection in prisms because it is almost non dispersive [67]. Limitations are only induced by the transmission of the prisms.

In accordance to these general principles we developed a prototype which is optimized to work in the mid-infrared spectral range, from 2 to 14 μm. A functional scheme of the prototype optical assembly is represented in the Fig. 2.25a. The instrument is represented in a reflection configuration even though measurements in transmission are also possible. The Mueller ellipsometer consists of an input arm, a sample holder, an exit arm and an acquisition system. The input arm includes a light source, a PSG and a retractable sample-holder for calibration samples. The exit arm includes a second retractable sample-holder for calibration samples, a PSA and a detection platform which can contain one or multiple detectors. The illumination source consists of a commercial conventional FTIR interferometer providing an collimated beam. The PSG is of the type described in Sect. 2.6.3.2, with a fixed grid type linear polarizer, and an V-shaped achromatic retarder. The retarder is mounted on a motorized rotating platform that allows it to be rotated at four consecutive orientations following a predetermined sequence. Both the polarizer and the V-shaped retarder are made on ZnSe. The PSA is identical to the PSG as discussed above.

As shown in Fig. 2.25 it is possible to design the optical assembly either to minimize either the spot size or the divergence of the beam arriving to the sample. In the focused configuration (Fig. 2.25c), the spot size can be reduced to around 300 μm. This configuration is ideal to measure small or inhomogeneous samples. If a motorized X–Y table is used to move the sample, it is possible to record mappings of the sample with a good lateral resolution. In the collimated beam configuration (Fig. 2.25b), the divergence of the beam can be reduced to values of the order of several milliradians. This configuration is ideal for measuring strongly anisotropic samples such diffraction gratings or photonic structures. In this configuration, the spot size is about 0.7 mm. In this configuration, it is advisable to use an automatic

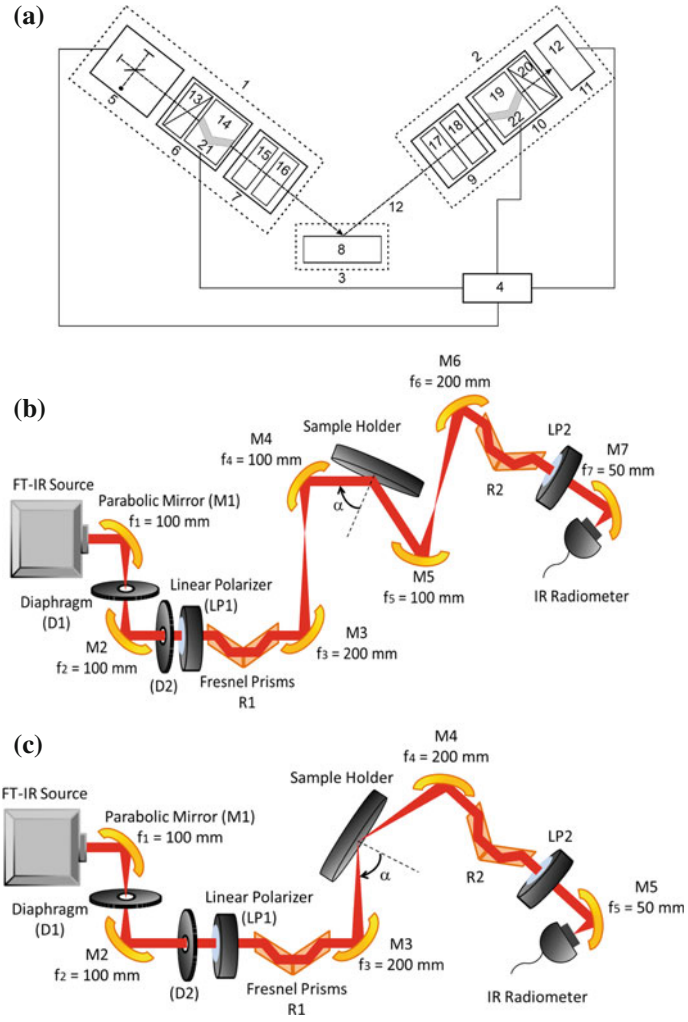

Fig. 2.25 **a** Functional schema of the Mueller ellipsometer. It includes a FTIR interferometer (5) a PSG (6) and a PSA (10). The PSG includes a linear polarizer (13) and the V-shaped retarder (21). The same elements can be found in the PSA. The detection signal (12) and the motors which control the orientation of the V-shaped retarders are controlled with a computer (4). **b** Schematic representation of the optical chain to create a collimated beam incident on the sample. **c** Idem to create a focused spot size on the sample

theta table as sample-holder to make measurements as a function of the azimuthal angle.

2.6.5.2 Spectroscopic Mueller Ellipsometer with Ferroelectric Liquid Crystals

Liquid crystal modulation Mueller ellipsometers use liquid crystal variable retarders to modulate the polarization without any mechanical rotation. The first prototype was built in 2003 and presented to the 3rd International Conference of Spectroscopic Ellipsometry held in Vienna [68]. After the encouraging preliminary results, the system was patented [69], and the first commercial system appeared in 2005 under the name of MM16. Since then, the product has been developed and new versions are now in the market. For instance, a particular implementation adapted to the measurement of small samples, commercialized under the name of AutoSE has been launched in 2008. The latest version, called SmartSE, combine spectroscopic with imaging capabilities. The spectral range, initially limited to the visible (450–850 nm), has been widened to the near IR (450–1000 nm). The working spectral range of liquid crystal based polarimeters is determined by the transparency of the liquid crystal devices. In the short wavelength range, UV radiation must be avoided because it may induce chemical modifications or even destroy the liquid crystals which are made of delicate organic molecules [70]. In the long wavelength range, the near infrared, the limits are due to the thin conducting oxides that are deposited on the windows of the liquid crystal devices that allow the electrical control the orientation of the liquid crystals. The conducting oxides have a high concentration of free charge carriers which absorbs very efficiently the near infrared (>1500 nm) making the devices to become opaque. This range matches quite well that defined in Sect. 2.6.3.4 from the criterion $c(\mathbf{W})$, $c(\mathbf{A}) > 4$, and is also very well suited for the use of standard CCDs.

The optomechanical design of the instrument is shown in Fig. 2.26. The illumination beam comes from a halogen lamp, goes through the PSG, interacts with the sample and traverses the PSA before entering a spectrometer operating in the visible and fitted with a CCD array. For practical purposes, the PSG and the PSA were mounted on an automatic goniometer allowing to vary the angles of incidence and detection from 40° to 90° in steps of 0.01, and to operate the ellipsometer in

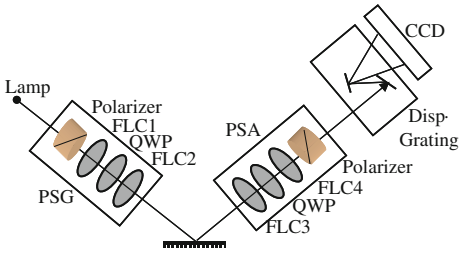

Fig. 2.26 *Left* schematic representation of the general set-up of a Mueller ellipsometer mounted in reflection configuration, showing the PSG the sample and the PSA. *Right* schema of the optical configuration of the PSG. The PSA is identical to the PSG. Pictures taken from [68] with the authorization of the authors and the publisher

reflection and in transmission modes. The sample holder was mounted on an automated theta table which allows rotation of the sample about a vertical axis. As shown below, this azimuthal movement is interesting to characterize anisotropic samples and diffracting structures.

With this setup, full Mueller spectra in the whole spectral range could be taken in seconds or less, depending on the sample reflectivity. Moreover, most users are essentially interested in classical ellipsometry, for which the accuracy must be comparable to that of other, very mature, instruments. Actually, normalized Mueller matrix spectra are retrieved with typical accuracies of a few 10^{-3} % a clear demonstration of the efficiency of the optimization and calibration procedures described earlier.

2.6.5.3 Imaging Mueller Ellipsometer with Nematic Liquid Crystals for Macroscopic Samples

We now describe an imaging ellipsometer for macroscopic samples (up to 4 cm in size) using PSG and PSA based on nematic liquid crystal variable retarders, previously described in Sect. 2.6.3.3. This approach seemed indeed the most appropriate for an instrument used to image static samples, as the acquisition time (of the order of 10 s) was not an issue while the condition numbers of **W** and **A** could be minimized for each chosen wavelength. Actually, this instrument was installed in 2009 in the Pathology Department of Institut Mutualiste Montsouris hospital in Paris, and has been used to image dozens of samples such as those briefly presented in Sect. 2.7.4.

A schematic view of the optical assembly is represented in Fig. 2.27. The illumination part of the set-up comprises a halogen lamp (Olympus CLH-SC 150 W), a fiber bundle with its output at the focus of an aspherical condenser (Newport KPA046, $f1 = 37$ mm) followed by an achromatic lens (Edmund Optics NT- 32-886, $f2 = 150$ mm) whose focal point F coincides with the condenser's one. This combination is both telecentric in the object and images the fiber output onto the PSG. As all points of the NLCs are illuminated with the same angular aperture (defined by the aperture stop), the polarization generated by the liquid crystals is spatially uniform in spite of the angle-dependency of the liquid crystal retardation. Finally, a third lens images the PSG on the sample plane, illuminating a 5 cm diameter zone with very uniform intensity and polarization throughout.

The sample was imaged on a fast CCD camera (Dalsa CAD1, 256×256 pixels, 12 bits) by means of a $12.5 - 75$ mm zoom with an additional 500 mm close-up lens to "reject" the sample image at infinity, in order to use the zoom. This arrangement allowed an efficient rejection of any stray light. The wavelengths could be chosen between 400 and 700 nm in 50 nm steps by means of interference filters with 20 nm bandwidth placed before the close-up lens.

The PSG and PSA were built according to the optimized design defined in Sect. 2.6.3.3, [71] with a dichroic linear polarizer (Melles Griot, 03 FPG 007) followed by two nematic LCVRs (Meadowlark LVR 300). The four NLCs of the PSG and PSA were sequentially switched with frequencies in ratios 1, 2, 4 and 8 to generate the 16 needed polarization states. The dark current, which depended on the room

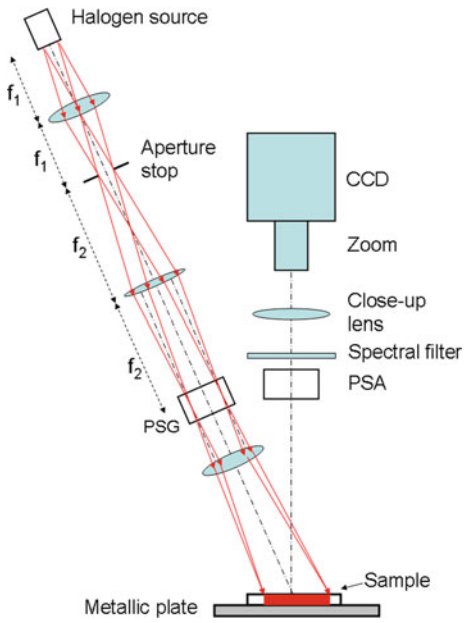

Fig. 2.27 Scheme of the imaging Mueller ellipsometer in reflection

temperature was measured frequently and subtracted from the signal for each pixel. A satisfactory signal-to-noise ratio was achieved by typically averaging 7 images for each state of polarization. A complete set of 16 averaged raw images was taken in about 11 s.

Typically, the reciprocal condition number of the PSG and the PSA were of the order of 0.45, thus quite close to the theoretical maximum of 0.57. The polarimetric accuracy, evaluated with a polarizer and a retardation plate set a various azimuths in either the illumination or the detection arm, was of the order of 3 % (maximum errors), which turned out to be more than sufficient for polarimetric imaging of surgical samples. However, a "run" of improvement of this instrument is planned for the near future.

Impact of the choice of the reference frame basis. With instruments operating in reflection at, or close to, normal incidence, special attention has to be paid to the definition of the (**s, p**) and ($\mathbf{s}'$, $\mathbf{p}'$) bases for incident and emerging beams, whose directions of propagation are defined by the vectors **z** and z' respectively. Far from normal incidence, the most natural (and the most widespread !) choice is that shown, for instance, on Fig. 2.11: $\mathbf{s} = \mathrm{s}'$ and both **p** and $\mathbf{p}'$ have positive components on the outgoing surface normal. By doing so, the 3D bases (**p**, **s**, **z**) and ($\mathbf{p}'$, $\mathbf{s}'$, $\mathbf{z}'$), are both right handed. If this choice is maintained up to normal incidence, the result is:

$$(\mathbf{p}', \mathbf{s}', \mathbf{z}')^{+} = (-\mathbf{p}, \mathbf{s}, -\mathbf{z}) \tag{2.116}$$

with this (usual) convention the Mueller matrix $\mathbf{M}_m^+$ of a mirror under normal incidence is

$$\mathbf{M}_m^+ = \begin{pmatrix} 1 & 0 & 0 & 0 \\ 0 & 1 & 0 & 0 \\ 0 & 0 & -1 & 0 \\ 0 & 0 & 0' & -1 \end{pmatrix} \tag{2.117}$$

The other possible choice for the emerging beam is to take the same basis (s, p) for both directions of propagation:

$$(\mathbf{p}', \mathbf{s}', \mathbf{z}')^- = (\mathbf{p}, \mathbf{s}, -\mathbf{z}) \tag{2.118}$$

Of course, in this case the $(\mathbf{p}', \mathbf{s}', \mathbf{z}')^-$ is no longer right-handed. But then the Mueller matrix $\mathbf{M}_m^-$ of a mirror under normal incidence is simply the unit matrix. More generally, if $\mathbf{M}^+$ is the Mueller matrix of a system in the usual (+) convention, then the Mueller matrix $\mathbf{M}^-$ of the same system in the other convention is obtained by changing the sign of the lower two lines.

As we will see in the following, many samples of interest for us behave as diagonal depolarizers, with $M_{22} = -M_{33}$ with the usual (+) convention and $M_{22} = M_{33}$ with the other choice. Obviously, it is much easier to visually check this relationship if the elements to be compared are supposed to be equal rather than opposite ! We thus decide to keep the "unusual" choice for the calibration of the imagers operating in reflection.

2.6.5.4 Imaging Mueller Ellipsometer with Nematic LCs Coupled to a Microscope

This instrument can be seen as the ultimate development of the well-known polarized microscopy, as the polarimetric characterization of the sample is complete, in contrast with the usual setups with crossed linear polarizers or left and right circular polarizers. An overall view of the imaging polarimeter [72, 73] is shown in Fig. 2.28.

A microscope objective (Nikon Plan Achromat 100×) with a high numerical aperture (0.90) is illuminated by a halogen source via a fiber bundle followed by an input arm comprising, among other elements:

- An *aperture diaphragm* 1, which is imaged on the objective back focal plane (BFP), and is used to define the *angular distribution* of the light incident on the sample,
- A *field diaphragm* 2, imaged on the sample, which allows to define *the size of the illuminated area* on the sample.
- The PSG 3, to modulate the incident polarization,
- A *nonpolarizing beamsplitter*, with approximately 50 % transmission and reflection coefficients, to steer the beam onto the microscope.

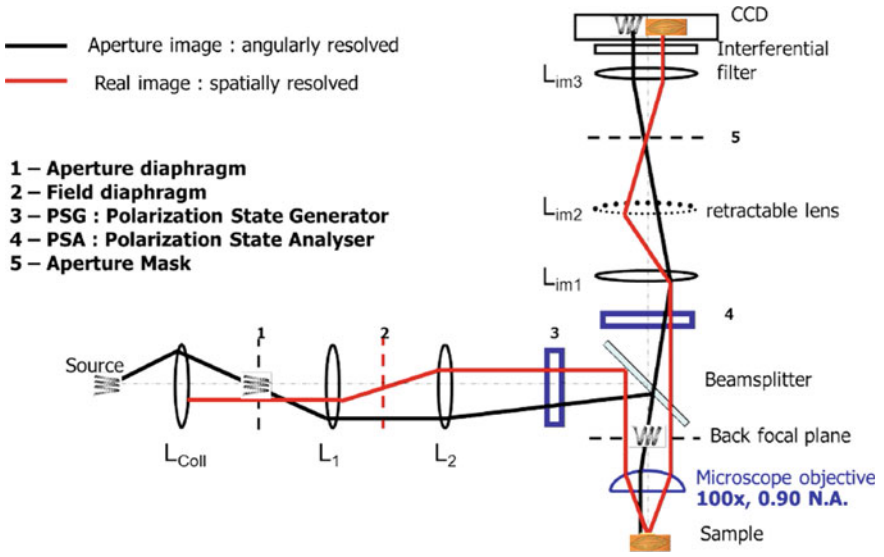

Fig. 2.28 Schematic representation of the imaging/conoscopic Mueller polarimeter

On the detection side, we find

- The *beamsplitter* again, working this time in transmission,
- The PSA 4 to analyse the emerging polarization,
- A set of two lenses which *image the objective back focal plane onto a two dimensional* imaging detector,
- A "retractable" lens which can be inserted in the beam path *to image the sample* instead of the objective back focal plane,
- An *aperture mask* 5 can be set in a plane conjugated with the objective BFP, typically to eliminate some strong contributions in order to see weaker ones, or to select the visualized diffraction orders if the sample is a grating.
- An interferential filter, typically quite narrow for metrological applications.
- The camera, a backthinned and cooled 512 × 512 pixel CCD from Hamamatsu.

The PSG and PSA operating in this setup are essentially the same as those used in the macroscopic imagers, though of smaller size. This choice was driven by the same considerations as for the macroscopic imager: the samples were static, and we considered it was important to be able to minimize the condition numbers at each wavelength [68, 74].

The angular distribution and the spot size characterizing the beam incident onto the sample can be adjusted independently of each other (at least as long as the illumination beam is far from being diffraction limited, a condition which is always fulfilled in practice with the classical light sources such as the one we use).

The two modes of operation of the microscope are illustrated on Fig. 2.29. The left panel shows the real space image of image of a grating, and the reciprocal space

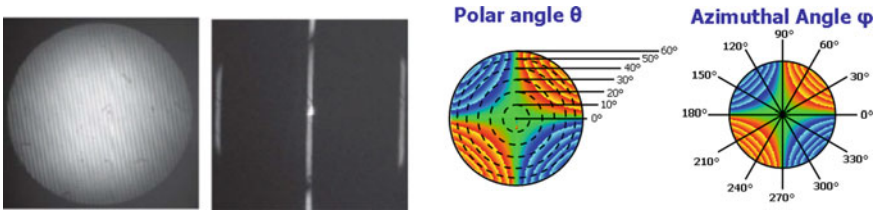

Fig. 2.29 *Left* Real-Fourier space images of a grating. *Right* Angular coordinates in the Fourier space (maximum aperture 62°). Images taken from Ref. [72] with the permission of Willey Science

image obtained with a slit as an aperture diaphragm and the grating as the sample: due to the presence of the slit, the angular distribution of the incident light is almost 1D, which is then diffracted in orders 0 (central line) and $+-1$ (lateral images).

The right panel of Fig. 2.29 shows how the angular distribution of the light coming from the sample is actually mapped on the objective back focal plane. Due to Abbe's sine condition [4] a parallel beam emerging from the sample with a polar angle θ and an azimuth ϕ is focussed in the back focal plane on a point with radial coordinates ($f \sin\theta$, ϕ), where f is the objective focal length. Of course, while all the azimuths between 0° and 360° are mapped, the polar angles θ are limited by the numerical aperture of the objective. In our case the nominal values are $\sin\theta_{\max} = 0.90$ and $\theta_{\max} = 65°$. In practice, it is difficult to achieve the full angular range. The radial coordinate is calibrated on the images by using diffraction patterns obtained with gratings with known pitches, such as the pattern shown in the left panel of Fig. 2.29, and our images are limited to about 60°.

Imaging in reciprocal space may constitute an interesting alternative to the more conventional approach of goniometric ellipsometry/polarimetry if angularly resolved data are to be acquired. Measurements along the polar angle at a fixed azimuthal angle of an image are equivalent to measurements taken at different angles of incidence on a non-imaging system. Accordingly, measurements recorded at a fixed polar angle and along the azimuthal direction on an image are equivalent to measurements taken rotating the sample holder in a non-imaging ellipsometer. With respect to simple conoscopy through crossed polarizers, full polarimetric conoscopy can be very useful to characterize anisotropic materials, as it provides angularly resolved maps of retardation (and diattenuation, if present) which significantly constrains the values of the dielectric tensor from easy and fast measurements [75] Moreover, under a powerful microscope objective, the *spot size can easily be reduced to* 10 μm *or less*, a possibility which can be very useful for some metrological applications, and more particularly in microelectronics, as we will see in Sect. 7.3. Obviously, so small spots sizes are much more difficult to obtain with the usual ellipsometric setups involving narrow beams with low numerical apertures.

As an example of Mueller images in the Fourier space we show in left panel of Fig. 2.30 the data taken on a silica thick plate. At first sight the observed patterns may seem surprising for an isotropic sample. In fact, the isotropy is "broken" by

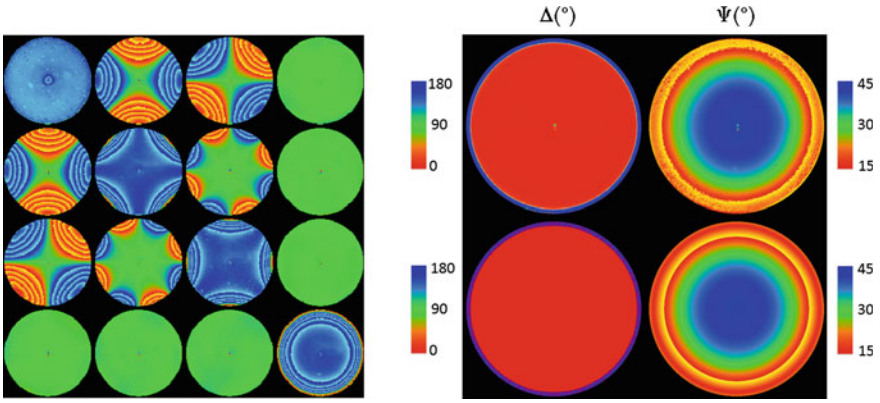

Fig. 2.30 *Left* raw Mueller images in the reciprocal space of a *thick plate* of silica. The basis vectors for the definition of polarisaton are vertical and horizontal all over the image. *Right*, *top* maps of angularly resolved Δ and Ψ derived from the Lu–Chipman decomposition of the data shown in the *left panel*. *Right bottom* corresponding simulations

the choice of the basis used to define the polarization, and which is uniform all over the image with one vector horizontal and the other vertical. Obviously, these are not the usual (*p, s*) vectors defined with respect of the incidence plane, and which would be oriented radially in each point of the image.

If the Lu–Chipman decomposition is applied to the raw image at the left of Fig. 2.30 we obtain essentially zero depolarization, and the angularly resolved values of Δ and Ψ shown in the right panel (top), together with the corresponding simulations (bottom). As expected, once Δ and Ψ are plot according to the conventional (s,p) coordinate system, both parameters display an almost perfect radial symmetry. Moreover Δ remains at zero, and then "jumps" to 180° at the Brewster incidence, while Ψ starts at 45° at the image center, and then decreases in agreement with the theory (the jump from red to light yellow indicates that the plotted value went below the minimum of the scale, here 15°).

These results clearly show that this technique may be very powerful. We give in Sect. 2.7.3 an example of application for the metrology of sub-wavelength gratings. However, it would be extremely difficult to "push" the accuracy of such measurements to the levels reached by usual, non-imaging ellipsometers. The main reason for this is that the objectives used in Fourier configuration may introduce some polarimetric artifacts which cannot be taken into account by the ECM method, as the system must be calibrated with the objective removed [72]. Moreover, even strain free objectives are extremely sensitive to mechanical constraints, and the resulting artifacts would probably evolve in time. In spite of these limitations in accuracy, Mueller microscopes (operating here in reflection, but transmission may be used too) are likely to open new research topics in many areas.

2.7 Examples of Applications of Mueller Ellipsometry

One of the interest of using Mueller ellipsometers is to access the whole Mueller matrix in a single measurement configuration to characterize samples with a complex optical response such as anisotropic layers or diffracting structures. Another interest of having broadband spectral measurements is to access different types of properties of the solids. In the following we provide three examples showing the performances of the above described systems to perform optical metrology of diffracting structures and to characterize the optical (and electrical) properties of thin metal films.

2.7.1 Characterization of Low Emissivity Coatings Using Broadband Mueller Ellipsometry and Standard Ellipsometry in Total Internal Reflection

In the first part of this chapter, it is stated that ellipsometry is an indirect technique, here we provide an example of a common way to work with ellipsometric data from non-depolarizing samples; i.e. the use of parameterized optical models to fit experimental data. This example also illustrates the advantages of using data in a broad spectral range and the interest of combining data from different sources and optical configurations to optimize the amount of information that can be obtained from the sample. In particular we show how to use optical data to study the dependence of the electrical properties (conductivity) of thin metallic layers with their thickness. The link between electrical and optical properties can be established because the infrared optical response of conducting materials is dominated by the dynamics of free charge carriers and can be written in terms of the electrical conductivity in the framework of the Drude model. We have worked with multi-layer stacks of aluminum doped zinc oxide, ZnO:Al, and silver, Ag, with the structure ZnO:Al/Ag/ZnO:Al. Silver layer thickness changed from sample to sample in the range from 8 to 50 nm, while the thickness of the ZnO:Al layers was kept constant (≈20 nm). ZnO:Al and Ag layers were deposited by magnetron sputtering. In the following we present a summary of a detailed study made on the set of samples. More information about measurements, parameterization of the dielectric function of the materials present in the samples, and fitting of data can be found elsewhere [76].

The optical characterization of the samples was performed with two techniques: spectroscopic ellipsometry and infrared reflectometry. Infrared reflectometry measurements were taken with a commercial (Bruker) FTIR Spectrophotometer in the spectral range from 4 to 30 μm. Spectroscopic ellipsometry measurements in the ultraviolet to the near-infrared (270–1600 nm) were performed with a commercial phase-modulated ellipsometer UVISEL (HORIBA Jobin-Yvon). Mueller ellipsometric data in the mid-infrared were measured with the Mueller ellipsometer described in Sect. 2.6.5.1 The angle of incidence was the same, 68.5°, for the UVISEL and

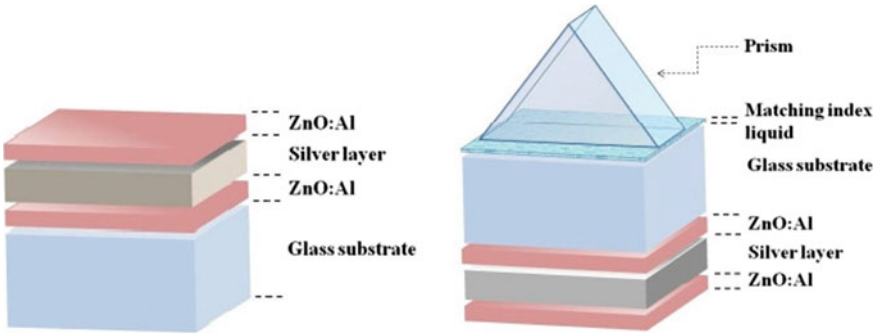

Fig. 2.31 *Left* sketch of the ZnO:Al/Ag/ZnO:Al stack on a glass substrate. *Right* sketch of TIR configuration used and the orientation of the sample. The prism used for TIR measurements was cut at an angle of 57.6°

the broadband Mueller ellipsometer in order to have continuous data. Measurements were performed from the coated side as depicted in Fig. 2.31. Total internal reflection ellipsometric (TIR) measurements were performed using the UVISEL spectroscopic ellipsometer because the most prominent spectral features appear at visible frequencies. The TIR measurement configuration, sketched in Fig. 2.31, consists of a BK7 prism optically matched to the substrate by an oil designed for this purpose. Measurements were performed from the substrate side of samples as depicted in Fig. 2.31.

Experimental data for all samples was interpreted on the basis of a common model of the structure which included as parameters the thickness and dielectric functions of the three layers. The dielectric function of the substrate was considered as well. The dielectric function of the glass at infrared frequencies was described with a combination of four Lorentz oscillators (OS) whereas in the ultraviolet it was represented using the Tauc-Lorentz (TL) model [3, 31, 77]. ZnO:Al showed strong ultraviolet absorption due to interband transitions which were modeled with a TL formula with two oscillators. Silver is a noble metal which shows a noticeable absorption in the whole spectral region from the infrared to the ultraviolet. Above the plasma frequency the absorption is governed by interband transitions, and below it by intraband absorptions due to free carriers. Free carrier contribution was modeled with the Drude expression, whereas interband transitions were modeled with TL expression.

Glass substrate was characterized following the example given in [78]. Ellipsometry and reflectometry measurements were performed on both sides of the uncoated glass substrate. In Fig. 2.32, we provide a comparison between best-fitted data and experimental values obtained for the glass substrate at the air side. In addition, the values of the refractive index and absorption coefficient deduced from the best-fitted parameters are also plotted in the same figure.

For the characterization of optical properties of ZnO:Al we worked with a sample consisting of a glass substrate coated with a 30 nm layer of ZnO:Al. The optical model of the sample was identical to the glass substrate with an additional layer

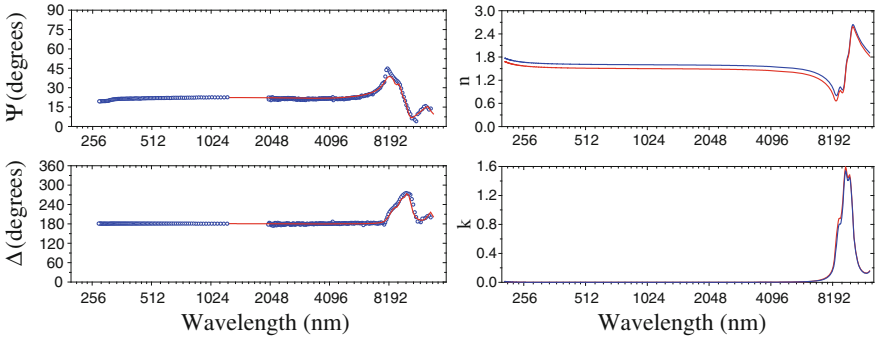

Fig. 2.32 *Left* experimental (*blue dots*) and best-fitted (*red lines*) values for the ellipsometer angles Ψ and Δ corresponding to the air side of the glass substrate. *Right* best-fitted refractive index n, and absorption coefficient k, corresponding to bulk glass (*red line*) and glass with tin (*blue line*). Spectral range spans from the ultraviolet to the mid infrared, the wavelength axis of both figures is represented in a logarithmic scale

representing the ZnO:Al film. In Fig. 2.33, we provide a comparison between the best-fitted and the experimental data obtained for the ZnO:Al sample. The same figure also shows the values of the refractive index and the absorption coefficient deduced from the fitted data.

Unlikely to zinc oxide, it is not possible to characterize a single layer of silver because it oxidizes quickly in contact with the air. In order to work with silver, we had to use the complete ZnO:Al/Ag/ZnO:Al tri-layer samples. We measured the sample having the thickest film, 50 nm. From the set of parameters characterizing the Ag optical response, the most relevant for the purposes of the present example are only two: the plasma frequency, ω_p, and the Drude damping factor, Γ_D. The best-fitted value of ω_p was 9.2 ± 0.2 eV and it was found to be stable from sample to sample [76, 79]. On the contrary, the value of the Drude damping, which is the inverse of the mean time among two collisions of electrons, was expected to strongly depend on the thickness of the silver layers. Considering that the mean free path (MFP) of electrons in bulk silver is about 40 nm, it is not surprising that once dimensions of the layer become of the same order or even smaller than MFP, the interfaces of the film as well as the microcrystalline grain boundaries, have a non-negligible impact on the kinetics of free electrons. The fitted value for Γ_D for the thicker layer was about 0.038 eV, a value which is compatible with the literature.

Once the dielectric functions of the materials were known, it came the problem of fitting the three layer system. It was found that it was not possible to fit properly the thickness of the three layers and the Drude damping using either ellipsometric data in external configuration alone or reflectometry data alone. The problem was the strong numerical correlations between parameters. This limitation is due to the loss of information contained in optical data because of the absorption of the Ag layer. To circumvent this problem we added to our fitting procedure the measurements performed in TIR configuration. This approach allowed to enhance the sensitivity

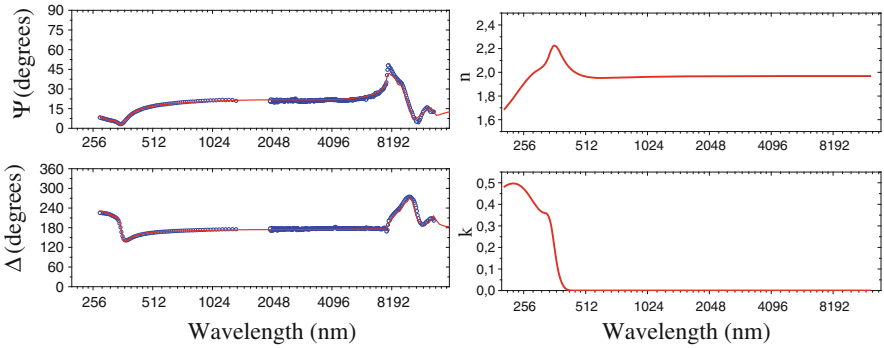

Fig. 2.33 *Left* experimental (*blue dots*) and theoretical (*red lines*) values for the ellipsometric angles Ψ and Δ corresponding to the ZnO:Al single layer sample. *Right* best fitted refractive index, n, and absorption coefficient, k. Spectral features visible in Ψ and Δ at infrared wavelengths larger than 8 μm are created from the glass substrate. Spectral range spans from the ultraviolet to the mid infrared, the wavelength axis of both figures is represented in a logarithmic scale

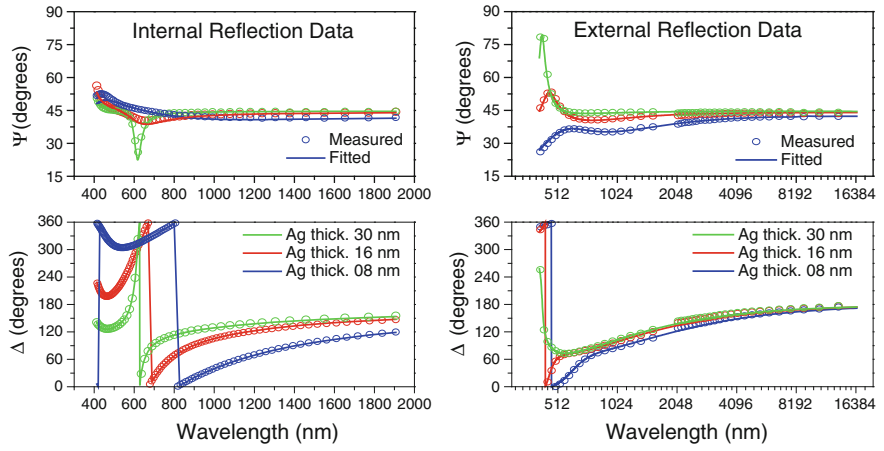

Fig. 2.34 Experimental (*circles*) and best-fitted (*lines*) Ψ and Δ spectra corresponding to samples with silver thickness of 8 (*blue*), 16 (*red*) and 30 (*green*) nm. *Left* ellipsometric data in TIR configuration. *Right* ellipsometric data in external configuration

of measurements and to remove most of the numerical correlations. In Fig. 2.34 we have represented the experimental and the best-fitted ellipsometric data for three representative samples.

The main advantage of using ellipsometer in TIR configuration is the excitation of resonant surface plasmon waves on metal/dielectric interfaces [80–83]. When the metallic surface is covered with thin films, the field distribution and the propagation characteristics of plasmons are strongly influenced by the thickness and refractive index of these layers. Contrarily to standard propagating (plane) waves, the way surface plasmons interact with thin films is substantially non-interferometric, which

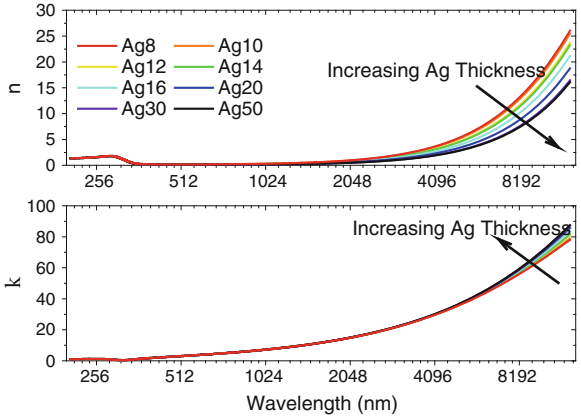

Fig. 2.35 Spectral dependence of the values of the refraction index, n, and the absorption coefficient, k, for each sample studied. The *arrows* indicate spectra corresponding to samples with increasing silver layer thickness. Spectral range spans from the ultraviolet to the mid infrared, the wavelength axis of both figures is represented in a logarithmic scale

explains why surface plasmons can retrieve an information which is not affected by the same limitations as that carried by light beams in external configuration and thus, enhance the sensitivity of ellipsometric measurements.

As expected, we observed that Γ_D increased when the thickness d_{Ag} decreases. Γ_D is proportional to the collision frequency. The observed behavior of Γ_D is explained because when the silver layer thickness decreases, scattering of electrons at the layer interfaces and at grain boundaries becomes non-negligible and it adds-up to the intrinsic bulk scattering by phonons and impurities. The value of Γ_D impacts considerably the refractive index and the absorption coefficient of the Ag layer specially at long wavelengths. As shown in Fig. 2.35, the refractive index decreases and the absorption coefficient increases when Γ_D increases.

In order to study the dependency of Γ_D with the silver layer thickness, the optical conductivity of each sample was calculated from the fitted data and compared with the corresponding values of the measured electrical conductivity. In the framework of the Drude theory the optical conductivity can be calculated as follows: [3]

$$\sigma_{c,opt} = \frac{\varepsilon_0 \omega_p^2}{\Gamma_D} = \frac{1}{\rho_{c,opt}}$$

According to [84, 85] the most convenient is not to represent resistivity, but the resistivity times the thickness of the silver layer, $\rho_c d_{Ag}$, as a function of the silver layer thickness itself. It can be shown that for metals this relation is linear. The slope of the line is related to the intrinsic resistivity of the silver layer, ρ_0, and the cut with the y-axis gives information about the influence of the surface scattering. In Fig. 2.36

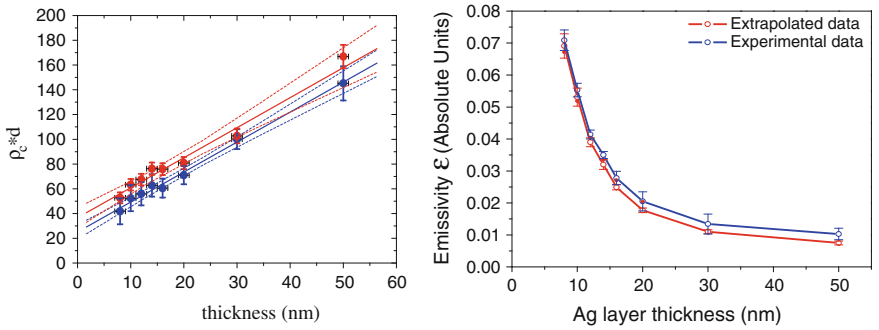

Fig. 2.36 *Left* electrical (*blue spots*) and the optical (*red spots*) results in terms of the $d_{Ag}\rho_c$ product as function silver layer thickness d_{Ag}. Linear regression of the experimental electrical data (*blue line*) and optical data (*red line*) are represented together with the corresponding 95 % confidence intervals (*blue* and *red dotted lines*). *Right* experimental (*blue*) and extrapolated (*red*) emissivity as a function of the Ag layer thickness for the whole set of samples

are represented the values of the product $\rho_c d_{Ag}$ obtained with optical and electrical measurements respectively as a function of d_{Ag}.

The slope of the linear regression (also shown in the figure) corresponding to the electrical and optical data were $(2.1\pm0.9)\mu\,\Omega$ cm and $(2.1\pm0.3)\mu\,\Omega$ cm respectively. These values are slightly higher than the value for bulk monocrystalline silver at room temperature, $1.59\,\mu\,\Omega$ cm, because the silver in our samples was polycrystalline. To validate the results obtained from optical data fitting, we compared the emissivity extrapolated from the optical model for each sample with experimental data. The results, shown in Fig. 2.38, prove that the high accuracy of the optical model allows to predict emissivity which matches very well with experimental data.

In summary, in this example we wanted to illustrate the way to treat ellipsometric data from non-depolarizing samples and also to show the interest of combining data from different sources in a wide spectral range to optimize the amount of information that can be obtained from the sample. In our particular example we have applied a combined approach to characterize a tri-layer structure in which an Ag layer was stacked between two ZnO:Al layers. We have used Mueller ellipsometric data in the infrared to obtain the optical properties of Ag layers, which are responsible of the thermal emissivity of the coatings. Moreover, the enhanced sensitivity due to the penetration of surface plasmons through the tri-layer stack measured in TIR configuration, allowed us to achieve the better accuracy for the thickness of the layers. The validation of the method using an independent measurement (emissivity), confirmed the accuracy of characterization achieved with ellipsometry.

This example shows how Mueller ellipsometric data in the infrared can be used to study the dependence of the electrical properties (conductivity) of thin metallic layers with their thickness. The link between electrical and optical properties can be done because the infrared optical response of conducting materials is dominated by the dynamics of free charge carriers. We have studied multi-layer stacks of aluminum doped zinc oxide, ZnO:Al, and silver, Ag, forming the structure ZnO:Al/Ag /ZnO:Al

with thin Ag films of following thicknesses: 8, 10, 12, 14, 16, 20, 30, and 50 nm. The thickness of the ZnO:Al layers was kept constant (≈20 nm). ZnO:Al and Ag layers were deposited by magnetron sputtering. In the following we present a summary of a detailed study made on the set of samples, here we want to highlight the benefits of having optical data in a broad spectral range.

2.7.2 *Characterization of Spatially Inhomogeneous Samples by Sum Decomposition of the Measured Mueller Matrix*

This example illustrates one practical use of the sum decomposition, the retrieval of non-depolarizing components of a depolarizing Mueller matrix. A beam which shines two parts of a sample with different optical properties can lead to depolarizing Mueller matrices because the two responses add-up incoherently in the detector. This situation can easily occur when it comes to measure samples with characteristic size comparable to the size of the probe beam. If the alignment of the sample with the beam is not extremely accurate, a portion of the beam may fall outside of the sample, then the combination in the detector of beam parts having fallen inside and outside the sample causes the measured Mueller matrix to be depolarized. This example shows how to separate the Mueller matrix of the sample from the Mueller matrix of the surrounding substrate provided that both matrices are non-depolarizing and the matrix of the substrate is known. The adequate decomposition to treat this simple example is the Cloude decomposition.

The sample consisted of a one-dimensional diffraction grating etched on a photoresist deposited on the surface of a silicon wafer. More details about the grating profile and the etching procedure can be found elsewhere [86]. The size of the etched area containing the grating was about 3×3 mm, large enough to contain the spot size of the Mueller ellipsometer, $200 \times 400\,\mu$m projected on the sample when the grating was properly aligned. The etching process removed the photoresist coating surrounding the grating, leaving exposed the surface of the bare silicon substrate. Therefore, the measured signal could come from the substrate, from the sample or from a mixture of both depending on the alignment of the beam. The lines of the grating were oriented at 45° respect to the plane of incidence to maximize the difference between the polarimetric optical response of the grating and the surface.

As shown in Fig. 2.37, the measurement process started positioning the beam perfectly aligned to the center of the grating and measuring the corresponding Mueller matrix. Then, the beam was slightly shifted from the initial position and the sample was measured again. The procedure was repeated until the entire beam spot fell well outside the grating. The goal was to measure the depolarization of all the measured matrices, to separate the depolarizing matrices in two components, and to measure the relative weight of each non-depolarizing component as a function of total shift of the beam respect to the initial position. The matrices of the initial and the final steps corresponding to the grating and the substrate respectively, were found to be non-depolarizing. Ellipsometric measurements were performed with a com-

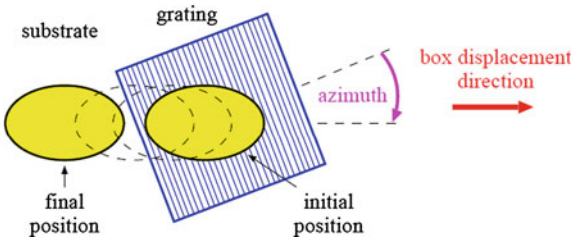

Fig. 2.37 Schematic representation of the sample and the measurement procedure. The *stripped square* represents the grating whereas the *white* area surrounding it represents the silicon substrate. The *yellow ellipses* represent the projection of the spot size on the sample surface in the initial and the final step. A few intermediate measurement steps are represented by the *dashed ellipses*. Picture taken from [86] with the authorization of the authors and the publisher

mercial liquid crystal based spectroscopic Mueller matrix ellipsometer (MM16 from HORIBA Jobin-Yvon), operating in the visible range (450–850 nm with a spectral step of 1.5 nm) previously described in this chapter.

The method to separate the Mueller matrix of the grating from the experimental Mueller matrix is based on the Cloude sum decomposition. This decomposition implies to work with coherence matrices given by expressions (2.43) or (2.18). Because in this particular experience, there are two components that can contribute to the detected signal, the grating and the substrate, the rank of the coherence matrix $\mathbf{N^e}$ associated to the depolarizing measured Mueller matrix, $\mathbf{M^e}$, must be two (2). It is assumed that both the substrate and the grating are non-depolarizing, thus their respective Mueller matrices $\mathbf{M^s}$, and $\mathbf{M^g}$, have associated matrices $\mathbf{N^s}$ and $\mathbf{N^g}$ of rank one. According to the experimental conditions, the normalized depolarizing Mueller matrix $\mathbf{M^e}$ resulting from the sum of two normalized non-depolarizing matrix components $\mathbf{M^s}$ and $\mathbf{M^g}$ can be written in form:

$$\mathbf{M^e} = \frac{1}{1+p}\left(\mathbf{M^g} + p\mathbf{M^s}\right) \tag{2.119}$$

where the coefficient p accounts for the relative weight of the two non-depolarizing matrices. Therefore, when $\mathbf{M^e}$ and $\mathbf{M^s}$ are known, it is always possible to use find unique real number, α, such that the rank of the matrix $(\mathbf{N^e} - \alpha\,\mathbf{N^s})$ equals one [87]. The solution of this algebraic problem can be performed numerically with an algorithm that searches the value of parameter α by minimizing the values of three eigenvalues associated to the matrix $(\mathbf{N^e} - \alpha\,\mathbf{N^s})$. Ideally, for the matrix $(\mathbf{N^e} - \alpha\,\mathbf{N^s})$ to be of rank one, three of its four eigenvectors must be zero. Because the matrices are experimental, they have some noise, then for practical reasons related to the minimization routine, the noise level is numerically considered as zero. Once the value of the parameter α is known, the normalized Mueller matrix $\mathbf{M^g}$ an be written in terms of $\mathbf{M^e}$ and $\mathbf{M^s}$ as:

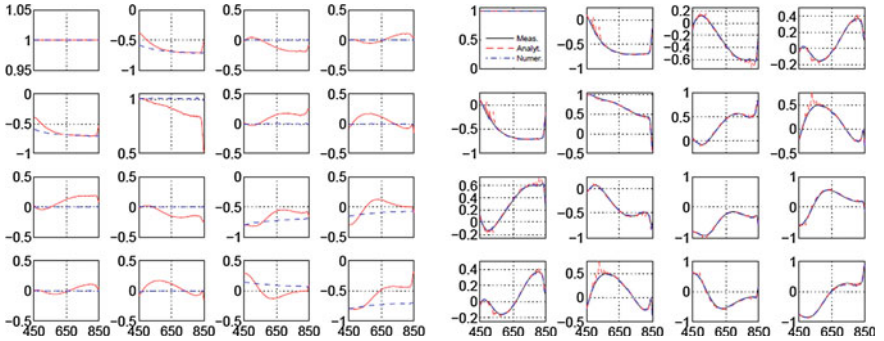

Fig. 2.38 *Left* experimental data corresponding to a normalized depolarizing Mueller matrix $\mathbf{M^e}$ (*solid red line*) and the normalized non-depolarizing Mueller matrix of the substrate $\mathbf{M^s}$ (*dashed blue line*). The different boxes arranged in 4×4 arrays correspond to each one of the sixteen elements of the normalized Mueller matrices. *Right* spectral values of the numerically (*dash-dotted blue line*) retrieved Mueller matrices compared with the directly measured matrix of the grating (*solid black line*). The *dashed blue lines* correspond to an alternative way to calculate the coefficient α, not commented in this chapter. More details about the alternative method can be found in [88] from which the figure has been reproduced with the authorization of the authors and the publisher

$$\mathbf{M^g} = (1+p)\,\mathbf{M^e} - p\mathbf{M^s} \quad \text{with} \quad p = \left(\frac{\alpha}{1-\alpha}\right) \tag{2.120}$$

Therefore, the method allows the extraction of the unknown non-depolarizing component $\mathbf{M^g}$ from the original depolarizing matrix by subtracting the right proportion of the known component $\mathbf{M^s}$. The method can be further generalized to extract more than one non-depolarizing component from the depolarizing matrix [88]. Figure 2.38 shows one of the depolarizing Mueller matrices $\mathbf{M^e}$ and the non-depolarizing Mueller matrix $\mathbf{M^s}$. The same figure also shows the matrix $\mathbf{M^g}$ resulting from the decomposition of matrix $\mathbf{M^e}$ together with the experimental matrix of the grating measured alone (first step in the measurement process). The overall correspondence between measured and numerically reconstructed matrices is very good, which shows the validity of the extraction procedure.

In summary, this example illustrates one of the possible uses of the Cloude decomposition, i.e. the extraction of pure non-depolarizing matrices, which can be in turn analyzed using ellipsometric models, from depolarizing matrices. A method to implement the subtraction has been presented. The robustness of the method is illustrated in an example concerning depolarizing Mueller matrices containing two non-depolarizing components, a diffraction grating and a silicon substrate respectively.

2.7.3 Subwavelength Grating Metrology

In this section we focus on the profile reconstruction of diffraction gratings. Optical methods (also called "scatterometry") are fast, non-destructive and may exhibit strong sensitivity to tiny changes in grating profiles [89]. As a result, they are becoming increasingly popular for process control in microelectronics industry [90]. On the other hand, these methods are indirect, and the reconstructed profiles may depend on the model used to fit the data (and the dielectric function of somewhat "ill-defined" materials like resists.) Possible model inadequacies do not necessarily appear in the goodness of fit. Parameter correlations may also constitute a serious issue, as shown in a comprehensive study of the results of scatterometric reconstruction by the usual techniques (normal incidence reflectometry and planar diffraction spectroscopic ellipsometry) of various profiles representing different technological steps [91]. In this context, Mueller ellipsometry may constitute an interesting alternative, provided the data are taken in conical diffraction geometries. In conical diffraction configurations, the symmetry axes of the grating structure are neither parallel or perpendicular respect to the plane of incidence. Indeed, in such geometries the grating Jones matrix is no longer diagonal (and the Mueller matrix no longer block-diagonal). As a result, additional information is available, and may help in constraining the fitting parameters. Moreover, the stability of the optimal values of these parameters when the azimuth is varied may constitute a much better test of the model relevance than goodness of fit at a single azimuth [92]. The principle of ellipsometric measurements is sketched in Fig. 2.39. The relevant parameters characterizing the measurement are the angle of incidence, θ, and the azimuthal angle φ, which is the angle between the plane of incidence and one of the axes of symmetry of the sample. For one-dimensional gratings, the azimuth is defined to be zero when the grooves are aligned perpendicular to the plane of incidence. Only in the case the grooves are ori-

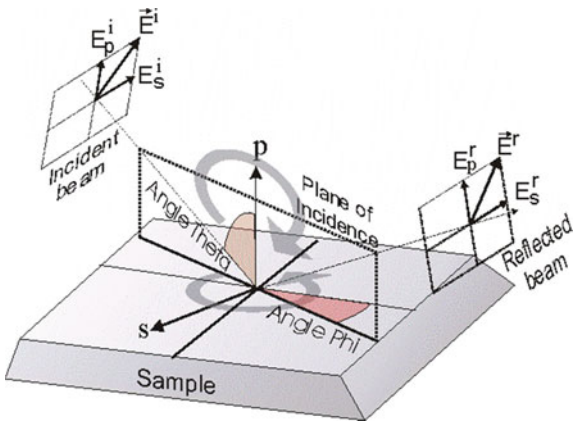

Fig. 2.39 Sketch of a typical Mueller ellipsometric configuration to perform measurements in conical diffraction mode. The relevant angles are the angle of incidence, θ, and the azimuthal angle φ. In the figure only the zero order diffracted beam is represented for simplicity reasons

ented parallel or perpendicular to the plane of incidence the measurement geometry is called planar diffraction.

For non-depolarizing samples, either Jones or Mueller formalisms are valid to represent the properties of the sample and Mueller matrices can be related to Jones matrices with expression (2.14). This particular representation of Mueller matrices is useful to discuss the symmetry properties of the Mueller matrix of a sample measured in conical diffraction. Li demonstrated in [93] that the off-diagonal elements of the Jones matrix are anti-symmetric for symmetric structures as a result of the electromagnetic reciprocity theorem. Translating this condition to expression (2.14) gives a Mueller matrix which satisfies the following symmetry $M_{12} = M_{21}; M_{14} = M_{41}; M_{24} = M_{42}$ and anti-symmetry conditions: $M_{13} = -M_{31}$; $M_{23} = -M_{32}$; $M_{34} = -M_{43}$. Figure 2.40 show schematically all these relations:

When the a symmetric grating is rotated azimuthally of $\pm 180°$ the resulting geometry is equivalent to the original non-rotated one, except that the s component of the electric field have changed its sign. In other words, "p(φ)" = "p($\varphi \pm 180$)" "s(φ)" = $-$"s($\varphi \pm 180$)". This transformation makes the signs of all the off-diagonal elements of a rotated Mueller matrix to change respect to the elements of the non-rotated matrix. In particular for a symmetric grating the following relations are always satisfied:

$$\begin{aligned}
M_{13}(\varphi) &= -M_{13}(\varphi \pm 180°) = -M_{31}(\varphi) = M_{31}(\varphi \pm 180°);\\
M_{14}(\varphi) &= -M_{14}(\varphi \pm 180°) = M_{41}(\varphi) = -M_{41}(\varphi \pm 180°);\\
M_{23}(\varphi) &= -M_{23}(\varphi \pm 180°) = -M_{32}(\varphi) = M_{32}(\varphi \pm 180°);\\
M_{24}(\varphi) &= -M_{24}(\varphi \pm 180°) = M_{42}(\varphi) = -M_{32}(\varphi \pm 180°);\\
M_{34}(\varphi) &= -M_{34}(\varphi \pm 180°) = -M_{43}(\varphi) = M_{43}(\varphi \pm 180°);
\end{aligned} \tag{2.121}$$

These symmetry relations under rotation (2.121), are not fulfilled if the grating is not perfectly symmetric. The lack of symmetry can be due the presence of overlays or just because of imperfections of the grating profile occurred during the fabrication process. In many practical situations, the asymmetric effects due to overlays are small, and may be comparable in magnitude to the measurement errors of standard ellipsometric systems. In those cases, the fact of being able to measure a full Mueller matrix allows to profit the redundancies of all elements of the Mueller matrix to achieve an optimal discrimination between overlay effects and experimental measurement errors. Therefore, when only partial Mueller matrix are available, an extra-care must be taken in order to not mix-up both effects. In the following we show two examples of use of measurements of gratings in conical diffraction to characterize diffraction gratings. The first example is about profile reconstruction using spectroscopic Mueller matrices and the second example illustrates the use of the imaging Mueller ellipsometer to characterize small overlays.

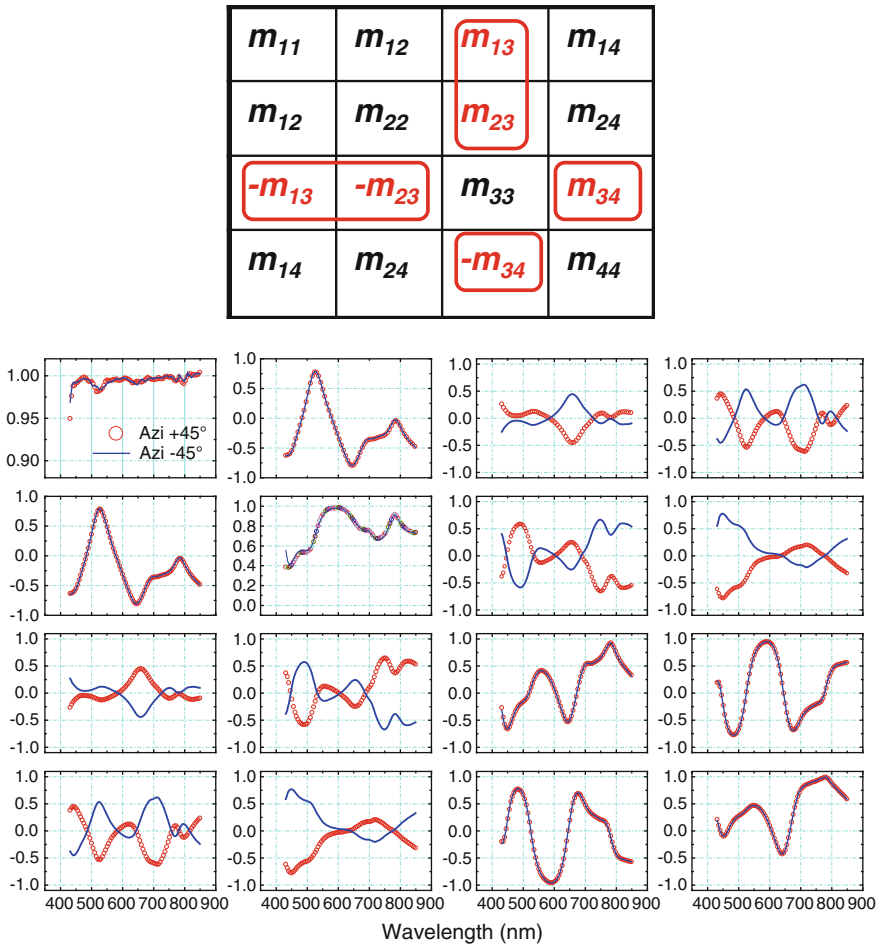

Fig. 2.40 *Top* schematic representation of the Mueller matrix of a symmetric grating, showing in *black* and in *red* the elements showing a symmetric an anti-symmetric relation respectively. Diagonal elements are not subjected to symmetry relations. *Bottom* spectroscopic Mueller matrix of a one-dimensional grating measured at two azimuths, $+45°$ (*red circles*) and $-45°$ (*blue line*) and at angle of incidence of 45°. Two types of symmetries can be seen. The off-diagonal elements of the matrix at azimuth $+45°$ have opposite sign respect to those of the matrix at -45, whereas the rest of elements have equal sign. Moreover for every single Mueller matrix, the symmetries among its respective elements, schematically show in the figure on *top*, are always respected

2.7.3.1 Profile Reconstruction by Spectroscopic Mueller Ellipsometry at Discrete Angles

Here we will summarize the main results of a study which goal was to show the possibility of using Mueller ellipsometry data for reconstruction (optical metrology) of diffraction gratings profile. The sample analyzed consisted of a silicon wafer

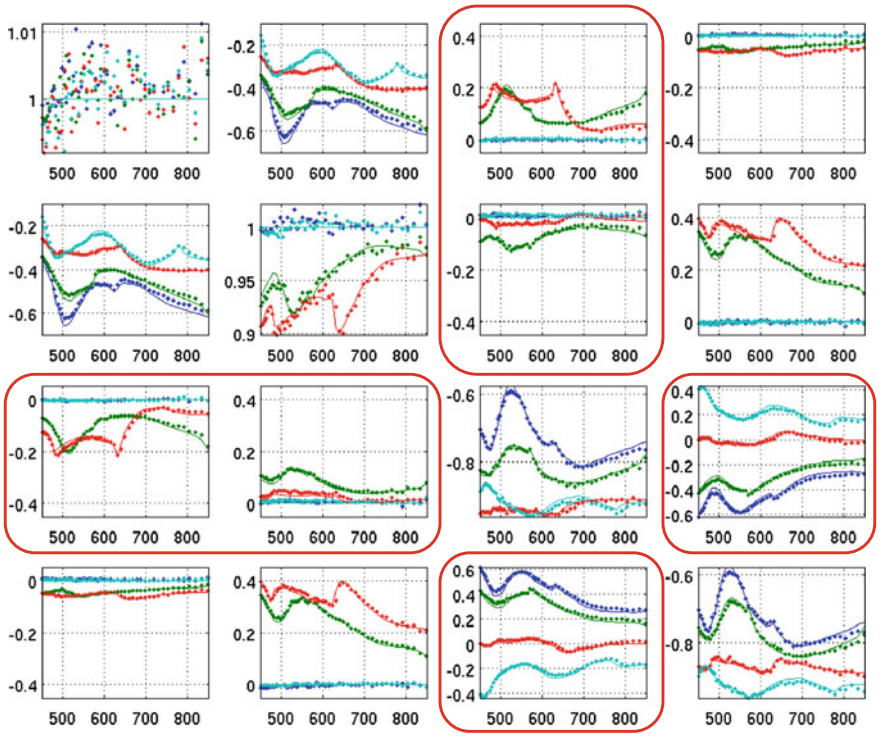

Fig. 2.41 Measured (*dots*) and fitted (*lines*) spectroscopic Mueller matrices for azimuthal angles of 0° (*blue*), +30° (*dark green*), +60° (*red*) and +90° (*light green*) and incidence angle of 45°. Spectral range spanned from 450 to 850 nm. Images taken from Ref. [71] with the authorization of the authors and the publisher

with a series of silicon gratings etched on it using UV beam lithography. Typical dimensions for the gratings were: groove depths around 100 nm, line widths around 130 and 250 nm, and pitches from 500 to 1100 nm. Each individual grating was etched in an area of 3 × 3 mm. Etched silicon gratings were chosen for this study because of their long term dimensional stability, higher refractive index contrast and relevance to semiconductor industry. For reference, the dimensions of the profiles of the gratings were determined by the state of the art 3D AFM microscope. For the sake of simplicity we show here the results corresponding to only one grating. For more details, please refer to [94]. Experimental data was taken by an Horiba Jobin-Yvon Mueller ellipsometer (MM16), operating in the visible (450–850 nm) [68]. A series of measurements were taken varying the azimuth over 360° in steps of 5°. The incidence was kept constant at 45° to make sure the beam diameter at the sample was small enough to safely maintain the spot within the grating. Four of the measured spectroscopic matrices, corresponding to azimuthal angles 0, +30, +60 and 90°, together with the corresponding fits, are shown in Fig. 2.41. The matrix elements are normalized by the element M_{11}, and thus they vary from −1 to 1. The redundant information in the Mueller matrix allows to evaluate the quality of

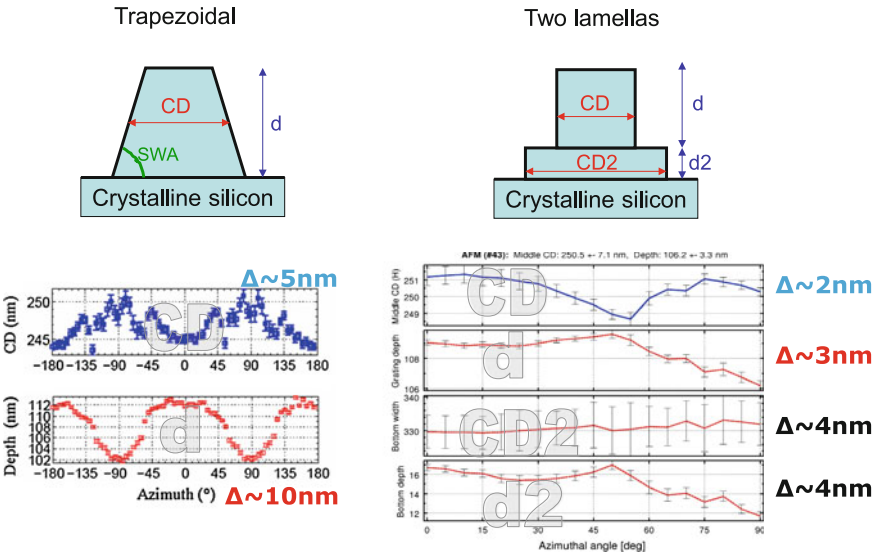

Fig. 2.42 *Left top* profile representing the trapezoidal model with the two characteristic parameters, the CD, the thickness and the SWA. *Left bottom* resulting best-fitted values for the parameters CD and thickness at different azimuths. The corresponding variations are indicated by the symbols Δ. *Right top* profile representing the double lamella model with the four characteristic parameters. *Right bottom* results of the fit of four free parameters of two lamellas model over different azimuthal angles. Error bars in figures denote statistical errors. The maximum variation of each parameter is indicated with the symbol Δ. Images taken from Ref. [94] with the authorization of the authors and the publisher

the measured data by simple criteria such as the degree of polarization, expression (2.19), or the symmetry of the off-diagonal elements (2.121). In the upper left corner panel of Fig. 2.41 there is plotted the degree of polarization, which was found to be very close to 1, indicating that no depolarization phenomenon occurs because of the high quality of both sample and data. The blue and green spectra coincide in the diagonal blocks, while they are opposite in the off-diagonal blocks. These symmetries provide a robust test of the accuracy of both the measurements and the sample azimuthal position.

The measured data were fitted by RCWA simulations [95] formulated in the Mueller–Jones formalism [73]. The profile of the gratings was represented using different models. For the sake of clarity here we discuss only two models. The first model assumed the profile to be trapezoidal. In the second model the grating profile was represented by the superposition of two rectangular lamellas. Both models are sketched in Fig. 2.42. The trapezoidal model depends on three adjustable parameters, the thickness, d, the CD (with) of the lines, and the trapeze angle (SWA). The second model depends on four parameters, the CDs and the thickness of the two lamellas. The resulting best-fitted parameters for both models are presented in Fig. 2.42. In general both models provided fits of same quality, but the most prominent difference among

them was the dependence of the best-fitted parameters with the azimuth angle at which the measurements were taken. Whereas best-fitted parameters corresponding to the model of two lamellas showed a low dependency with the azimuthal angle, CD2 values are dispersed by less than 1.5 nm and the grating depth varies by less than 2 nm around 108 nm, the parameters fitted with the trapezoidal model showed strong fluctuations, 5 nm for the CD and 10 nm for the thickness. The second element that makes the difference between both models is the correlation between fitted parameters. A close look to the values of the CD and the thickness corresponding to the trapezoidal model reveals that them are strongly linearly correlated. This means that the data does not carry the information needed by the model to discriminate the particular influence of each parameter. In contrast, regarding the bi-lamellar model only a small correlation between the overall grating depth and the bottom lamella depth can be observed in this figure. The low amount of correlation and dependency of the fitted parameters with the observation conditions, show that the bi-lamellar model represented better the profile than the trapezoidal model. The adequacy of the model was also confirmed by comparing the obtained profile with AFM measurements. Similar results have been obtained on all the gratings of the sample.

In summary, this example shows that Mueller ellipsometry spectra is a non-destructive technique, with allows accurate metrology of grating profiles. Mueller ellipsometry has the advantage of being faster and cheaper than other tests currently used to in-line quality control in the microelectronics industry.

2.7.3.2 Overlay Characterization by Angle Resolved Mueller Imaging Ellipsometry

The overlay is defined as the misalignment between two layers of a stack. The influence of this error could lead to defective transistors for example if there is no electrical contact between the different constitutive layers. This feature is more and more challenging with the shrinking of the technology node (TN). If this overlay is higher than a set threshold, the whole batch cannot be processed to the new step, this results in a rework, the wafer returns to the previous lithography step and the resist is stripped. Such in the case of grating profile optical metrology, there are several techniques that are considered as a reference for the microelectronic industry. Those techniques include non-optical techniques such AFM or SEM microscopy, and optical techniques based on image analysis (pattern recognition) and on scatterometry. Image analysis also known as Advanced Image Metrology (AIM) is used in this work as reference in order to check the quality of the results obtained by angle resolved Mueller ellipsometry. Angle resolved scatterometry, with a high numerical aperture microscope objective as described above [72, 96], also constitute an interesting scatterometric tool, as it greatly facilitates measurements in extremely tiny targets (less than 5 μm wide), an increasing requirement by semiconductor manufacturers. This would be particularly true for *overlay* (default of positioning of superimposed grids at different layers), a parameter which is becoming increasingly critical and will require in-die dense sampling while current methods involve up to 8 standard (50 μm wide) targets to provide all the relevant information [97]. In the following we provide two

examples, the first one illustrates the use of spectroscopic measurements, and the second one shows the possibilities of the angle-resolved polarimeter.

It has been shown that the choice of proper azimuthal configuration for the measurements with spectroscopic polarimetry is extremely important for the overlay characterization [98, 99]. Given that the angle resolved polarimeter gives an angular signature, it is possible to use the symmetries of the grating to enhance the sensitivity of its angle-resolved signature. The sign of the off-diagonal blocks of the measured Mueller matrix changes when the azimuth φ is changed into $-\varphi$. If the profile is symmetric, the signature is invariant when $\varphi -> \varphi + 180°$ and also for the special case of $\varphi = 90°$ the previous two conditions can only be fulfilled if the off-diagonal blocks are zero. A rupture of symmetry in the structure will violate the above conditions and the off-diagonal blocks will take non-zero values for $\varphi = 90°$. Moreover, given that these blocks change sign upon a mirror symmetry, the information about the sign of the overlay can be unambiguously extracted. In order to highlight the influence of the overlay over the off-diagonal elements of the Mueller matrices the following estimator was defined: $\mathbf{E} = |\mathbf{M}| - |\mathbf{M}|^{\mathrm{T}}$ where the superscript t denotes the transposed matrix. The estimator works well either with one-dimensional or two-dimensional gratings and for different types of overlays.

For the sake of clarity we show here a simple example. It consists of the overlay of a one-dimensional grating. As depicted in Fig. 2.43, the overlay is the small shift defined along the direction perpendicular to the lines of the grating. For this particular example, overlay 25 nm, the elements of the estimator matrix $\mathbf{E}$ can reach the value of 0.25 (m14 and m41), i.e. 1/8 of the total scale, which points out the high sensitivity of this estimator.

The fact of being able to measure the full Mueller matrix is advantageous because it provides the "full picture" of the polarization effects. From this full picture, it is possible to optimize the overlay estimation sensitivity for a given type of sample, by selecting a particular matrix element (or a the combination of them) from the whole matrix. However, if a partial Mueller matrix is measured, the evident lack of matrix elements may prevent to evaluate the optimal estimators, needed to properly measure the overlay. For the particular sample discussed here, we choose to work with the estimator element E_{14} for two reasons: The first was that E_{14} showed the strongest values, thus providing the most precise results in terms of signal to noise ratio. The second reason was related to the minimization of the impact of systematic errors in the evaluation of the overlay. For Mueller measurements performed in the Fourier plane at high numerical apertures, the principal source of systematic errors came from the residual birefringence of the microscope objective used to concentrate the light on the sample. Without entering into a detailed description of these errors, it is worth to mention here that it was observed that the Mueller matrix elements which were the less affected by non-idealities of the objective were M_{14} and M_{41}. Therefore the choice of the estimator element E_{14}, which is a combination of M_{14} and M_{41}, was done in order to maximize the accuracy of the measurements. In order to check the linear relation between the values of the estimator $\mathbf{E}$ and the value of the overlay, we compared the maximum value of the element $E_{1,4}$ of the estimator

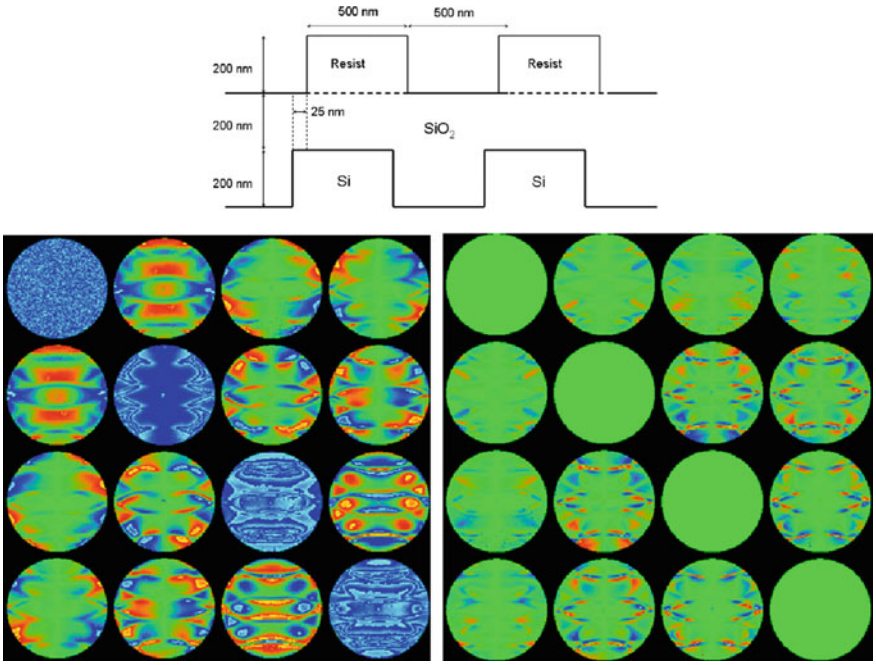

Fig. 2.43 *Top* schematic view of the grating used in the experiences for the overlay characterization. The overlay: 25 nm. *Bottom-Left* experimental angle-resolved Mueller matrix. *Bottom-Right* corresponding estimator matrix **E**. Values taken from [100] with the authorization of the author

matrix with the overlay value obtained by AIM for set of samples. The results are shown in Fig. 2.44.

The fitted linear regression, also shown in Fig. 2.44 is excellent. Moreover, the figure indicates that these results can be extended to negative overlays, the sign of the estimator becoming negative.

In conclusion, it can be said that the overlay errors can be accurately determined provided that we are able to design an apparatus with small enough errors. For this particular case, the magnitude of the systematic errors of the experimental matrices were estimated to be of the order of 1 %, which was associated to an incertitude of about 1nm in the determination of the overlay.

2.7.4 Biomedicine: Cancer Detection and Staging

The field of "optical biopsy", i.e. the diagnosis of the status of tissues by optical means, is currently a very active research area, with many techniques such as optical coherence tomography (OCT), fluorescence imaging, spectral reflectivity, imaging in coherent light (speckles), confocal imaging in vivo and many others. Polarimetric

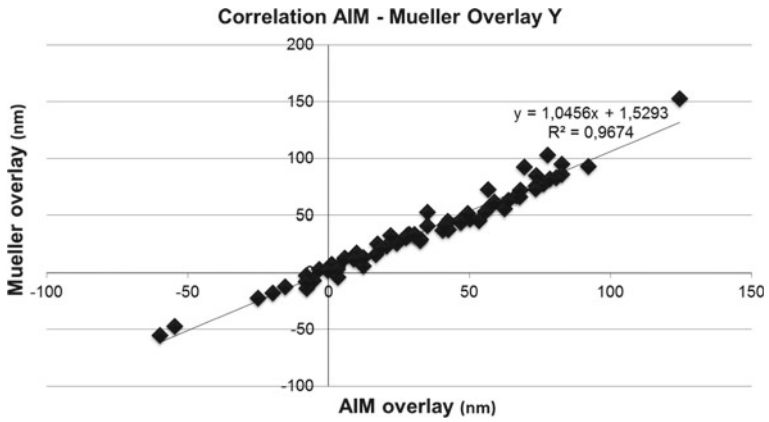

Fig. 2.44 Correlation between measured and AIM Y-overlay for 55 samples with different overlays. Values taken from [100] with the authorization of the author

imaging has received comparatively much less attention, even though it has several potential advantages for a wide use in "real world", among which its intrinsically low cost.

At LPICM we have been exploring this field for several years now, with particular attention to the early detection and staging of uterine cervix cancer. For this disease, the standard practice is as follows:

- the first "alarm" comes with anomalous Pap smear,
- then the patient is examined by a specialist with a long working distance binocular microscope, called colposcope, to give a first diagnosis form the visual aspect of the cervix, with and without staining by diluted acetic acid and iodine. The colposcopist usually takes one to three biopsies to be analyzed in a pathology department.
- If the biopsies are positive for a "precancer" state called dysplasia, the front part of the cervix is removed ("cone biopsy") and examined again by pathologists to pose the final diagnosis.

Now the colposcopic visualization of uterine dysplasias is notoriously very difficult and operator dependent. Any technique able to make this examination easier and more reliable would be welcome, provided it is not too expensive and does not imply too long examination times, which is the case for polarimetric imaging.

During a first clinical trial of a "polarimetric colposcope" which, however, did not provide full Mueller measurements, we realized that the polarimetric response of uterine cervix is much more complex than what we anticipated, and that other samples, where tumors were much easier to see, had to be studied too to get a more sound vision of the origin of the observed polarimetric contrasts. We thus focussed our activity on Mueller ellipsometric imaging of ex vivo samples, mostly colons with cancerous parts, with the instrument presented in Sect. 2.6.5.3, which was installed at the Pathology Department of Institut Mutualiste Montsouris in Paris.

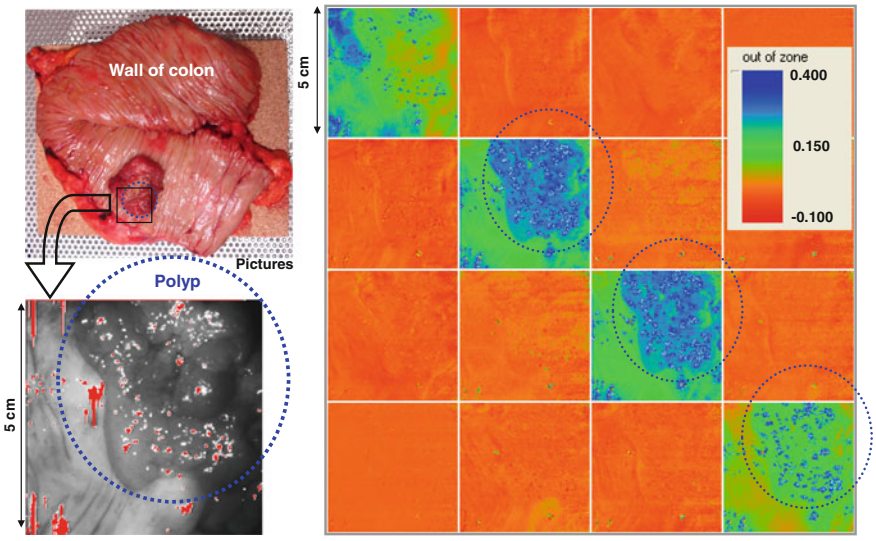

Fig. 2.45 *Left* ordinary (intensity) images of a colon sample with a burgeoning tumor. *Right* full Mueller image of the same sample, with a 5×5 field of view corresponding to the *bottom left* photo

In this contribution we cannot go beyond a short presentation of a few "emblematic" recent images, and a short discussion of the relevance of the technique for "real world" applications in this field.

2.7.4.1 Colon Samples

A first example is shown in Fig. 2.45. A colon sample with a large polyp is shown in ordinary (intensity) imaging and in full polarimetric imaging at 550 nm. The whole tissue appears as a diagonal depolarizer, with

$$M_{22} = M_{33} > M_{44} \tag{2.122}$$

as expected for a globally isotropic system observed in backscattering. Depolarization is larger for circular than for linear incident polarization, indicating that the contribution of small scatterers is dominant [101]. The key point here is that the tumoral part, at the top right of the images, is clearly *less depolarizing* than the healthy tissue.

Subsequent detailed studies [102] on similar colon samples with tumors at various stages confirmed that this trend is observed essentially at early stages of the disease, when tumoral cells exhibit an exophytic growth over normal tissues. At subsequent stages, the thickness of the tumoral tissue decreases, and the underlying layers are progressively destroyed. Then, the polarimetric responses depend on the structure of the remain tissue. However, by suitable processing of multispectral depolarization images, tumor staging by optical means seems possible.

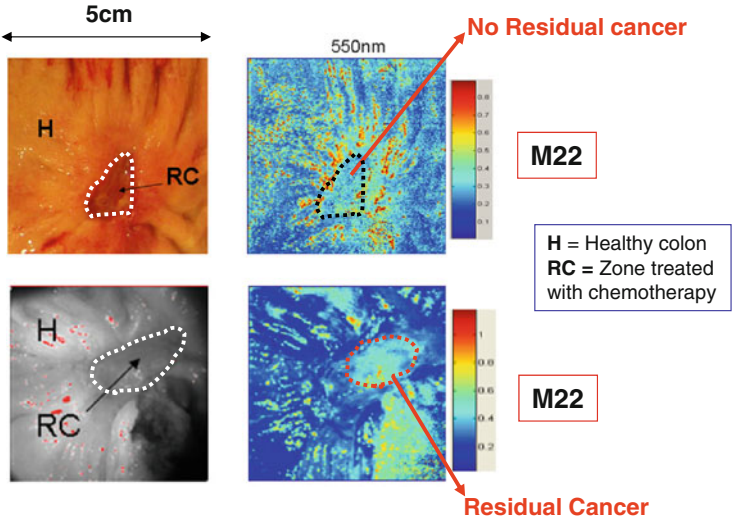

Fig. 2.46 Ordinary (*left*) and linear depolarization (*right*) images of samples of rectum extracted from two different patients after treatment by RC. The "footprint" of the initial tumor is shown on the ordinary images by *white dotted lines*. In the *bottom* images, the tissue visible in the low right corner is the section of the colon wall and should not be considered

Besides the detection and characterization of cancers at early stages, another important issue is the follow-up of treatment by radiochemotherapy (RC). For uterine cervix cancers taken at late evolution stages, RC is very efficient, and in many cases the tumor is totally "burnt" and replaced by fibrotic tissue. If so, no other treatment is actually needed. On the other hand, if some residual tumor is present after RC, it is mandatory to remove it surgically, even though this surgery, on fibrotic tissue, is much more difficult and traumatic than on non-irradiated tissues. In summary it is of paramount importance to know if residual cancer is present or not to take the right decision. Currently residual tumors are searched in CT and PetSCAN images, but none of these techniques is really satisfactory.

We took Mueller images of several rectum samples taken on patients operated after RC. Figure 2.46 shows the results for two such samples, which were subsequently analyzed by pathologists. On the ulcerated regions corresponding to the "footprint" of the initial cancer, M_{22} images reveal a lower depolarization (with respect to surrounding healthy tissue) when a residual tumor is present, while such contrasts are not visible if all the tumor has been "burnt". Of course these results are still preliminary, but they have been considered encouraging enough to start a specific project on this issue for uterine cervix.

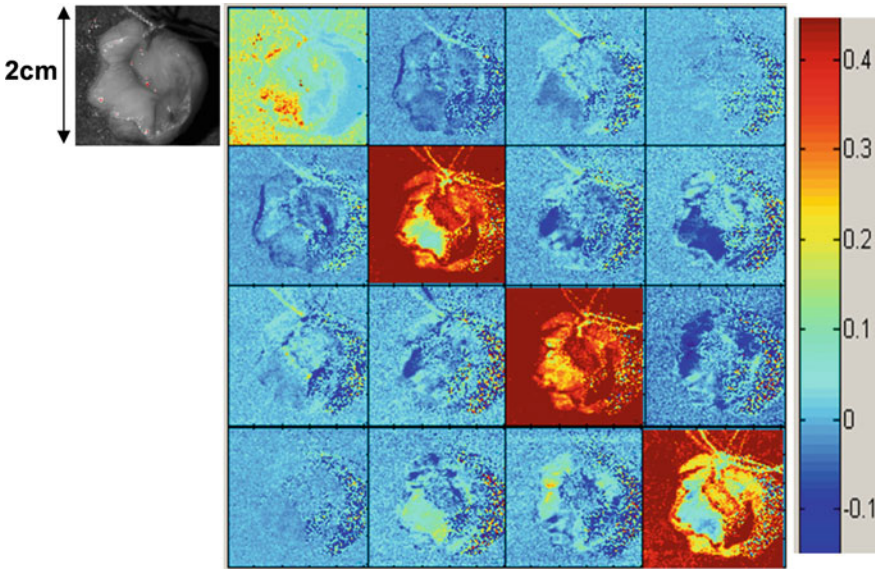

Fig. 2.47 Full Mueller matrix of a uterine cervix cone biopsy

2.7.4.2 Uterine Cervix Cone Biopsies

The colon and rectum samples always show polarimetric responses typical of pure depolarizers. Obviously, to characterize such sample full Mueller polarimetry is not needed and simpler instruments could do the job. However, this is not always so: our clinical trial on incomplete polarimetric imaging clearly showed that in vivo uterine cervix is optically anisotropic, a totally unexpected result for this kind of tissue.

Subsequently, full Mueller matrix imaging of unstained cone biopsies confirmed this very surprising result. An example of such images is shown in Fig. 2.47, where off diagonal terms are clearly quite significant. Again, a Lu–Chipman decomposition has been performed and its result has been compared with the maps of the lesions obtained by a careful (and time consuming !) pathology study of this cone biopsy. The results are shown in Fig. 2.48. The scalar birefringence is a very good marker of healthy regions. In spots where this birefringence disappears, the depolarization power becomes the best indicator of the status of the tissue: as seen previously on colon cancer at early stages, the dysplastic (precancerous) region at the center of the sample is less depolarizing than healthy tissue. Another type of tissue, with an even much lower depolarization, appears at the right bottom corner: this is not really a lesion, and it is very easily distinguished from dysplasia.

These trends have been confirmed with many other cone biopsies. It turns out that the birefringence is a very good marker of healthy regions, while in dysplastic parts the depolarization power seems rather well correlated with the stage of the disease.

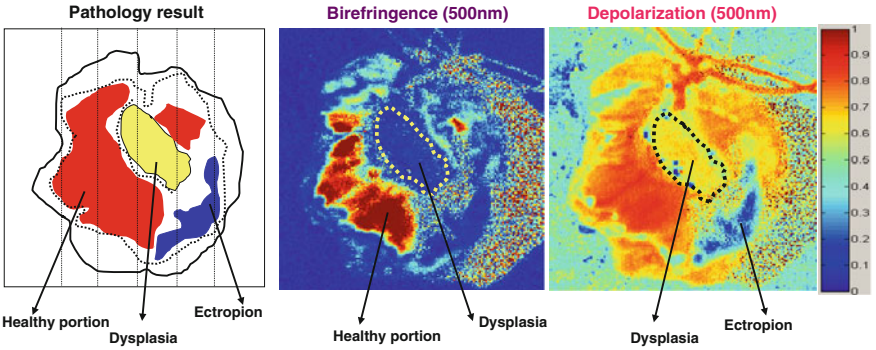

Fig. 2.48 Lu–Chipman decomposition of MM matrix of the polyp shown in Fig. 2.47

2.7.4.3 Summary and Perspectives

The results briefly reported here clearly demonstrate the potential of polarimetric imaging for optical biopsy. Though some tissues, like colon walls, behave as pure depolarizers, in other cases the polarimetric response is too rich to be exploited by incomplete polarimeters. Full Mueller imaging with subsequent image decompositions is mandatory, and can be implemented to be used not only on ex-vivo sample, but also in vivo, for clinical practice. Moreover, to really optimize the reliability of optical biopsy based on Mueller imaging, it will probably be necessary to acquire superimposable images at various wavelengths (for example with a color CCD coupled to FLCs based polarimeter) and then combine data merging and polarimetric analysis. For such an activity to succeed, the motivation of the MDs and the quality of the dialogue between physicists and physicians is crucial.

2.8 Conclusions

In this chapter we reviewed different aspects of Mueller ellipsometric instrumentation and data analysis in relation with standard ellipsometry showing the similarities but also the differences among them. We reviewed the optical formalisms currently used in the framework of standard and Mueller ellipsometry, the Jones and the Stokes formalisms. A special attention has been paid to the description of the fundamental polarization properties. These basic properties are used as "building blocks" to understand the optical response of any sample. We also discussed different ways to decompose general Mueller matrices into simple matrices taking profit of their linear algebraic properties. Mueller matrix decompositions are useful to highlight the physical properties of complex samples, such biological tissues, which cannot be easily modeled. Moreover, matrix decompositions are useful to filter depolarizing Mueller matrices, to remove noise or to isolate non-depolarizing components

which, in turn, can be treated with simple models. Matrix decompositions are powerful tools to characterize samples, but to be applied properly they need to be carried on full Mueller matrices, not on partial matrices. In order to further highlight the advantages of working with full Mueller matrices, we compared the information that can be retrieved by generalized ellipsometry and by Mueller ellipsometry. We showed that whereas for non-depolarizing samples, both, generalized and Mueller ellipsometry provide the same results, for depolarizing samples only Mueller ellipsometry is relevant. In order to disclose the technical possibilities of measuring full Mueller matrices, we reviewed the most frequently used standard ellipsometric configurations showing their characteristics including advantages and limitations. The theory allowing the design, calibration and operation of optimal Mueller polarimeters have been overviewed. We have also shown four examples of complete Mueller ellipsometers developed by us in the past years. The technical description of the Mueller ellipsometers is accompanied by some examples of applications covering topics related to materials science, optical metrology and biomedical imaging. We believe that there is an important potential for the future development of Mueller matrix-based diagnosis tools in medicine and biology. The reason for this is that tissues and living cells show an extremely complex optical behavior, which cannot be sufficiently characterized either by partial polarimetric systems, or by methods neglecting polarization properties of light. We hope to have made clear to the reader the necessity of measuring full Mueller matrices in order to properly study samples showing either depolarization or complex anisotropic response. We also hope to have brought clear and pedagogic information about the general methods and criteria that may be used to build robust and accurate Mueller ellipsometers.

Acknowledgments We would like to express our deep gratitude to the editors of this book for giving us the opportunity, (the place in terms of pages, and specially the time) that we needed to write this chapter.

Appendix 1. Mueller Matrices of Some Common Optical Retarders and Diattenuators

In the following we provide specific expressions for Mueller matrices corresponding to different types of general and fundamental optical elements.

Homogeneous Elliptic Diattenuator

The following expression corresponds to the Mueller matrix of a homogeneous elliptic diattenuator oriented with an azimuth angle θ respect to the laboratory axis.

$$\mathbf{M} = \frac{\tau_P}{2}\begin{pmatrix} 1 & C\cos 2\Psi & S\cos 2\Psi\cos(\delta) & S\cos 2\Psi\sin(\delta) \\ C\cos 2\Psi & C^2+S^2\sin 2\Psi & CS\cos(\delta)\,(1-\sin 2\Psi) & CS\sin(\delta)\,(1-\sin 2\Psi) \\ S\cos 2\Psi\cos(\delta) & CS\cos(\delta)\,(1-\sin 2\Psi) & \left(S^2+C^2\sin 2\Psi\right)\cos^2(\delta)+\sin 2\Psi\sin^2(\delta) & S^2\cos(\delta)\sin(\delta)\,(1-\sin 2\Psi) \\ S\cos 2\Psi\sin(\delta) & CS\sin(\delta)\,(1-\sin 2\Psi) & S^2\cos(\delta)\sin(\delta)\,(1-\sin 2\Psi) & \left(S^2+C^2\sin 2\Psi\right)\sin^2(\delta)+\sin 2\Psi\cos^2(\delta) \end{pmatrix} \tag{A1.1}$$

In expression (A1.1) the angles Ψ and Δ are the ellipsometric angles with its standard meaning, and the angle δ represents the ellipticity of the eigenvalues of the elliptic retarder.

The following Table A1.1 provides matrices representing some particular cases of the previous general formula corresponding to ideal circular polarizers, dichroic circular polarizers and an ideal elliptical polarizer elliptical oriented at particular angles respect to the laboratory axis.

Table A1.1 provides matrices representing some particular cases of the previous general formula corresponding to ideal linear polarizers and dichroic linear polarizers oriented at particular angles respect to the laboratory axis.

The following expression corresponds to the Mueller matrix of a homogeneous elliptic retarder oriented with an azimuth angle θ respect to the laboratory axis. The retardance provided by the system is Δ. The phase difference between the two linear components needed to build an ellipse is given by the angle φ.

$$\mathbf{M} = \frac{\tau_P}{2}\begin{pmatrix} 1 & 0 & 0 & 0 \\ 0 & d^2 - e^2 - f^2 + g^2 & 2\,(de + fg) & 2\,(df - eg) \\ 0 & 2\,(de - fg) & -d^2 + e^2 - f^2 + g^2 & 2\,(ef + dg) \\ 0 & 2\,(df + eg) & 2\,(ef - dg) & -d^2 - e^2 + f^2 + g^2 \end{pmatrix} \tag{A1.2}$$

$$d = \cos(2\theta)\sin\left(\frac{\Delta}{2}\right);\ e = \sin(2\theta)\sin\left(\frac{\Delta}{2}\right)\cos(\varphi);$$
$$f = \sin(2\theta)\sin\left(\frac{\Delta}{2}\right)\sin(\varphi);\ g = \cos\left(\frac{\Delta}{2}\right)$$

Table A1.2 provides Mueller matrices representing some particular cases of the previous general formula corresponding to circular retarders and linear retarders oriented at particular angles respect to the x–y reference coordinate axis.

Appendix 2. Differential Matrices of Fundamental Polarimetric Properties

In this appendix we provide a detailed expression of the differential matrices corresponding to the eight fundamental polarimetric properties, written according to the 4 × 4 Stokes formalism and the 2 × 2 Jones formalism. We also provide the way to deduce them from the original Mueller or Stokes matrices.

Mueller matrix of an homogeneous elliptic retarder

According to [26, 27] the differential matrix **m** of a given Mueller matrix **M** is a 4 × 4 matrix containing simple expressions of the fundamental polarimetric properties: isotropic refraction, φ isotropic absorption, α, linear birefringence along the coordinate axis x–y, η, linear dichroism along the coordinate x–y, β, linear bire-

Table A1.1 In the table there are summarized the eigenvectors, the Jones matrices, the Mueller matrices and the vector diattenuation for some particular cases of the general expression (A1.1)

Optical element	Eigenvectors	Jones matrix	Mueller matrix	Vector diattenuation
Right circular polarizer ideal	$\frac{1}{\sqrt{2}}\begin{pmatrix}1\\ i\end{pmatrix}$ $\frac{1}{\sqrt{2}}\begin{pmatrix}i\\ 1\end{pmatrix}$	$\sqrt{\tau_p}\begin{pmatrix}1 & -i\\ i & 1\end{pmatrix}$	$\frac{\tau_P}{2}\begin{pmatrix}1&0&0&1\\0&0&0&0\\0&0&0&0\\1&0&0&1\end{pmatrix}$	$\begin{pmatrix}0\\0\\1\end{pmatrix}$
Left polarizer ideal	$\frac{1}{\sqrt{2}}\begin{pmatrix}1\\ i\end{pmatrix}$ $\frac{1}{\sqrt{2}}\begin{pmatrix}i\\ 1\end{pmatrix}$	$\sqrt{\tau_p}\begin{pmatrix}1 & i\\ -i & 1\end{pmatrix}$	$\frac{\tau_P}{2}\begin{pmatrix}1&0&0&-1\\0&0&0&0\\0&0&0&0\\-1&0&0&1\end{pmatrix}$	$\begin{pmatrix}0\\0\\-1\end{pmatrix}$
Dichroic circular polarizer	$\frac{1}{\sqrt{2}}\begin{pmatrix}1\\ 1\end{pmatrix}$ $\frac{1}{\sqrt{2}}\begin{pmatrix}1\\ -1\end{pmatrix}$	$z\begin{pmatrix}1 & -i\cos(2\Psi)\\ i\cos(2\Psi) & 1\end{pmatrix}$ $z=\frac{\sqrt{\tau_{\max}}+\sqrt{\tau_{\min}}}{2}$	$\frac{q_1}{2}\begin{pmatrix}1&0&0&q_2\\0&q_3&0&0\\0&0&q_3&0\\q_2&0&0&1\end{pmatrix}$ $q_1=\tau_{\max}+\tau_{\min}$; $q_2=\cos(2\Psi)$; $q_3=\sin(2\Psi)$	$q_2\begin{pmatrix}0\\0\\-1\end{pmatrix}$

(continued)

Table A1.1 (continued)

Optical element	Eigenvectors	Jones matrix	Mueller matrix	Vector diattenuation
Dichroic elliptical polarizer	$\begin{pmatrix} \cos(\theta) \\ \sin(\theta)\, e^{i\varphi} \end{pmatrix}$	$\frac{\sqrt{\tau_{\max}}}{2} \begin{pmatrix} c^2 & cse^{-i\varphi} \\ cse^{i\varphi} & s^2 \end{pmatrix}$ $c = \cos(\theta);\ s = \sin(\theta)$	$\frac{\tau_{\max}}{2} \begin{pmatrix} 1 & C & SX & SY \\ C & C^2 & CSX & CSY \\ SX & CSX & (SX)^2 & SXSY \\ SY & CSY & SXSY & (SY)^2 \end{pmatrix}$ $C = \cos(2\theta)\ ;\ SX = \sin(2\theta)\cos(\varphi)$ $SY = \sin(2\theta)\sin(\varphi)$	$\begin{pmatrix} C \\ SX \\ SY \end{pmatrix}$
Orientation θ	$\begin{pmatrix} -\sin(\theta)\, e^{-i\varphi} \\ \cos(\theta) \end{pmatrix}$			

The cases correspond to elliptical ideal and elliptical dichroic polarizers oriented at particular angles, θ, respect to the x–y reference coordinate frame. The selected cases are representative of elements commonly used in practical optical settings. In this table the values of τ_{max} and τ_{min} correspond to the maximum and minimum transmission of the dichroic polarizer. For an ideal polarizer τ_{min} is null and τ_{max} is equal to the total transmission of the element τ_P. The angle φ is the phase difference between the two linear orthogonal components needed to build an elliptic state. The symbols C, SX, SY and q_2 used in the expressions of the vector diattenuation are the same that these used in the corresponding Mueller matrices

Table A1.2 List of the eigenvectors, the Jones matrices, the Mueller matrices and the vector diattenuation for some particular cases of the general expression (A1.1)

Optical element	Eigenvectors	Jones matrix	Mueller matrix	Vector diatten-uation
Linear polarizer	$\begin{pmatrix}1\\0\end{pmatrix}$	$\sqrt{\tau_p}\begin{pmatrix}1&0\\0&0\end{pmatrix}$	$\frac{\tau_p}{2}\begin{pmatrix}1&1&0&0\\1&1&0&0\\0&0&0&0\\0&0&0&0\end{pmatrix}$	$\begin{pmatrix}1\\0\\0\end{pmatrix}$
Orientation $\theta = 0°$	$\begin{pmatrix}0\\1\end{pmatrix}$		$C = \cos(2\theta) = 1\ ;\ S = \sin(2\theta) = 0$	
Linear polarizer	$\begin{pmatrix}1\\0\end{pmatrix}$	$\sqrt{\tau_p}\begin{pmatrix}0&0\\0&1\end{pmatrix}$	$\frac{\tau_p}{2}\begin{pmatrix}1&-1&0&0\\-1&1&0&0\\0&0&0&0\\0&0&0&0\end{pmatrix}$	$\begin{pmatrix}-1\\0\\0\end{pmatrix}$
Orientation $\theta = 90°$	$\begin{pmatrix}0\\1\end{pmatrix}$		$C = \cos(2\theta) = -1\ ;\ S = \sin(2\theta) = 0$	
Linear polarizer	$\frac{1}{\sqrt{2}}\begin{pmatrix}1\\1\end{pmatrix}$	$\frac{\sqrt{\tau_p}}{2}\begin{pmatrix}1&1\\1&1\end{pmatrix}$	$\frac{\tau_p}{2}\begin{pmatrix}1&0&1&0\\0&0&0&0\\1&0&1&0\\0&0&0&0\end{pmatrix}$	$\begin{pmatrix}-1\\0\\0\end{pmatrix}$
Orientation $\theta = 45°$	$\frac{1}{\sqrt{2}}\begin{pmatrix}1\\-1\end{pmatrix}$		$C = \cos(2\theta) = 0\ ;\ S = \sin(2\theta) = 1$	

(continued)

Table A1.2 (continued)

Optical element	Eigenvectors	Jones matrix	Mueller matrix	Vector diatten-uation
Linear polarizer	$\begin{pmatrix}\cos(\theta)\\ \sin(\theta)\end{pmatrix}$	$\sqrt{\tau_p}\begin{pmatrix}c^2 & cs\\ cs & s^2\end{pmatrix}$ $c=\cos(\theta)\ ;\ s=\sin(\theta)$	$\frac{\tau_P}{2}\begin{pmatrix}1 & C & S & 0\\ C & C^2 & CS & 0\\ S & CS & S^2 & 0\\ 0 & 0 & 0 & 0\end{pmatrix}$	$\begin{pmatrix}C\\ S\\ 0\end{pmatrix}$
Orientation θ	$\begin{pmatrix}-\sin(\theta)\\ \cos(\theta)\end{pmatrix}$		$C=\cos(2\theta)\ ;\ S=\sin(2\theta)$	
Dichroic linear polarizer	$\begin{pmatrix}\cos(\theta)\\ \sin(\theta)\end{pmatrix}$	$\begin{pmatrix}\sqrt{\tau_{\max}}c^2 & zcs\\ zcs & \sqrt{\tau_{\min}}s^2\end{pmatrix}$ $c=\cos(\theta)\ ;\ s=\sin(\theta)\,;$ $z=\ \sqrt{\tau_{\max}}-\sqrt{\tau_{\min}}$	$\frac{q_1}{2}\begin{pmatrix}1 & Cq_2 & Sq_2 & 0\\ Cq_2 & C^2+S^2q_3 & CS(1-q_3) & 0\\ Sq_2 & CS(1-q_3) & S^2+C^2q_3 & 0\\ 0 & 0 & 0 & 0\end{pmatrix}$ $q_1=\tau_{\max}+\tau_{\min};\ q_2=\cos(2\Psi)$ $q_3=\sin(2\Psi);\ C=\cos(2\theta)\ ;\ S=\sin(2\theta)$	$q_2\begin{pmatrix}C\\ S\\ 0\end{pmatrix}$
Orientation θ	$\begin{pmatrix}-\sin(\theta)\\ \cos(\theta)\end{pmatrix}$			

These cases correspond to linear ideal and linear dichroic polarizers oriented at particular angles, θ, respect to the x–y reference coordinate frame. They are selected because they represent the optical behavior of optical elements commonly encountered in practical situations. The values of τ_{max} and τ_{min} correspond to the maximum and minimum transmission of the dichroic polarizer. For an ideal polarizer τ_{min} is null and τ_{max} is equal to the total transmission of the element τ_P. The symbols C, S and q_2 used in the expressions of the vector diattenuation are the same that these used in the corresponding Mueller matrices

Table A2.1 This table summarizes the eigenvalues, the Jones matrices, the Mueller matrices and the vector retardances corresponding to some particular cases of the general expression (A1.2)

Optical element	Eigenvectors	Jones matrix	Mueller matrix	Vector diatten-uation R
Linear birefringent	$\begin{pmatrix}1\\0\end{pmatrix}$	$\begin{pmatrix}e^{i\frac{\Delta}{2}} & 0\\ 0 & e^{-i\frac{\Delta}{2}}\end{pmatrix}$	$\begin{pmatrix}1&0&0&0\\0&1&0&0\\0&0&\cos(\Delta)&\sin(\Delta)\\0&0&-\sin(\Delta)&\cos(\Delta)\end{pmatrix}$	$\Delta\begin{pmatrix}1\\0\\0\end{pmatrix}$
Retarder	$\begin{pmatrix}0\\1\end{pmatrix}$			
Linear birefringent	$\begin{pmatrix}1\\0\end{pmatrix}$	$\begin{pmatrix}\cos\left(\frac{\Delta}{2}\right) & i\sin\left(\frac{\Delta}{2}\right)\\ i\sin\left(\frac{\Delta}{2}\right) & \cos\left(\frac{\Delta}{2}\right)\end{pmatrix}$	$\begin{pmatrix}1&0&0&0\\0&\cos(\Delta)&0&-\sin(\Delta)\\0&0&1&0\\0&\sin(\Delta)&0&\cos(\Delta)\end{pmatrix}$	$\Delta\begin{pmatrix}0\\1\\0\end{pmatrix}$
Retarder orientation $\theta = 45°$	$\frac{1}{\sqrt{2}}\begin{pmatrix}-1\\1\end{pmatrix}$			
Linear birefringent	$\begin{pmatrix}\cos(\theta)\\ \sin(\theta)\end{pmatrix}$	$\begin{pmatrix}c^2ep+s^2em & i\sin\frac{\Delta}{2}\sin 2\theta\\ i\sin\frac{\Delta}{2}\sin 2\theta & s^2ep+c^2em\end{pmatrix}$ $c=\cos(\theta);\ s=\sin(\theta);$ $ep=e^{i\Delta/2};\ em=e^{-i\Delta/2}$	$\begin{pmatrix}1&0&0&0\\0&C^2+S^2X&CS(1-X)&-SY\\0&CS(1-X)&S^2+C^2X&CY\\0&SY&-CY&X\end{pmatrix}$ $C=\cos(2\theta)\ ;\ S=\sin(2\theta)$ $X=\cos(\Delta)\ Y=\sin(\Delta)$	$\Delta\begin{pmatrix}C\\S\\0\end{pmatrix}$
Retarder orientation θ	$\begin{pmatrix}-\sin(\theta)\\ \cos(\theta)\end{pmatrix}$			

(continued)

Table A2.1 (continued)

Optical element	Eigenvectors	Jones matrix	Mueller matrix	Vector diatten-uation R
Circular birefrin-gent	$\frac{1}{\sqrt{2}}\begin{pmatrix}1\\ i\end{pmatrix}$	$\begin{pmatrix}\cos\left(\frac{\Delta}{2}\right) & \sin\left(\frac{\Delta}{2}\right)\\ -\sin\left(\frac{\Delta}{2}\right) & \cos\left(\frac{\Delta}{2}\right)\end{pmatrix}$	$\begin{pmatrix}1 & 0 & 0 & 0\\ 0 & \cos(\Delta) & \sin(\Delta) & 0\\ 0 & -\sin(\Delta) & \cos(\Delta) & 0\\ 0 & 0 & 0 & 1\end{pmatrix}$	$\Delta\begin{pmatrix}0\\ 0\\ 1\end{pmatrix}$
Retarder right	$\frac{1}{\sqrt{2}}\begin{pmatrix}i\\ 1\end{pmatrix}$			
Circular birefrin-gent	$\frac{1}{\sqrt{2}}\begin{pmatrix}1\\ i\end{pmatrix}$	$\begin{pmatrix}\cos\left(\frac{\Delta}{2}\right) & -\sin\left(\frac{\Delta}{2}\right)\\ \sin\left(\frac{\Delta}{2}\right) & \cos\left(\frac{\Delta}{2}\right)\end{pmatrix}$	$\begin{pmatrix}1 & 0 & 0 & 0\\ 0 & \cos(\Delta) & -\sin(\Delta) & 0\\ 0 & \sin(\Delta) & \cos(\Delta) & 0\\ 0 & 0 & 0 & 1\end{pmatrix}$	$\Delta\begin{pmatrix}0\\ 0\\ -1\end{pmatrix}$
Retarder left	$\frac{1}{\sqrt{2}}\begin{pmatrix}i\\ 1\end{pmatrix}$			

The listed cases correspond to circular retarders and linear retarders oriented at a particular angle, θ, respect to the x–y reference coordinate axis. The symbols C, S and Δ used in the expressions of the vector retardances are the same that these used in the corresponding Mueller matrices

fringence along the bisectors to the coordinate axis x–y, η, linear dichroism along the bisectors to the coordinate axis x–y, γ, circular birefringence, μ, and circular dichroism, δ. The bisectors to the coordinate axis x–y form a coordinate axes rotated 45° respect to the x–y. A particular choice of the x–y axis well adapted for ellipsometric measurements in reflection, or in transmission with tilted samples, is the p-s axis defined respect to the plane of incidence. When light propagates along the z direction in an anisotropic medium, which is considered as homogeneous in the x, y directions, the transformation of the Stokes vector at a given position z, S(z) to a Stokes vector at a given position S(z + Δz) can be described by the Mueller matrix $\mathbf{M_{z,\Delta z}}$. The transformation can be written according to the following expression:

$$\mathbf{S}(z+\Delta z) = \mathbf{M_{z,\Delta z}}\mathbf{S}(z) \tag{A2.1}$$

Subtraction of S(z) from both sides of expression (A2.1) leads to:

$$\mathbf{S}(z+\Delta z) - \mathbf{S}(z) = \mathbf{S}(z)\left(\mathbf{M_{z,\Delta z}} - \mathbf{I}\right) \tag{A2.2}$$

where $\mathbf{I}$ is the identity matrix. Clearly, if the latter expression is divided by Δz and then the it is extrapolated to the limiting case of $\Delta z \to 0$, then it is possible to obtain the following expression relating the transformation of the Stokes vector:

$$\frac{d\mathbf{S}}{dz} = \lim_{\Delta z \to 0} \frac{\left(\mathbf{M_{z,\Delta z}} - \mathbf{I}\right)}{\Delta z}\mathbf{S}(z) = \mathbf{m}\mathbf{S}(z) \tag{A2.3}$$

The latter equation is the definition of the matrix $\mathbf{m}$ in the 4×4 Stokes formalism. The derivation of expression (A2.3) is valid for either a non-depolarizing or a depolarizing medium. The matrix $\mathbf{m}$ is the expression of the effect of the different optical properties of the medium on the Stokes vector when light travels a differential distance Δz. For this reason the matrix $\mathbf{m}$ is called the differential propagation matrix, or simply the differential matrix.

The relation of (A2.3) with the expression (2.52) given in the text is easily found. The transformation of an initial Stokes vector $\mathbf{S}(0)$ of a beam traveling a distance z inside a medium can be written as:

$$\mathbf{S}(z) = \mathbf{M_z}\mathbf{S}(0) \tag{A2.4}$$

After differentiating the previous expression respect to z one gets:

$$\frac{d\mathbf{S}}{dz} = \frac{d\mathbf{M_z}}{dz}\mathbf{S}(0) \tag{A2.5}$$

According to (A2.3) the latter expression can be rewritten as:

$$\frac{d\mathbf{S}}{dz} = \mathbf{m}\mathbf{S}(z) = \mathbf{m}\mathbf{M_z}\mathbf{S}(0) = \frac{d\mathbf{M_z}}{dz}\mathbf{S}(0) \tag{A2.6}$$

Table A2.2 Differential matrices m and n corresponding to the eight fundamental polarimetric properties

Optical property	Differential **m**	Differential **n**
Isotropic refraction	$\begin{pmatrix} 0 & 0 & 0 & 0 \\ 0 & 0 & 0 & 0 \\ 0 & 0 & 0 & 0 \\ 0 & 0 & 0 & 0 \end{pmatrix}$	$\frac{\varphi}{2}\begin{pmatrix} i & 0 \\ 0 & i \end{pmatrix}$
Isotropic absorption	$\begin{pmatrix} \alpha & 0 & 0 & 0 \\ 0 & \alpha & 0 & 0 \\ 0 & 0 & \alpha & 0 \\ 0 & 0 & 0 & \alpha \end{pmatrix}$	$\frac{\alpha}{2}\begin{pmatrix} 1 & 0 \\ 0 & 1 \end{pmatrix}$
Linear birefringence along x–y	$\begin{pmatrix} 0 & 0 & 0 & 0 \\ 0 & 0 & 0 & 0 \\ 0 & 0 & 0 & \eta \\ 0 & 0 & -\eta & 0 \end{pmatrix}$	$\frac{\eta}{2}\begin{pmatrix} i & 0 \\ 0 & -i \end{pmatrix}$
Linear dichroism along x–y	$\begin{pmatrix} 0 & \beta & 0 & 0 \\ \beta & 0 & 0 & 0 \\ 0 & 0 & 0 & 0 \\ 0 & 0 & 0 & 0 \end{pmatrix}$	$\frac{\beta}{2}\begin{pmatrix} 1 & 0 \\ 0 & -1 \end{pmatrix}$
Linear birefringence along bisectors of x–y	$\begin{pmatrix} 0 & 0 & 0 & 0 \\ 0 & 0 & 0 & \nu \\ 0 & 0 & 0 & 0 \\ 0 & -\nu & 0 & 0 \end{pmatrix}$	$\frac{-\nu}{2}\begin{pmatrix} 0 & i \\ i & 0 \end{pmatrix}$
Linear dichroism along bisectors of x–y	$\begin{pmatrix} 0 & 0 & \gamma & 0 \\ 0 & 0 & 0 & 0 \\ \gamma & 0 & 0 & 0 \\ 0 & 0 & 0 & 0 \end{pmatrix}$	$\frac{\gamma}{2}\begin{pmatrix} 0 & 1 \\ 1 & 0 \end{pmatrix}$
Circular birefringence (right)	$\begin{pmatrix} 0 & 0 & 0 & 0 \\ 0 & 0 & \mu & 0 \\ 0 & -\mu & 0 & 0 \\ 0 & 0 & 0 & 0 \end{pmatrix}$	$-\frac{\mu}{2}\begin{pmatrix} 0 & -1 \\ 1 & 0 \end{pmatrix}$
Circular dichroism (right)	$\begin{pmatrix} 0 & 0 & 0 & \delta \\ 0 & 0 & 0 & 0 \\ 0 & 0 & 0 & 0 \\ \delta & 0 & 0 & 0 \end{pmatrix}$	$\frac{\delta}{2}\begin{pmatrix} 0 & -i \\ i & 0 \end{pmatrix}$

Thus giving an analogous definition of the matrix **m** which is identical to (2.52):

$$\mathbf{M_z}^{-1}\frac{d\mathbf{M_z}}{dz} = \mathbf{m} \tag{A2.7}$$

An analogous procedure may be performed using Jones vectors instead of Stokes vectors leading to the derivation of a 2×2 matrix called **n**. Obviously the applicability of matrix **n** is restricted to non-depolarizing media.

As an illustration, of the method to obtain the expression of the differential matrices **m** and **n**, let's consider their detailed derivation for the particular case of a homogeneous medium along the propagation direction, of total thickness z, showing linear birefringence characterized by the parameter η. The respective Mueller and Jones matrices associated to this medium are:

$$\mathbf{M} = \begin{pmatrix} 1 & 0 & 0 & 0 \\ 0 & 1 & 0 & 0 \\ 0 & 0 & \cos(\eta z) & \sin(\eta z) \\ 0 & 0 & -\sin(\eta z) & \cos(\eta z) \end{pmatrix} \quad \text{and} \quad \mathbf{J} = \begin{pmatrix} e^{i\frac{\eta}{2}z} & 0 \\ 0 & e^{-i\frac{\eta}{2}z} \end{pmatrix} \quad \text{where} \quad \eta = \frac{4\pi\, birr}{\lambda} \tag{A2.8}$$

The total retardance created by the medium, commonly expressed by the ellipsometric angle Δ is given by η times the thickness z. The parameter η is the intensive retardance, also called the differential retardance, whereas Δ is the extensive retardance, which is proportional to the path that light has travelled inside the medium. The differential retardance depends of the wavelength of light, λ, and the birefringence of the medium, *birr*.

For a thin section of thickness Δz of the material, the corresponding Jones and Mueller matrices can be calculated expanding the terms of matrices in (A2.8) in a Taylor series expansion respect to z and retaining only the first order terms.

$$\mathbf{M_{\Delta z}} = \begin{pmatrix} 1 & 0 & 0 & 0 \\ 0 & 1 & 0 & 0 \\ 0 & 0 & 1 & \eta z \\ 0 & 0 & -\eta z & 1 \end{pmatrix} \quad \text{and} \quad \mathbf{J_{\Delta z}} = \begin{pmatrix} 1 + \frac{i\eta z}{2} & 0 \\ 0 & 1 - \frac{i\eta z}{2} \end{pmatrix} \tag{A2.9}$$

Then according to (A2.3) after subtraction of the respective (2 × 2) and (4 × 4) unit matrices and division by z, one gets:

$$\mathbf{m} = \begin{pmatrix} 0 & 0 & 0 & 0 \\ 0 & 0 & 0 & 0 \\ 0 & 0 & 0 & \eta \\ 0 & 0 & -\eta & 0 \end{pmatrix} \quad \text{and} \quad \mathbf{n} = \frac{\eta}{2} \begin{pmatrix} i & 0 \\ 0 & -i \end{pmatrix} \tag{A2.10}$$

The matrices (4 × 4) and (2 × 2) **m** and **n** matrices grouped in Table A2.2 the following table are the result of applying the same procedure to each one of the eight fundamental properties:

References

1. R.M.A Azzam, N.M. Bashara, Ellipsometry and Polarized Light (Elsevier, Amsterdam, 1987)
2. H.G. Tompkins, W.A. McGahan, *Spectroscopic Ellipsometry and Reflectometry A User's Guide* (Wiley, New York, 1999)

3. H. Fujiwara, *Spectroscopic Ellipsometry: Principles and Applications* (Wiley, West Sussex, 2007)
4. M. Born, E. Wolf, *Principles of Optics* (Cambridge University Press, Cambridge, 2005)
5. S. Huard, *The Polarization of Light* (Wiley, New York, 1997)
6. R.A. Chipman, Polarimetry, in: Handbook of Optics, vol 2, chap 22, 2nd ed. M. Bass ed. (McGraw Hill, New York, 1995)
7. D. Goldstein, *Polarized Light*, 2nd edn. (Decker, New York, 2003)
8. J.J. Gil, Characteristic properties of Mueller matrices. J. Opt. Soc. Am. **17**, 328–334 (2000). doi:10.1364/JOSAA.17.000328
9. S.R. Cloude, Group theory and polarisation algebra. Optik **75**, 26 (1986). doi:10.1364/JOSAA.18.003130
10. D.G.M. Anderson, R. Barakat, Necessary and sufficient conditions for a Mueller matrix to be derivable from a Jones matrix. J. Opt. Soc. Am. A **11**, 2305 (1994). doi:10.1364/JOSAA.11.002305
11. J.J. Gil, E. Bernabeu, A depolarization criterion in Mueller matrices. Opt. Acta **32**, 259 (1985). doi:10.1080/713821732
12. S.Y. Lu, R.A. Chipman, Interpretation of Mueller matrices based on polar decomposition. J. Opt. Soc. Am. A **13**, 1106–1113 (1996). doi:10.1364/JOSAA.13.001106
13. R. Ossikovski, Alternative depolarization criteria for Mueller matrices. J. Opt. Soc. Am. A **27**, 808–814 (2010). doi:10.1364/JOSAA.27.000808
14. R. Espinosa-Luna, G. Atondo-Rubio, E. Bernabeu, S. Hinijosa-Ruiz, Dealing depolarization of light in Mueller matrices with scalar metrics Â'. Optik **121**, 1058–1068 (2010). doi:10.1016/j.ijleo.2008.12.030
15. S.R. Cloude, E. Pottier, IEEE Trans. GRS **34**, 498 (1996)
16. S.R. Cloude, Conditions for the physical realizability of matrix operators in polarimetry. Proc. SPIE **1166**, 177–185 (1989)
17. F. Le Roy-Bréhonnet, B. Le Jeune, Utilization of Mueller matrix formalism to obtain optical targets depolarization and polarization properties. Prog. Quantum Electron. **21**, 109–151 (1997). doi:10.1016/S0079-6727(97)84687-3
18. J. Morio, F. Goudail, Influence of the order of diattenuator, retarder, and polarizer in polar decomposition of Mueller matrices. Optics. Lett. **29**, 2234–2236 (2004). doi:10.1364/OL.29.002234
19. R. Ossikovski, A. De Martino, S. Guyot, Forward and reverse product decompositions of depolarizing Mueller matrices. Opt. Lett. **32**, 689 (2007)
20. R. Ossikovski, Interpretation of nondepolarizing Mueller matrices based on singular-value decomposition. J. Opt. Soc. Am. A **25**, 473–482 (2008). doi:JOSAA.25.000473
21. R. Ossikovski, E. Garcia-Caurel, A. De Martino, Product decompositions of experimentally determined non-depolarizing Mueller matrices. Physica status solidi C (2008). doi:10.1002/pssc.200777794
22. R. Ossikovski, Analysis of depolarizing Mueller matrices through a symmetric decomposition. J. Opt. Soc. Am. A **26**, 1109–1118 (2009)
23. C. Fallet, A. Pierangelo, R. Ossikovski, A. De Martino, Experimental validation of the symmetric decomposition of Mueller matrices. Opt. Express. **18**, 2832 (2009). doi:10.1364/OE.18.000831
24. R. Ossikovski, C. Fallet, A. Pierangelo, A. De Martino, Experimental implementation and properties of Stokes nondiagonalizable depolarizing Mueller matrices. Opt. Lett. **34**, 974 (2009)
25. R. Ossikovski, M. Foldyna, C. Fallet, A. De Martino, Experimental evidence for naturally occurring nondiagonal depolarizers. Opt. Lett. **34**, 2426–2428 (2009). doi:10.1364/OL.34.002426
26. R. Ossikovski, Differential matrix formalism for depolarizing anisotropic media. Opt. Lett. **36**, 2330–2332 (2011). doi:10.1364/OL.36.002330
27. R.M.A. Azzam, Propagation of partially polarized light through anisotropic media with or without depolarization: a differential 4×4 matrix calculus. J. Opt. Soc. Am. **68**, 1756–1767 (1978). doi:10.1364/JOSA.68.001756

28. M. Anastasiadou, S. Ben-Hatit, R. Ossikovski, S. Guyot, A. De Martino, Experimental validation of the reverse polar decomposition of depolarizing Mueller matrices. J. Eur. Opt. Soc. Rapid Publ. **2**, 1–7 (2007). doi:10.2971/jeos.2007.07018
29. M. Gaillet, D. Cattelan, G. Bruno, M. Losurdo, Roadmap on industrial needs in ellipsometry and specifications for the next generation of ellipsometry and polarimetry. NanocharM Report 2009, www.nanocharm.org
30. G.E. Jellison Jr., Data analysis for spectroscopic ellipsometry. Thin Solid Films **234**, 416–422 (1993). doi:10.1016/0040-6090(93)90298-4
31. G.E. Jellison Jr., The calculation of thin film parameters from spectroscopic ellipsometry data. Thin Solid Films **290–291**, 40–45 (1996). doi:0.1016/S0040-6090(96)09009-8
32. P.S. Hauge, Recent developments in instrumentation in ellipsometry. Surf. Sci. **96**, 108–140 (1980). doi:10.1016/0039-6028(80)90297-6
33. D. Thomson, B. Johs, Infrared ellipsometer/polarimeter system, method of calibration and use thereof, US patent No: US5706212, (1998)
34. A. Laskarakis, S. Logothetidis, E. Pavlopoulou, M. Gioti, Mueller matrix spectroscopic ellipsometry: formulation and application. Thin Solid Films **455–456**, 43–49 (2004). doi:10.1016/j.tsf2003.11.197
35. E. Compain, S. Poirier, B. Drévillon, General and self-consistent method for the calibration of polarization modulators, polarimeters, and Mueller-matrix ellipsometers. Appl. Opt. **38**, 3490–3502 (1999). doi:10.1364/AO.38.003490
36. D.S. Sabatke, A.M. Locke, M.R. Descour, W.C. Sweatt, Figures of merit for complete Stokes polarimeters. Proc. SPIE **4133**, 75–81 (2000). doi:10.1117/12.406613
37. J.S. Tyo, Noise equalization in Stokes parameter images obtained by use of variable-retardance polarimeters. Opt. Lett. **25**, 1198–2000 (2000). doi:10.1364/OL.25.001198
38. J.S. Tyo, Design of optimal polarimeters : maximization of signal-to-noise ratio and minimization of systematic error. Appl. Opt. **41**, 619–630 (2002). doi:10.1364/AO.41.000619
39. D.S. Sabatke, M.R. Descour, E.L. Dereniak, W.C. Sweatt, S.A. Kemme, G.S. Phipps, Optimization of retardance for a complete Stokes polarimeter. Opt. Lett. **25**, 802 (2000). doi:10.1364/OL.25.000802
40. J. Zallat, S. Aïnouz, M.P. Stoll, Optimal configurations for imaging polarimeters: impact of image noise and systematic errors. J. Opt. A Pure Appl. Opt. **8**, 807 (2006). doi:10.1088/1464-4258/8/9/015
41. M.H. Smith, Optimisation of a dual-rotating-retarder Mueller matrix polarimeter. Appl. Opt. **41**, 2488 (2002). doi:10.1364/AO.41.002488
42. R.W. Collins, J. Koh, Dual rotating-compensator multichannel ellipsometer: instrument design for real-time Mueller matrix spectroscopy of surfaces and films. JOSA A. **16**, 1997–2006 (1999). doi:10.1364/JOSAA.16.001997
43. E. Compain, B. Drévillon, High-frequency modulation of the four states of polarization of light with a single phase modulator. Rev. Sci. Instrum. **69**, 1574 (1998). doi:/10.1063/1.1148811
44. E. Compain, B. Drévillon, Broadband division-of-amplitude polarimeter based on uncoated prisms. Appl. Opt. **37**, 5938 (1998). doi:10.1364/AO.37.005938
45. E. Compain, B. Drévillon, J. Huc, J.Y. Parey, J.E. Bouree, Complete Mueller matrix measurement with a single high frequency modulation. Thin Solid Films **313–314**, 47–52 (1998). doi:10.1016/S0040-6090(97)00767-0
46. D. Lara, C. Dainty, Double-pass axially resolved confocal Mueller matrix imaging polarimetry. Opt. Lett. **30**, 2879–2881 (2005). doi:10.1364/OL.30.002879
47. See for instance the official website of Woollam Co. www.jawoollam.com
48. G.E. Jellison, F.A. Modine, Two-modulator generalized ellipsometry: experiment and callibration. Appl. Opt. **36**, 8184–8189 (1997). doi:10.1364/AO.36.008184
49. O. Arteaga, J. Freudenthal, B. Wang, B. Kahr, Mueller matrix polarimetry with four photoelastic modulators: theory and calibration, to be published in, Applied Optics (2012)
50. A.E. Oxley, On apparatus for the production of circularly polarized light. Philos. Mag. **21**, 517–532 (1911). doi:10.1080/14786440408637058
51. See for instance the official website of Meadowlark Optics, www.meadowlark.com

52. J. Ladstein, F. Stabo-Eeg, E. Garcia-Caurel, M. Kildemo, Fast near-infra-red spectroscopic Mueller matrix ellipsometer based on ferroelectric liquid crystal retarders. Physica Status Solidi C, Special Issue: 4th International Conference on Spectroscopic Ellipsometry, 5, n/a, doi:10.1002/pssc.200890005
53. P.A. Letnes, I.S. Nerbo, L.M.S. Ass, P.G. Ellingsen, M. Kildemo, Fast and optimal broadband Stokes/Mueller polarimeter design by the use of a genetic algorithm. Opt. Express **18**, 23095–23103 (2010). doi:10.1364/OE.18.023095
54. D. Cattelan, E. Garcia-Caurel, A. De Martino, B. Drevillon, Device and method for taking spectroscopic polarimetric measurements in the visible and near-infrared ranges. Patent application 2937732, Publication number: US 2011/0205539 A1
55. T. Wagner, J.N. Hilfiker, T.E. Tiwald, C.L. Bungay, S. Zollner, Materials characterization in the vacuum ultraviolet with variable angle spectroscopic ellipsometry. Physica Status Solidi A **188**, 1553–1562 (2001). doi:10.1002/1521-396X(200112)188:4<1553:AID-PSSA1553>3.0.CO;2-A
56. A. Zuber, N. Kaiser, J.L. Stehlé, Variable-angle spectroscopic ellipsometry for deep UV characterization of dielectric coatings. Thin Solid Films **261**, 37–43 (1995). doi:10.1016/S0040-6090(94)06492-X
57. E. Garcia-Caurel, J.L. Moncel, F. Bos, B. Drévillon, Ultraviolet phase-modulated ellipsometer. Revi. Sci. Instrum. **73**, 4307–4312 (2002). doi:10.1063/1.1518788
58. D.H. Goldstein, Mueller matrix dual-rotating retarder polarimeter. Appl. Opt. **31**, 6676–6683 (1992). doi:10.1364/AO.31.006676
59. L.L. Deibler, M.H. Smith, Measurement of the complex refractive index of isotropic materials with Mueller matrix polarimetry. Appl. Opt. **40**, 3659–3667 (2001). doi:10.1364/AO.40.003659
60. A. Röseler, *Infrared Spectroscopic Ellipsometry* (Akademie-Verlag, Berlin, 1990)
61. E.H. Korte, A. Röseler, Infrared spectroscopic ellipsometry: a tool for characterizing nanometer layers. Analyst **123**, 647–651 (1998)
62. J.N. Hilfiker, C.L. Bungay, R.A. Synowicki, T.E. Tiwald, C.M. Herzinger, B. Johs, G.K. Pribil, J.A. Woollam, Progress in spectroscopic ellipsometry: applications from vacuum ultraviolet to infrared. J. Vac. Sci. Technol. A **21**, 1103 (2003). doi:10.1116/1.1569928
63. E. Gilli, M. Kornschober, R. Schennach, Optical arrangement and proof of concept prototype for mid infrared variable angle spectroscopic ellipsometry. Infrared Phys. Technol. **55**, 84–92 (2012). doi:10.1016/j.infrared.2011.09.006
64. T.D. Kang, E. Standard, G.L. Carr, T. Zhou, M. Kotelyanskii, A.A. Sirenko, Rotatable broadband retarders for far-infrared spectroscopic ellipsometry. Thin Solid Films **519**, 2698–2702 (2011). doi:/10.1016/j.tsf.2010.12.057
65. C. Bernhar, J. Humlıcek, B. Keimer, Far-infrared ellipsometry using a synchrotron light source the dielectric response of the cuprate high Tc superconductors. Thin Solid Films **455–456**, 143–149 (2004). doi:10.1016/j.tsf.2004.01.002
66. T. Hofmann, C.M. Herzinger, A. Boosalis, T.E. Tiwald, J.A. Woollam, M. Schubert, Variable-wavelength frequency-domain terahertz ellipsometry. Rev. Sci. Instrum. **81**, 023101 (2010). doi:10.1063/1.3297902
67. J.M. Bennett, A critical evaluation of rhomb-type quarterwave retarders. Appl. Opt. **9**, 2123–2129 (1970). doi:10.1364/AO.9.002123
68. E. Garcia-Caurel, A. de Martino, B. Drévillon, Spectroscopic Mueller polarimeter based on liquid crystal devices. Thin Solid films **455–456**, 120 (2003). doi:10.1016/j.tsf.2003.12.056
69. B. Drévillon, A. De Martino, Liquid crystal based polarimetric system, a process for the calibration of this polarimetric system, and a polarimetric measurement process. Patent number US 7,196,792 (filing date 2003)
70. T. Scharf, *Polarized Light in Liquid Crystals and Polymers* (Willey, New Jersey, 2007)
71. A. De Martino, Y-K. Kim, E. Garcia-Caurel, B. Laude, B. Drévillon, Optimized Mueller polarimeter with liquid crystals. Opt. Lett. **28**, 619–618 (2003) doi:10.1364/OL.28.000616
72. S. Ben Hatit, M. Foldyna, A. De Martino, B. Drévillon, Angle-resolved Mueller polarimeter using a microscope objective. Phys. Stat. Sol. (a) **205**, 743 (2008). doi:10.1002/pssa.200777806

73. A. De Martino, S. Ben Hatit, M. Foldyna, Mueller polarimetry in the back focal plane. Proc. SPIE **6518**, 65180X (2007). doi:10.1117/12.708627
74. A. De Martino, E. Garcia-Caurel, B. Laude, B. Drévillon, General methods for optimized design and calibration of Mueller polarimeters. Thin Solid Films **455**, 112–119 (2004). doi:10.1016/j.tsf.2003.12.052
75. N.A. Beaudry, Y. Zhao, R.A. Chipman, Dielectric tensor measurement from a single Mueller matrix image. J. Opt. Soc. Am. A **24**, 814 (2007). doi:10.1364/JOSAA.24.000814
76. A. Lizana, M. Foldyna, M. Stchakovsky, B. Georges, D. Nicolas, E. Garcia-Caurel, Enhanced sensitivity to dielectric function and thickness of absorbing thin films by combining Total Internal Reflection Ellipsometry with Standard Ellipsometry and Reflectometry, to appear in Journal of Physics D. Applied Physics
77. G.E. Jellison, F.A. Modine, Parameterization of the optical functions of amorphous materials in the interband region. Appl. Phys. Lett. **69**, 371–373 (1996). doi:10.1063/1.118064
78. R.A. Synowicki, B.D. Johs, A.C. Martin, Optical properties of soda-lime float glass from spectroscopic ellipsometry. Thin Solid Films **519**, 2907–2913 (2011). doi:10.1016/j.tsf.2010.12.110
79. M. Philipp, M. Knupfer, B. Büchner, H. Gerardin, Plasmonic excitations in ZnO/Ag/ZnO multilayer systems: insight into interface and bulk electronic properties. J. Appl. Phys. **109**, 063710–063716 (2011). doi:10.1063/1.3565047
80. H. Raether, *Surface Plasmons on Smoth and Rough Surfaces and on Gratings* (Springer, Berlin, 1988)
81. F. Abelès, Surface electromagnetic waves ellipsometry. Surf. Sci. **56**, 237–251 (1976). doi:10.1016/0039-6028(76)90450-7
82. H. Arwin, M.K. Poksinski, K. Johansen, Total internal reflection ellipsometry: principles and applications. Appl. Opt. **43**, 3028–3036 (2004). doi:10.1364/AO.43.003028
83. T. Lopez-Rios, G. Vuye G, Use of surface plasmon excitation for determination of the thickness and the optical constants of very thin surface layers. Surf. Sci. **81**, 529–538 (1979). doi:10.1016/0039-6028(79)90118-3
84. P. Wissmann, H.-U. Finzel, Electrical Resistivity of Thin Metal Films (Springer Tracts in Modern, Physics, Berlin, 2007)
85. E.H. Sondheimer, The mean free path of electrons in metals. Adv. Phys. **50**, 499–537 (2001). doi:10.1080/00018730110102187
86. M. Foldyna, A. De Martino, R. Ossikovski, E. Garcia-Caurel, C. Licitra, Characterization of grating structures by Mueller polarimetry in presence of strong depolarization due to finite spot size and spectral resolution. Opt. Commun. **282**, 735–741 (2009). doi:10.1016/j.optcom.2008.11.036
87. J.M. Correas, P. Melero, J.J. Gil, Decomposition of Mueller matrices in pure optical media. Mon. Sem. Mat. Garcia de Galdeano **27**, 233–240 (2003). Free PDF can be downloaded www.unizar.es/galdeano/actas_pau/PDF/233.pdf
88. M. Foldyna, E. Garcia-Caurel, R. Ossikovski, A. De Martino, J.J. Gil, Retrieval of a non-depolarizing component of experimentally determined depolarizing Mueller matrices. Opt. Express **17**, 12794–12806 (2009). doi:10.1364/OE.17.012794
89. B.J. Rice, H. Cao, M. Grumski, J. Roberts, The limits of CD metrology. Microelectron. Eng. **83**, 1023 (2006). doi:10.1063/1.2062991
90. See for example the proceedings of the conference “Advanced Lithography” available on line at the site of the SPIE, www.spie.org
91. V. Ukraintsev, A comprehensive test of optical scatterometry readiness for 65 nm technology production. Proc. SPIE **6152**, 61521G (2006). doi:10.1117/12.657649
92. M. Foldyna, A. De Martino, D. Cattelan, F. Bogeat, C. Licitra, J. Foucher, P. Barritault, J. Hazart, Accurate dimensional characterization of periodic structures by spectroscopic Mueller polarimetry. Proc. SPIE **7140**, 71400I (2008). doi:10.1117/12.804682
93. L. Li, Symmetries of cross-polarization diffraction. J. Opt. Soc. Am. A **17**, 881–887 (2000). doi:10.1364/JOSAA.17.000881

94. A. De Martino, M. Foldyna, T. Novikova, D. Cattelan, P. Barritault, C. Licitra, J. Hazart, J. Foucher, F. Bogeat, Comparison of spectroscopic Mueller polarimetry, standard scatterometry and real space imaging techniques (SEM and 3D-AFM) for dimensional characterization of periodic structures. SPIE Proc **6922**, 69221P (2008). doi:10.1117/12.772721
95. M.G. Moharam, T.K. Gaylord, Diffraction analysis of dielectric surface-relief gratings. J. Opt. Soc. Am. **72**, 1385 (1982). doi:10.1364/JOSA.72.001385
96. R.M. Silver, B.M. Barnes, A. Heckert, R. Attota, R. Dixson, J. Jun, Angle resolved optical metrology. Proc. SPIE **6922**, 69221M.1–69221M.12 (2008). doi:10.1117/12.777131
97. P. Leray, S. Cheng, D. Kandel, M. Adel, A. Marchelli, I. Vakshtein, M. Vasconi, B. Salski, Diffraction based overlay metrology: accuracy and performance on front end stack. Proc. SPIE **6922**, (2008) doi:10.1117/12.772516
98. Y.-n. Kim, J.-s. Paek, S. Rabello, S. Lee, J. Hu, Z. Liu, Y. Hao, W. Mcgahan, Device based in-chip critical dimension and overlay metrology. Opt. Express **17**, 21336–21343 (2009). doi:10.1364/OE.17.021336
99. T. Novikova, A. De Martino, R. Ossikovski, B. Drévillon, Metrological applications of Mueller polarimetry in conical diffraction for overlay characterization in microelectronics. Eur. Phys. J. Appl. Phys. **69**, 63–69 (2005). doi:10.1051/epjap:2005034
100. C. Fallet, Polarimétrie de Mueller résolue angulairement et applications aux structures périodiques. Ph.D. Thesis, Ecole Polytechnique, (2011). The manuscript can be freely downloaded at http://pastel.archives-ouvertes.fr/pastel-00651738/
101. M.R. Antonelli, A. Pierangelo, T. Novikova, P. Validire, A. Benali, B. Gayet, A. De Martino, Impact of model parameters on Monte Carlo simulations of backscattering Mueller matrix images of colon tissue. Biomed. Opt. Express **2**, 1836–1851 (2011). doi:10.1364/BOE.2.001836
102. A. Pierangelo, A. Benali, M.R. Antonelli, T. Novikova, P. Validire, B. Gayet, A. De Martino, Ex-vivo characterization of human colon cancer by Mueller polarimetric imaging. Opt. Express **19**, 1582–1593 (2011). doi:10.1364/OE.19.001582

http://www.springer.com/978-3-642-33955-4

Ellipsometry at the Nanoscale
Losurdo, M.; Hingerl, K. (Eds.)
2013, XXIV, 730 p., Hardcover
ISBN: 978-3-642-33955-4